DISSERTATION

COMPUTATIONAL ADVANCEMENTS IN THE D-BAR RECONSTRUCTION METHOD FOR 2-D ELECTRICAL IMPEDANCE TOMOGRAPHY

Submitted by

Melody Alsaker

Department of Mathematics

In partial fulfillment of the requirements

For the Degree of Doctor of Philosophy

Colorado State University

Fort Collins, Colorado

Spring 2016

Doctoral Committee:

Advisor: Jennifer L. Mueller

Margaret Cheney
Branislav Notaros
Olivier Pinaud

ABSTRACT

COMPUTATIONAL ADVANCEMENTS IN THE D-BAR RECONSTRUCTION METHOD FOR 2-D ELECTRICAL IMPEDANCE TOMOGRAPHY

We study the problem of reconstructing 2-D conductivities from boundary voltage and current density measurements, also known as the electrical impedance tomography (EIT) problem, using the D-bar inversion method, based on the 1996 global uniqueness proof by Adrian Nachman. We focus on the computational implementation and efficiency of the D-bar algorithm, its application to finite-precision practical data in human thoracic imaging, and the quality and spatial resolution of the resulting reconstructions. The main contributions of this work are (1) a parallelized computational implementation of the algorithm which has been shown to run in real-time, thus demonstrating the feasibility of the D-bar method for use in real-time bedside imaging, and (2) a modification of the algorithm to include *a priori* data in the form of approximate organ boundaries and (optionally) conductivity estimates, which we show to be effective in improving spatial resolution in the resulting reconstructions. These computational advancements are tested using both numerically simulated data as well as experimental human and tank data collected using the ACE1 EIT machine at CSU. In this work, we provide details regarding the theoretical background and practical implementation for each advancement, we demonstrate the effectiveness of the algorithm modifications through multiple experiments, and we provide discussion and conclusions based on the results.

ACKNOWLEDGEMENTS

I would like to thank my advisor Jennifer Mueller for extensive advice and guidance over the past few years. Additional thanks goes to the members of the Electrical Impedance Tomography Laboratory at Colorado State University, with special thanks in particular to Michelle Mellenthin.

This project has been supported in part by Award Numbers 1R21EB016869-01A1 and 5R21EB016869-02 from the National Institute of Biomedical Imaging and Bioengineering. The content is solely the responsibility of the author and does not represent the official view of the National Institute of Biomedical Imaging and Bioengineering or the National Institutes of Health.

TABLE OF CONTENTS

LIST OF TABLES

LIST OF FIGURES

CHAPTER 1

INTRODUCTION

1.1. WHAT IS EIT?

Electrical impedance tomography, or EIT, is an imaging modality in which the internal electrical properties (conductivity σ, permittivity ϵ, or resistivity $\rho = 1/\sigma$) of an object are reconstructed using current and voltage data measured only on the object's surface. This is in practice accomplished by attaching an array of electrodes to the surface of the object and applying currents which penetrate into the interior of the object (see Figure 1.1). This creates a voltage distribution on the electrodes, and this resulting surface voltage is measured. Inhomogeneities in the internal conductivity or permittivity distribution will cause perturbations in the surface voltage measurements from the homogeneous case, which can be exploited to reconstruct an image of the internal structures of an object. Temporal changes in conductivity can additionally provide functional imaging of dynamic living and nonliving systems.

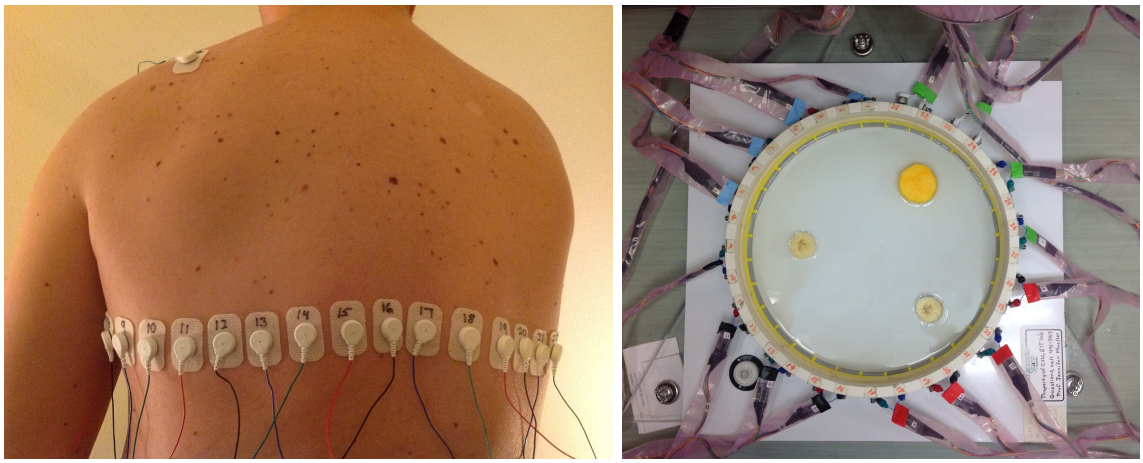

FIGURE 1.1. Left: typical human thoracic 2-D EIT data collection, with electrodes arranged in a plane around the patient's thorax. Right: EIT data collection at CSU using a saline-filled tank containing various targets, surrounded by electrodes.

1.1.1. Current patterns. In practical experiments, current is applied to the domain boundary on L electrodes according to a set of *current patterns*. Each current pattern is applied to the domain boundary in turn, resulting in a corresponding vector of voltage measurements. For L electrodes, there are N linearly independent current patterns where $N \leq L - 1$; this results in at most $L - 1$ linearly independent voltage measurements. All other voltage measurements will therefore be a linear combination of these N voltage measurements.

The choice of current pattern used for a particular application depends on many factors, and is a major engineering consideration in the design of EIT hardware. For an analysis of optimal current patterns and distinguishability in EIT, see [39]. For a description of possible current patterns for EIT, see [129]. In the Electrical Impedance Tomography Laboratory at Colorado State University, the ACE1 EIT machine, which was used to collect the experimental data presented in this dissertation, has been designed to apply bipolar *skip patterns* [127, 128]. In this scenario, equal and opposite current is applied on pairs of electrodes, skipping a electrodes in between, as shown in Figure 1.2, which depicts the case with $a = 2$. Application of a skip a pattern on L electrodes will result in $N = L - \gcd(L, a + 1)$ linearly independent voltage measurements. All experimental and numerically simulated data presented in this dissertation was generated using skip patterns.

1.1.2. Applications of EIT. There are a variety of engineering and industrial applications of EIT (also known as electrical resistance tomography, or ERT), and new uses for the technology continue to emerge. As will be discussed in §1.2.1, the original motivation for EIT was the prospection of underground natural resources, and today EIT is used in a diverse set of geophysical imaging applications. These include the assessment of contaminants in geological media and site remediation [46, 47, 147, 161], the study of underground

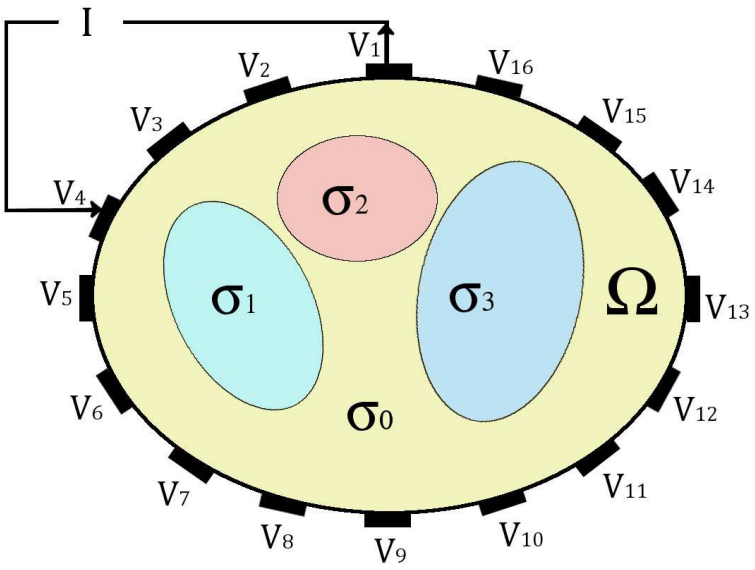

FIGURE 1.2. In skip patterns, equal and opposite current is applied to pairs of electrodes, skipping a electrodes in between. Here is an illustration of the case where $a = 2$, so that current is applied on electrodes e_1 and e_4, in a scenario with $L = 16$ electrodes. For the next current pattern, current will be applied on e_2 and e_5, and so on. Voltage is measured on all L electrodes.

hydrogeological processes and subsurface flow monitoring [48, 52, 111, 145, 148, 193], monitoring underground solute transport [24], and archaeological investigation [143]. In chemical and industrial applications, process tomography may be used to gain insight into complex internal flows and multiphase mixtures occurring inside process equipment. To this end, EIT has been applied to pharmaceutical testing [26, 151, 152], mixture and flow monitoring [53, 81, 105, 117, 125, 126, 150, 187, 189], contaminant detection [120], and various other process applications [96, 190]. Another area of industrial application is the nondestructive evaluation of concrete and other structures [49, 74, 85, 87, 103, 102, 157].

In this dissertation, however, we will mostly consider EIT as it relates to medical imaging applications. The use of EIT for medical imaging is based on the fact that various bodily organs, tissues, fluids, and gases exhibit measurable and significant conductivity differences, as shown in Table 1.1

TABLE 1.1. Conductivity values of various human tissues and organs at 100kHz, based on values reported in [11]. See also [129, 17, 71].

Tissue or Organ	Approximate Conductivity (S/m)
Blood	0.70
Bone (Cancellous)	0.084
Bone (Cortical)	0.021
Bone Marrow	0.0033
Cardiac Muscle (transversal)	0.23
Cardiac Muscle (longitudinal)	0.63
Cartilage	0.18
Fat	0.024
Kidney	0.17
Liver	0.08
Muscle	0.36
Skin (Dry)	0.00045
Skin (Wet)	0.066
Lung (Deflated)	0.27161
Lung (Inflated)	0.10735

In the field of modern medical imaging there are a wide variety of imaging modalities in common use, each with its own benefits as well as problems and shortcomings. It is often desirable to have several imaging options available, and to use these various modalities in conjunction with each other to complement and extend the benefits of each. Magnetic resonance imaging (MRI) and X-ray computed tomography (CT) scans provide images with good spatial resolution but require large, expensive machines which cannot be readily moved or used to provide bedside imaging. CT scanning comes with the additional drawback in that the technique relies on the use of ionizing radiation, the effects of which may accumulate to high levels over a lifetime [60]. The cumulative effects of low-dose ionizing radiation have been linked to the development of cancers and leukemia [1]. Ultrasound technology is safer and more portable than some modalities, but is quite low-contrast, and is difficult to use on obese patients due to limitations in the depth of ultrasound penetration. Electrical impedance tomography is a modality which promises to provide high-contrast real-time bedside imaging with excellent temporal resolution at fairly low cost. The procedure is also painless and

does not use ionizing radiation. EIT may additionally be used to provide complementary information to other modalities.

There is a long, diverse, and ever-growing list of potential medical applications of EIT. For instance, EIT has been studied for use in breast cancer detection, based on evidence that malignant tumors have higher conductivity values than surrounding normal tissues [43, 44, 32, 75, 90, 101, 104, 160, 194]. Various thoracic imaging applications include monitoring of cardiac activity and diagnosis of pulmonary embolism [42, 95, 121, 140, 159, 184], diagnosis of pulmonary edema [33, 139, 142, 178], and ventilation and lung perfusion monitoring [65, 68, 69, 118, 140, 183, 185]. Other biomedical applications include monitoring of gastric emptying and gastric volume [33, 86], bladder volume monitoring [89, 122, 123, 156], prostate imaging [29, 30, 97, 172, 186], assessment of stroke and other neural imaging [2, 15, 57, 73, 86, 141, 146, 153], and imaging of the larynx [158].

In the case of 2-D thoracic imaging, which is a current research focus of the EIT lab in the Department of Mathematics at Colorado State University, it is typical to place a number of approximately equally-spaced electrodes in a single plane around the circumference of a human chest, apply low-frequency, low-amplitude AC current, and then measure the resulting surface voltage. This process, which will be described in greater detail later, provides the necessary data to reconstruct the electrical conductivity distribution within the plane of the electrodes.

1.1.3. The EIT problem. In our mathematical description of the EIT problem, we begin with the *conductivity equation* in $\mathbb{R}^2$, which provides a model of the electric potential $u = u(x, y)$ propagating through a living tissue and the relationship of the potential to the internal spatially varying conductivity distribution. The governing equation is a generalized

Laplace equation derived from Maxwell's equations:

$$\nabla \cdot (\sigma(x,y)\nabla u(x,y)) = 0, \quad (x,y) \text{ in } \Omega, \tag{1}$$

where $\Omega \subset \mathbb{R}^2$ is a bounded, simply-connected domain with Lipschitz boundary, $\sigma : \Omega \to \mathbb{R}$ is the electrical conductivity distribution within Ω, and $u : \Omega \to \mathbb{R}$ is the electrical potential within Ω. See [129] for a full derivation of (1). We may further assume that the conductivity σ is bounded away from zero so that $0 < \sigma(x,y) < c$ for all $(x,y) \in \Omega$; it is straightforward to verify that this condition ensures (1) is an elliptic equation. For our purposes, we will also assume that the conductivity distribution σ is isotropic on Ω.

If the voltage distribution $f = f(x,y)$ on the boundary is known, we may add to (1) the following Dirichlet boundary condition:

$$u\big|_{\partial\Omega} = f, \tag{2}$$

where it is assumed $f \in H^{1/2}(\partial\Omega)$.

The current density J within Ω is modeled by Ohm's law:

$$J = \sigma\nabla u \quad \text{in } \Omega,$$

so that on the boundary we have

$$J \cdot \nu = \sigma \frac{\partial u}{\partial \nu}\bigg|_{\partial\Omega} = j, \tag{3}$$

where we assume $j \in H^{-1/2}(\partial\Omega)$, and ν denotes the outward unit normal. This corresponds to a Neumann boundary condition for (1).

The *forward conductivity problem* is to determine $u \in H^1(\Omega)$ by solving (1) subject to the Dirichlet condition (2), which requires that we have knowledge of the function σ within Ω. The forward problem is readily numerically solvable using a finite element scheme.

Of interest in EIT, however, is to determine the unknown conductivity σ satisfying (1). To this end, we define the *Dirichlet-to-Neumann (DN) map* corresponding to σ, which maps the boundary voltages to the boundary current densities:

$$\Lambda_\sigma : H^{1/2}(\Omega) \to H^{-1/2}(\Omega), \quad \Lambda_\sigma : f \mapsto \sigma \frac{\partial u}{\partial \nu}\bigg|_{\partial\Omega}. \tag{4}$$

The DN map is often called the voltage-to-current density map. For any given conductivity distribution σ on Ω, the DN map encodes all possible EIT boundary measurements, i.e. pairs (f, j) of boundary voltage and current density measurements, in infinite precision. It is well-known from standard PDE theory that Λ_σ is a bounded linear operator acting on f, and a pseudo-differential operator of order 1. The DN map may also be given by its weak formulation, which is readily derived from (4) via integration by parts:

$$\Lambda_\sigma : H^{1/2}(\Omega) \to H^{-1/2}(\Omega), \quad \langle \Lambda_\sigma f, g \rangle = \int_\Omega \sigma \nabla u \cdot \nabla v \, dxdy, \tag{5}$$

where $v \in H^1(\Omega)$ is an arbitrary function with $v\big|_{\partial\Omega} = g$ and $u \in H^1(\Omega)$ is a weak solution to the Dirichlet problem (1).

The *inverse conductivity problem* is then to uniquely determine σ that satisfies (1) given knowledge of the DN map (4). The inverse conductivity problem was first posed in this theoretical form in 1980 by Alberto Calderón [37], who formulated the problem for dimensions 2 and higher. This will be discussed in further detail in §1.2.

1.1.4. The challenges of EIT. The EIT problem turns out to be quite mathematically challenging for a number of reasons. First, the EIT problem is nonlinear in the sense that the forward mapping $\sigma \mapsto \Lambda_\sigma$ is nonlinear, since the potential u depends on the conductivity σ.

Second, the boundary measurements depend non-locally on the internal structures of the domain. As a comparison, in X-ray CT scanning for example, X-ray beams pass through the domain in straight lines with minimal scattering, and the attenuation of X-ray energy depends linearly on the density of the material in the one-dimensional path of the beam. This is quite different from EIT, in which the path of the electrical current depends on the conductivity distribution in the domain. The current therefore takes a complicated path through the domain, and (in real-world practical experiments) diffuses into three dimensions, so that a change in conductivity at any given point inside the object can cause changes in surface measurements at a large number of domain boundary points [45, 86].

A variety of practical problems also exist, relating to the electrical properties of the physical domain and imperfections of electronics and other hardware, as described in [3], for example. We are often interested in conductivity changes deep inside the interior of the domain, but only a relatively small amount of the applied current penetrates deeply. In medical applications this shortcoming is made worse by the presence of resistive tissues such as bone, lungs, or fat. EIT also tends to be highly sensitive to any imperfections in hardware or difficulties with electrode contact.

Finally and most importantly, the inverse conductivity problem is severely ill-posed in the sense of Hadamard. Hadamard gave three conditions for a problem to be well-posed:

(1) A solution must exist.

(2) The solution must be unique.

(3) The solution must depend continuously on the input data.

The EIT problem is ill-posed in the sense that condition (3) is not satisfied: the solution does not depend continuously on the data. More precisely, the forward map $\sigma \mapsto \Lambda_\sigma$ does not have a continuous inverse. This means that large changes in the internal conductivity distribution may result in negligible changes in the boundary measurements and therefore the DN map. Therefore, for any given finite measurement precision, there will exist distinct (and sometimes very different) conductivity distributions that lead to indistinguishable boundary current and voltage measurements. This can be made precise (as was done by Alessandrini in [4]) by showing that for any $\delta > 0$, $C > 0$, there exist σ_1, σ_2 such that

$$\|\Lambda_{\sigma_1} - \Lambda_{\sigma_2}\|_{H^{1/2}(\Omega), H^{-1/2}(\Omega)} < \delta,$$

but

$$\|\sigma_1 - \sigma_2\|_{L^\infty(\Omega)} > C.$$

The severe ill-posedness of EIT leads to many challenges in both the design of EIT systems as well as the theoretical development and application of reconstruction algorithms.

1.2. LITERATURE REVIEW

We now present the highlights of previous theoretical and computational work in electrical impedance tomography, spanning nearly four decades from the date of this writing.

1.2.1. The roots of EIT. Alberto Calderón, whose background was in civil engineering as well as mathematics, was motivated by the potential application of the inverse conductivity problem to identify petroleum deposits in geological media. In 1980, in a short paper that is now hailed as the work responsible for launching the mathematical study of

EIT, Calderón asked whether the conductivity distribution σ of a domain could be uniquely determined from knowledge of the DN map [37]. In other words, is the DN map injective: does $\Lambda_{\sigma_1} = \Lambda_{\sigma_2}$ imply $\sigma_1 = \sigma_2$? Furthermore, if this is true, how does one then determine σ? This is the inverse conductivity problem, which would also come to be known as Calderón's problem.

Calderón was able to prove the injectivity of a linearized version of the inverse conductivity problem, in which we assume σ is a small perturbation from a constant throughout the Lipschitz domain $\Omega \subset \mathbb{R}^n, n \geq 2$, so that $\sigma = 1 + \eta$ where η is small. He accomplished this by first introducing the quadratic form of the DN map,

$$Q_\sigma(\phi) = \int_\Omega \sigma |\nabla u|^2 \, dx.$$

He then showed the injectivity of the Fréchet differential,

$$dQ_\sigma(\phi)\big|_{\sigma=1} = \int_\Omega \delta |\nabla u|^2 dx, \tag{6}$$

at the constant conductivity $\sigma = 1$. This is equivalent to showing the injectivity of the DN map under the linearization assumption.

Importantly, Calderón's proof invokes a set of complex exponential solutions to Laplace's equation,

$$u_\pm(x) = e^{\pi i (z \cdot x) \pm \pi (a \cdot x)},$$

where a and z are vectors in $\mathbb{R}^n$ such that $|a| = |z|$ and $a \cdot z = 0$. These solutions grow exponentially in some directions and decay exponentially in others. Solutions of this type, which are known as *complex geometrical optics* (CGO) solutions (a term which arises due

to similarities to geometrical optics solutions arising in WKB approximations), would be invoked in various forms in many later works on the inverse conductivity problem.

CGO solutions first appeared in [59], a 1966 paper by L.D. Faddeev, whose motivation was quantum scattering theory. Faddeev constructed exponentially growing solutions to a Schrödinger equation in a multidimensional generalization of the 1-D Gelfand-Levitan method for inverse scattering. CGO solutions allow the application of a type of nonlinear Fourier analysis, in which we may construct custom-built nonlinear Fourier transforms to solve a wide variety of inverse problems. The methods involved have today become an essential toolkit in the study of inverse problems (see [179] for a list of applications using CGO solutions of the Schrödinger equation).

Calderón uses his CGO solutions to show that if (6) vanishes for all harmonic u, then $\delta = 0$, and so $dQ_\sigma(\phi)\big|_{\sigma=1}$ is injective. Additionally, Calderón provided an explicit method to approximate σ under the linearization assumption, which involves finding a formula for the approximate Fourier transform of η and then applying an inverse Fourier transform.

This seminal work did not, however, fully answer the central question of whether the DN map is injective. Calderón humbly states, "This we are yet unable to do, and is, as far as we know, an open problem." He goes on to say that if the Fréchet differential about $\sigma = 1$ had a closed range, we could conclude that the DN map itself is injective in some neighborhood of $\sigma = 1$, but this is unfortunately not the case, and so "the desired conclusion cannot be obtained in this fashion" [37].

1.2.2. Continuing theoretical developments. Calderón's work opened the door for decades of further theoretical work on the existence and uniqueness of solutions to the inverse conductivity problem. The following is a summary of these foundational theoretical developments which have shaped the modern study of EIT and other inverse problems.

Boundary determination. In 1984, R. Kohn and M. Vogelius gave a proof that boundary values of σ could be uniquely determined from knowledge of Λ_σ in dimensions $n \geq 2$, provided $\Omega \in C^\infty$ is bounded, and $\sigma \in L^\infty(\overline{\Omega})$, $\sigma > 0$ in $\overline{\Omega}$, with $\sigma \in C^\infty$ in some neighborhood of $\partial\Omega$ [113]. The following year, the same authors showed that the results could be extended to piecewise real-analytic conductivities, and that interior values of σ could be determined in the special case of a layered structure with $\sigma \in C^3(\overline{\Omega})$ [114]. J. Sylvester and G. Uhlmann would later provide an explicit reconstruction method for σ on $\partial\Omega$ under the assumption that $\sigma \in C^\infty(\overline{\Omega})$ [176].

Conductivities in Dimensions $n \geq 3$. The ability to obtain σ on $\partial\Omega$ was a major theoretical advancement, but this result did not fully answer Calderón's original question. Spanning two works published in 1986 and 1987, Sylvester and Uhlmann provided the first global uniqueness theorems showing the injectivity of the DN map. Provided $\partial\Omega \in C^\infty$, they showed uniqueness for 2-D near-constant isotropic conductivities in [173], and for more general isotropic $\sigma \in C^\infty(\overline{\Omega})$ in dimensions $n \geq 3$ in [175]. These results relied on the construction of CGO solutions of the conductivity equation that for large frequencies had behavior similar to the exponential solutions used by Calderón (as explained in [179]).

In 1988, A. Nachman, J. Sylvester, and G. Uhlmann extended the results in dimensions $n \geq 3$ to $\sigma \in C^{1,1}(\overline{\Omega})$ in [136]. The same year, Nachman used the CGO solutions provided in [175] to give the first general reconstruction procedure in [137], and also relaxed the boundary smoothness to $\partial\Omega \in C^{1,1}$. A similar result was provided independently by R.G. Novikov in [144]. These results were extended by Giovanni Alessandrini in 1990 to Lipschitz domains, in a paper which also included a treatment of anisotropic conductivities [5].

Planar conductivities. For several years a global uniqueness result for dimension $n = 2$ remained elusive. To see why the problem in 2 dimensions is more difficult, consider the

following. Since the DN map is a pseudo-differential operator of order 1, it therefore has a Schwartz kernel. In n dimensions, the Schwartz kernel of the DN map is a distribution of $2(n-1)$ variables, but σ is a function of n variables. Therefore the problem in dimensions $n \geq 3$ is overdetermined while the 2-D case is not so. This is explained in detail in [177], for example.

The first 2-D global uniqueness result was provided by Nachman in 1996. Nachman's reconstruction method is indeed the basis for the work presented here and will be described in detail later; here we present a few essential details. In this seminal work, Nachman gave a constructive proof showing the injectivity of the DN map for 2-D isotropic C^2 conductivities in Lipschitz domains [138]. The proof involves the transformation of the conductivity equation into a Schrödinger equation to which CGO solutions are constructed to perform a nonlinear Fourier analysis, hinging on the construction of the *scattering transform* from the EIT data. This integral transform can be thought of as a nonlinear Fourier transform custom-built for the inverse conductivity problem. The scattering transform is then used as a parameter in a PDE involving the $\bar{\partial}$ (D-bar) operator. This technique is known as the D-bar method, and a similar method was first introduced by C.S. Gardner, et al in 1967 in [72] for use in solving the KdV equation. D-bar methods were later used as the foundation for the inverse scattering method to solve nonlinear evolution equations by R. Beals and R. Coifman in [20].

Further theoretical developments concerning conductivities in 2-D included the work of R. Brown and G. Uhlmann in 1997, who showed uniqueness results for $\sigma \in C^1(\Omega)$ in [35]. Brown and Uhlmann also used D-bar methods, but employed a technique which involved rewriting the conductivity equation as a first-order system rather than using a second-order Schrödinger equation (which was in fact based on a method used by Beals and Coifman in

[21].) Later, results were further extended to non-smooth conductivities $\sigma \in L^\infty(\Omega)$ by K. Astala and L. Päivärinta in 2006 in [13], where the authors provide a constructive uniqueness proof based on transforming the conductivity equation to the Beltrami equation and then constructing CGO solutions to the Beltrami equation.

Complex conductivities. There has also been theoretical work on the inverse conductivity problem with complex conductivities, known as *admittivities*, of the form

$$\gamma(z) = \sigma(z) + i\omega\epsilon(z), \quad z \in \Omega, \tag{7}$$

where σ is the real-valued conductivity, ω is the frequency of the applied electromagnetic wave, and ϵ is the electric permittivity of the medium encompassed by the domain Ω. This work was pioneered in 2000 by E. Francini in [63], who showed that admittivities γ of the form (7), with $\sigma \in W^{2,\infty}(\Omega)$ and small permittivity $\epsilon \in W^{2,\infty}(\Omega)$, where $\Omega \subset \mathbb{R}^2$ with Lipschitz boundary, can be uniquely determined from the DN map. Francini's proof was based on D-bar methods, but was not completely constructive, since it lacked a connection between the DN map and the voltage data, and so did not contain the complete set of equations necessary to reconstruct the admittivity. In 2012, the gaps were filled in by S.J. Hamilton, et al in [76], who provided a complete direct reconstruction method for admittivities $\gamma \in W^{2,\infty}(\Omega)$ in bounded, simply connected Lipschitz domains in $\mathbb{R}^2$. Additionally, a non-constructive proof that does not require small permittivity ϵ can be found in [36].

1.2.3. Practical reconstruction algorithms and computation. While an abstract theoretical foundation for the inverse conductivity problem provides us with necessary information about what is possible to achieve, the problem was originally motivated by practical applications to real-world situations. Researchers the world over continue to seek out

the best ways to apply the theoretical knowledge developed over the past decades to produce working computational algorithms for use in engineering and biomedical applications. The goal of any computational reconstruction algorithm is to obtain an approximation to the conductivity σ on the interior of an object using a finite number of noisy finite-precision boundary measurements. The primary numerical methods that have been developed to solve the inverse conductivity problem fall into five basic categories: linearization-based methods, nonlinear iterative algorithms, layer stripping algorithms, statistical inversion techniques, and D-bar methods. We will next provide a brief overview of these methods along with some commentary on each.

Linearization. Linearization methods are based on the assumption that the conductivity is some small perturbation from a constant or other known distribution so that the boundary data depends linearly on conductivity. The linearized problem is then solved using some (typically noniterative) regularized inversion method. One obvious drawback to these linear approximation techniques is that the approximation is only valid when the actual conductivity is a small deviation from the distribution used as reference.

As previously discussed, Calderón provided such a method in his original 1980 paper [37]. Computational work based on Calderón's method applied to simulated practical data was described in the late 1980s and early 1990s in [40, 91–93], and the method was applied to experimental data in 2008 in [23] and [31] and extended to elliptical domains in [134]. In 1984, D.C. Barber and B.H. Brown provided what would come to be known as the Barber-Brown backprojection method in [16], with further developments based on this method described in [22] and [155]. Various noniterative Newton methods have been developed, including the now widely-used NOSER algorithm provided in [41], which is based on one step of a Newton-Raphson method. Extensions of NOSER and other one-step Newton methods are described

in [25, 130, 131]. Additionally, an integral identity first described by Calderón was used in [6] to reduce the nonlinear inverse problem to a moment problem.

Iterative algorithms. Various Newton-type nonlinear iterative techniques have also been widely used in EIT. One of the most popular methods involves reformulating the inverse problem as a regularized least-squares minimization problem as in [28, 27, 54–56, 100, 192]. In these methods, a weighted least-squares error functional $F(\sigma)$ is formed with the hope of finding the conductivity σ which minimizes F and therefore fits the boundary measurements in a least-squares sense. The problem is ill-posed and is therefore regularized, often by adding a Tikhonov-type regularization functional as an extra term. It is then typically solved using multiple iterations of a quasi-Newton method. As an alternative, algorithms involving variational equation-error formulations have appeared in [112, 115, 191, 192], which are based on the minimization of a regularized equation-error functional. While these methods do provide accurate conductivity values in many cases, speedy convergence is not guaranteed, and the algorithms may be prohibitively slow.

Layer-stripping. Layer-stripping methods were described by E. Somersalo et al in 1991 in [168], and were further developed by Sylvester shortly thereafter in [174]. The basis for these direct nonlinear techniques can be understood as follows. Boundary voltages corresponding to the highest spatial frequency are used to find the conductivity distribution within some thin layer of the boundary. This information is then used to synthesize the voltages on a subsurface close to the boundary, by solving a Riccati-type nonlinear differential equation. We then imagine that the outermost layer has been stripped off the domain, and the conductivity of a second thin layer near this new boundary may then be computed. The process repeats inductively, and the conductivity is found layer-by-layer from the outside in. While this method is computationally fast and has been shown to provide good approximations

for boundary conductivities, it proves to be highly unstable in the presence of noise and is therefore unsuitable for experimental data.

Statistical inversion methods. In 1997, Somersalo et al described in [169] a nonlinear inversion scheme for EIT based upon Bayesian statistics; extensions and applications of this method have since appeared in [116, 98, 149, 171, 188]. These algorithms reformulate the inverse problem into a type of statistical inference, where all known and unknown quantities involved in the problem are modeled as random variables. The goal is to estimate the posterior probability density distribution of the unknown variables, from which estimates for the conductivity may be computed along with associated *a posteriori* uncertainties. Estimates for the conductivity can be found by computing the conditional expectation, which requires integration of the posterior probability density. This is typically accomplished via Markov chain Monte Carlo sampling methods. While methods based on statistical inversion have been shown to provide promising results, as with the Newton-like iterative techniques these Bayesian algorithms tend to involve great computational expense and may be too slow to be of clinical use.

D-bar methods. Regularized D-bar methods are both nonlinear and direct (noniterative). As of this writing, they are in fact the only direct methods that allow for a true regularization strategy, which makes them noise-robust and therefore suitable for use with real-world data. Since D-bar methods are in fact the subject of this dissertation, we will explain the mathematical foundation and computational steps in detail later; here we present only a history of advancements.

The D-bar method is an implementation of the previously mentioned 1996 reconstruction method of A. Nachman in [138], in which he constructively proved the injectivity of the Dirichlet-to-Neumann map in the case of $W^{2,p}, p > 1$ conductivities in 2 dimensions. The

first numerical implementation of Nachman's method was provided by S. Siltanen, J.L. Mueller, and D. Isaacson in [163], in which the authors apply the method to high- and low-contrast C^∞ radially symmetric conductivities, while noting that the implementation would certainly apply to conductivities lacking radial symmetry. In 2002, Mueller, Siltanen, and Isaacson successfully applied the algorithm to a noise-free numerically simulated chest phantom with elliptical organ boundaries representing a heart and two lungs in [133], and a regularization scheme was given by Mueller and Siltanen in [132]. Around this same time, in [110] and [106], K. Knudsen (along with A. Tamasan in the first work) implemented the related method of Brown and Uhlmann in [35], in which C^1 conductivities are permissible. In 2004, Knudsen, Mueller, and Siltanen also demonstrated the computational efficiency of the D-bar algorithm applied to a more general set of problems using a 2-grid method in [109].

Further developments in D-bar methods for EIT include a variety of computational improvements and extensions. The method was first applied to experimental data in the 2004 paper [94] by Isaacson et al; this data was collected on a saline-filled tank containing agar heart and lung phantoms. In 2006, the same authors demonstrated the application of the method to cardiac imaging in the case of actual human data in [95]. A study of the method applied to discontinuous conductivities appeared in [107], and the same authors provided a regularized D-bar method via low-pass filtering for EIT in 2009 in [108]. The method was extended to non-circular chest-shaped domains in [135] (2009), and an improved numerical approximation to the scattering transform (the nonlinear Fourier transform used in the method) was provided in [50] (2010).

More recent computational advancements in D-bar methods for EIT include the following. Implementations for complex admittivities appeared in [76, 78] (2012, 2013), and

reconstructions of both conductivity and admittivity from human chest data appeared in [84]. A method for anisotropic conductivities appeared in [77] (2014), the requirement that the conductivities be constant near the boundary was removed in [164] (2014); and in [80] (2014) a method to preserve edges within EIT images was introduced.

1.3. NACHMAN'S METHOD OF RECONSTRUCTION

In this section we present a discussion of the theoretical formulation in infinite precision of the D-bar method for the inverse conductivity problem, which is due to A. Nachman's constructive global uniqueness proof in [138]. This method is the focus of the computational advancements detailed in this dissertation. Other helpful resources that include additional explanation and development of the theory include [129, 162].

1.3.1. Problem statement. We assume $\Omega \subset \mathbb{R}^2$ is a bounded and simply-connected Lipschitz domain, we associate $(x, y) \in \mathbb{R}^2$ with $z = x + iy \in \mathbb{C}$, and assume $\sigma(z) \in W^{2,p}(\Omega)$ for some $p > 1$ is the isotropic conductivity distribution within Ω, where for arbitrary $U \subset \mathbb{R}^n$, $\rho \in [1, \infty]$, $k \geq 0$ we define the Sobolev space

$$W^{k,\rho}(U) := \{f \in L^\rho(U) | \partial^\alpha f \in L^\rho(U), |\alpha| \leq k\}.$$

We further assume σ is constant in some neighborhood of $\partial\Omega$, and $0 < c \leq \sigma(z)$. The mathematical formulation of the inverse conductivity problem was provided previously in §1.1.3, but is repeated here for the reader's convenience. Our goal is to recover the unknown σ in the generalized Laplace equation

$$\nabla \cdot (\sigma \nabla u) = 0 \quad \text{in } \Omega, \tag{8}$$

where u is the electrical potential. Boundary voltages and current densities are modeled by the DN map:

$$\Lambda_\sigma : f \mapsto \sigma \frac{\partial u}{\partial \nu}\bigg|_{\partial\Omega}, \tag{9}$$

where $f \in H^{1/2}(\partial\Omega)$ and $j \in H^{-1/2}(\partial\Omega)$ are the infinite-precision boundary voltage and current density measurements, respectively.

1.3.2. Transformation to the Schrödinger equation. We begin with a change of variables

$$q(z) = \frac{\Delta\sqrt{\sigma(z)}}{\sqrt{\sigma(z)}}, \quad \tilde{u}(z) = \sqrt{\sigma(z)}u(z)$$

that transforms (8) into the 2-D Schrödinger equation:

$$-\Delta\tilde{u}(z) + q(z)\tilde{u}(z) = 0 \quad \text{in } \Omega. \tag{10}$$

For simplicity, assume $\sigma \equiv 1$ near $\partial\Omega$. Then the Schrödinger potential q satisfies $q = 0$ within this same neighborhood, so we can smoothly extend $\sigma = 1, q = 0$, and therefore (10), to all of $\mathbb{R}^2$.

We next introduce a complex frequency parameter $k = k_1 + ik_2$. The D-bar method hinges on finding complex geometrical optics (CGO) solutions $\psi(z, k)$ to

$$-\Delta\psi(z,k) + q(z)\psi(z,k) = 0 \quad \text{in } \mathbb{R}^2. \tag{11}$$

L.D. Faddeev first introduced these exponentially-behaving solutions to (11) in [59]. Nachman proved the existence of CGO solutions to (11) three decades later: by Theorem 1.1 in

[138], for any $k \in \mathbb{C}\backslash\{0\}$ there exists a unique solution $\psi(z,k)$ satisfying

$$e^{-ikz}\psi(z,k) - 1 \in W^{1,\tilde{p}}(\mathbb{R}^2), \quad \tilde{p} > 2, \tag{12}$$

so that $\psi(z,k)$ is asymptotic to e^{ikz} as $|z| \to \infty$. The behavior of $\psi(z,k)$ as $|z| \to \infty$ can be discerned as follows:

$$\begin{aligned} \psi \sim e^{ikz} &= e^{i(k_1+ik_2)(x+iy)} \\ &= e^{-(k_1y+k_2x)}e^{i(k_1x-k_2y)}, \end{aligned}$$

indicating an exponential decay / growth condition in the directions $\pm(x,y)$ and periodicity in the orthogonal directions $\pm(x,-y)$. Due to symmetry, analogous behavior results if we hold z fixed and look at $\psi(z,k)$ as $|k| \to \infty$ over the k-plane.

It will be useful to define the function

$$\mu(z,k) := e^{-ikz}\psi(z,k). \tag{13}$$

Since μ satisfies $\mu(z,k) - 1 \in W^{1,\tilde{p}}(\mathbb{R}^2)$, the Sobolev embedding theorem implies that $\mu \in L^\infty(\mathbb{R}^2) \cap C(\mathbb{R}^2)$, and clearly $\mu(z,k)$ is asymptotically close to 1 as $|z| \to \infty$.

1.3.3. The $\bar{\partial}$ and ∂ operators. We now define the D-bar ($\bar{\partial}$) operator for which Nachman's algorithm is named, as well as its cousin, the ∂ operator, which together are sometimes called the *Wirtinger derivatives*. Given $z = x + iy \in \mathbb{C}$, we define

$$\begin{aligned} \bar{\partial}_z = \frac{\partial}{\partial \bar{z}} &:= \frac{1}{2}\left(\frac{\partial}{\partial x} + i\frac{\partial}{\partial y}\right), \\ \partial_z = \frac{\partial}{\partial z} &:= \frac{1}{2}\left(\frac{\partial}{\partial x} - i\frac{\partial}{\partial y}\right). \end{aligned}$$

The action of the $\bar{\partial}$ operator on a function gives us information about the function's differentiability. Recall that a complex-valued function $f(x+iy) = u(x,y) + iv(x,y)$ is analytic if and only if f satisfies the Cauchy-Riemann conditions:

$$\frac{\partial u}{\partial x} = \frac{\partial v}{\partial y}, \qquad \frac{\partial u}{\partial y} = -\frac{\partial v}{\partial x}. \tag{14}$$

If f satisfies (14), we may therefore compute

$$\bar{\partial}_z f = \frac{1}{2}\left(\left(\frac{\partial u}{\partial x} + i\frac{\partial v}{\partial x}\right) + \left(i\frac{\partial u}{\partial y} - \frac{\partial v}{\partial y}\right)\right) = \frac{1}{2}\left(\left(\frac{\partial u}{\partial x} - \frac{\partial v}{\partial y}\right) + i\left(\frac{\partial v}{\partial x} + \frac{\partial u}{\partial y}\right)\right) = 0.$$

Since the converse is also true, we have that f is analytic if and only if $\bar{\partial}_z f = 0$.

It is also easy to verify that the ∂ and $\bar{\partial}$ operators have the expected product, quotient, and chain rules; and the Laplacian operator Δ can be written as

$$\Delta = \frac{\partial^2}{\partial x^2} + \frac{\partial^2}{\partial y^2} = \left(\frac{\partial}{\partial x} + i\frac{\partial}{\partial y}\right)\left(\frac{\partial}{\partial x} - i\frac{\partial}{\partial y}\right) = 4\bar{\partial}_z\partial_z. \tag{15}$$

1.3.4. A Lippmann-Schwinger equation for μ. We next derive a Lippmann-Schwinger type integral equation for which μ is a solution. This integral equation will later be differentiated to obtain the *D-bar equation*, which is the main equation in the method.

We begin by rewriting the Schrödinger equation (11) to obtain a PDE for μ involving the ∂ and $\bar{\partial}$ operators. From (11), and using (15) and $\psi(z,k) = e^{ikz}\mu(z,k)$, we compute:

$$\begin{aligned} & q(z)\psi(z,k) = \Delta\psi(z,k) \\ \iff\ & q(z)e^{ikz}\mu(z,k) = 4\partial\bar{\partial}(e^{ikz}\mu(z,k)) \\ & \qquad = 4\partial\big(\mu(z,k)\bar{\partial}e^{ikz} + e^{ikz}\bar{\partial}\mu(z,k)\big) \end{aligned}$$

$$
\begin{aligned}
&= 4\partial(e^{ikz}\bar{\partial}\mu(z,k)) \\
&= 4(\partial e^{ikz})(\bar{\partial}\mu(z,k)) + e^{ikz}\partial\bar{\partial}\mu(z,k) \\
&= 4\left(\frac{1}{2}\big(ike^{ikz} - i(ike^{ikz})\big)(\bar{\partial}\mu(z,k)) + e^{ikz}\partial\bar{\partial}\mu(z,k)\right) \\
&= e^{ikz}4ik\bar{\partial}\mu(z,k) + e^{ikz}4\partial\bar{\partial}\mu(z,k).
\end{aligned}
$$

Canceling a factor of e^{ikz} on each side of the equation and rearranging for convenience therefore yields

$$
L_k\mu(z,k) = -q(z)\mu(z,k), \tag{16}
$$

where $L_k := -4(\partial\bar{\partial} + ik\bar{\partial}) = -(\Delta + 4ik\bar{\partial})$.

Next define the *Faddeev Green's function*

$$
g_k(z) := \frac{1}{(2\pi)^2}\int_{\mathbb{R}^2} \frac{e^{iz\cdot\xi}}{|\xi^2| + 2k(\xi_1 + i\xi_2)}\, d\xi, \tag{17}
$$

where $\xi = (\xi_1, \xi_2) \in \mathbb{R}^2$ and $z\cdot\xi = x\xi_1 + y\xi_2$. The function g_k, introduced by L.D. Faddeev in [59], is a fundamental solution for the operator L_k, so that $L_k g_k(z) = \delta(z)$. This can be seen with a few straightforward computations, outlined as follows. We define the Fourier transform $\mathcal{F}$ and its inverse $\mathcal{F}^{-1}$ by

$$
(\mathcal{F}f)(\xi) = \hat{f}(\xi) := \int_{\mathbb{R}^2} e^{-iz\cdot\xi} f(z)dz, \qquad (\mathcal{F}^{-1}\hat{f})(z) = f(z) := \frac{1}{2\pi^2}\int_{\mathbb{R}^2} e^{iz\cdot\xi}\hat{f}(\xi)d\xi.
$$

It is clear that g_k can be written as $g_k(z) = \mathcal{F}^{-1}\big(\frac{1}{P(\xi)}\big)$, where $P(\xi) = (|\xi|^2 + 2k(\xi_1 + i\xi_2))$.

Also, we can readily obtain

$$\mathcal{F}(L_k f)(\xi, k) = P(\xi)\hat{f}(\xi, k), \tag{18}$$

by observing that $\mathcal{F}(-\Delta f(z,k))(\xi) = |\xi|^2 \hat{f}(\xi,k)$ and $\mathcal{F}(\bar{\partial} f(z,k)) = \frac{1}{2}(i\xi_1 + i^2\xi_2)\hat{f}(\xi,k)$. In this formulation, $P(\xi)$ is the symbol of the operator L_k, so by standard Fourier theory we have that $g_k(z) = \mathcal{F}^{-1}\big(\frac{1}{P(\xi)}\big)$ is a fundamental solution. This can be seen explicitly by applying inverse Fourier transforms to (18):

$$\begin{aligned} f(z,k) &= \mathcal{F}^{-1}\left(\left(\frac{1}{P(\xi)}\right)\mathcal{F}(L_k f)(\xi)\right)(z) \\ &= \left(\mathcal{F}^{-1}\left(\frac{1}{P(\xi)}\right) * L_k f(\xi)\right)(z) \\ &= (g_k * L_k f)(z,k) = (L_k g_k * f)(z,k). \end{aligned}$$

See also [162] for some useful properties of the Faddeev Green's function g_k.

It is now straightforward to see that a solution to the Lippmann-Schwinger type integral equation

$$\mu - 1 = -g_k * (q\mu) \tag{19}$$

is a solution to (16), since

$$\begin{aligned} &L_k(\mu - 1) = L_k(-g_k * (q\mu)) \\ &\implies L_k\mu = -(L_k g_k) * (q\mu) = -\delta * (q\mu) = -q\mu, \end{aligned}$$

and furthermore it can be verified that μ will satisfy $\mu(z,k) - 1 \in W^{1,\tilde{p}}(\mathbb{R}^2)$.

The conductivity $\sigma(z)$ can be recovered directly from the solution $\mu(z,k)$. To see this, substitute $q(z) = \Delta\sqrt{\sigma}/\sqrt{\sigma}$ and take $k \to 0$ in the PDE (16) to yield

$$\Delta\mu(z,0) = \frac{\Delta\sqrt{\sigma(z)}}{\sqrt{\sigma(z)}}\mu(z,0). \tag{20}$$

Then the asymptotic condition $\mu(z,0) - 1 \in W^{1,\tilde{p}}(\mathbb{R}^n)$ along with $\sigma(z) \equiv 1$ on $\mathbb{R}^2\backslash\Omega$ implies

$$\lim_{k\to 0}\mu(z,k) = \sqrt{\sigma(z)},$$

and in fact it can be verified directly that

$$\mu(z,0) = \sqrt{\sigma(z)} \tag{21}$$

is a solution to (20) satisfying the asymptotic condition $\mu(z,0) - 1 \in W^{1,\tilde{p}}(\mathbb{R}^n)$ as desired. The rigorous proof in [138] of the relationship (21) takes into account the $\log|k|$ singularity at $k = 0$ of the Faddeev Green's function g_k.

Our goal will therefore be to find the solution μ satisfying (19). It is not obvious, however, from the above derivations how the solution μ relates to the measured EIT data encoded in Λ_σ. The solution method, which establishes this link, involves several other intermediate functions and equations, as outlined over the following pages.

1.3.5. Linking Λ_σ and ψ. In [138], Nachman established a connection between the EIT data Λ_σ and the CGO solution ψ. This will involve several steps, the first of which is to derive a close relationship between the DN map Λ_σ for the conductivity problem and the DN map for the Schrödinger equation (10), $\Lambda_q : H^{1/2}(\partial\Omega) \to H^{-1/2}(\partial\Omega)$, defined informally

by

$$\Lambda_q : f \mapsto \left.\frac{\partial \tilde{u}}{\partial \nu}\right|_{\partial\Omega}, \tag{22}$$

where $\tilde{u} \in H^1(\Omega)$ is the unique (weak) solution to (10) satisfying the Dirichlet condition $\tilde{u}|_{\partial\Omega} = f$. From the change of variables $\tilde{u} = \sqrt{\sigma}u$ where u solves (8), we can compute

$$\frac{\partial \tilde{u}}{\partial \nu} = \frac{\partial}{\partial \nu}(\sqrt{\sigma}u) = \frac{1}{2\sqrt{\sigma}}\frac{\partial \sigma}{\partial \nu}u + \sqrt{\sigma}\frac{\partial u}{\partial \nu}.$$

The assumption $\sigma \equiv 1$ in a neighborhood of $\partial\Omega$ implies $\frac{\partial \sigma}{\partial \nu}|_{\partial\Omega} = 0$, and furthermore $\frac{\partial u}{\partial \nu}|_{\partial\Omega} = \Lambda_\sigma f$, so we conclude that

$$\Lambda_q f = \left.\frac{\partial \tilde{u}}{\partial \nu}\right|_{\partial\Omega} = \left.\frac{\partial u}{\partial \nu}\right|_{\partial\Omega} = \Lambda_\sigma f,$$

so that in fact for such σ we have

$$\Lambda_q = \Lambda_\sigma. \tag{23}$$

The connection between Λ_σ and $\psi|_{\partial\Omega}$ comes in the form of a boundary integral equation, which we derive in the remainder of this section.

The previously defined fundamental solution g_k is closely related to the Faddeev Green's function G_k:

$$G_k(z) := e^{ikz} g_k(z). \tag{24}$$

A straightforward computation using (15) and (24) will reveal that $-\Delta G_k(z) = \delta(z)$.

A solution to the Schrödinger equation (11) can be obtained by multiplying the Lippmann-Schwinger equation (19) through by e^{ikz} to yield a similar equation for ψ:

$$\psi(z,k) - e^{ikz} = -G_k * (q\psi) = -\int_\Omega G_k(z-\zeta)q(\zeta)\psi(\zeta,k)\, d\zeta, \tag{25}$$

where we recall that $q = 0$ outside of Ω so that we may restrict the domain of integration.

We next state a crucial theorem due to G. Alessandrini:

THEOREM 1. *(Alessandrini's Identity [4]) For any two solutions $v_1, v_2 \in H^1(\Omega)$ (along with corresponding Schrödinger potentials q_1, q_2) to $(-\Delta + q_j)v_j = 0$ in Ω, we have that*

$$\int_\Omega (q_1 - q_2)v_1 v_2 dz = \int_{\partial\Omega} v_1(\Lambda_{q_1} - \Lambda_{q_2})v_2 ds.$$

The application of Theorem 1 to (25) provides us with a direct link between the CGO solution ψ and the DN map for the Schrödinger equation. To see this, choose $v_1 = G_k(z - \zeta), q_1 = 0$ (valid since $-\Delta G_k(z-\zeta) = 0$ for all $z \neq \zeta$), and set $v_2 = \psi, q_2 = q = \Delta\sqrt{\sigma}/\sqrt{\sigma}$. These substitutions into the left-hand side of Alessandrini's identity gives us the right-hand side of (25), so that application of the identity yields

$$\begin{aligned} \psi(z,k) - e^{ikz} &= -\int_\Omega G_k(z-\zeta)q(\zeta)\psi(\zeta,k)\, d\zeta \\ &= \int_{\partial\Omega} G_k(z-\zeta)(\Lambda_0 - \Lambda_q)\psi(\zeta,k) ds(\zeta). \end{aligned} \tag{26}$$

By Theorem 5 in [138], we may take $z \to \partial\Omega$ in (26) so that the trace on $\partial\Omega$ of the solution ψ satisfies the boundary integral equation

$$\psi(z,k)\big|_{\partial\Omega} = e^{ikz}\big|_{\partial\Omega} - S_k(\Lambda_q - \Lambda_0)\psi(z,k), \tag{27}$$

where we define the *Faddeev single-layer operator* S_k for $k \neq 0$ by

$$S_k f(z) := \int_{\partial\Omega} G_k(z-\zeta) f(\zeta) ds(\zeta). \tag{28}$$

Then substituting $\Lambda_q = \Lambda_\sigma$ and observing that $q = 0$ is consistent with $\sigma \equiv 1$ gives

$$\psi(z,k)\big|_{\partial\Omega} = e^{ikz}\big|_{\partial\Omega} - S_k(\Lambda_\sigma - \Lambda_1)\psi(z,k), \tag{29}$$

where Λ_1 is the DN map corresponding to homogeneous conductivity $\sigma \equiv 1$ in Ω. We have therefore established a direct link between the EIT data Λ_σ and the CGO solution ψ.

1.3.6. The scattering transform. Here we define the *scattering transform* $\mathbf{t}$, which is the very important nonlinear Fourier transform mentioned previously in §1.2.3, in its two equivalent forms:

$$\mathbf{t}(k) := \int_{\mathbb{R}^2} e^{i\bar{k}\bar{z}} q(z)\psi(z,k)\, dz \tag{30}$$

$$\mathbf{t}(k) := \int_{\mathbb{R}^2} e^{i(kz+\bar{k}\bar{z})} q(z)\mu(z,k)\, dz \tag{31}$$

One can readily see from (31) that due to the asymptotic behavior $\mu \sim 1$, we have that

$$\mathbf{t}(k) \approx \hat{q}(k)\big|_{k=(-2k_1,2k_2)}$$

for large $|k|$. Also observe that the scattering transform is *nonphysical* in the sense that it has no real-world physical representation and cannot be measured directly in experiments. We will see that the scattering transform contains the necessary information to recover the conductivity $\sigma(z)$.

When written in the forms given in (30) and (31), there is no direct connection between the EIT data Λ_σ and the scattering transform $\mathbf{t}$. The connection is easy to see, however, through another application of Alessandrini's identity. This time let $q_1 = 0, v_1 = e^{i\bar{k}\bar{z}}$ (valid since $e^{i\bar{k}\bar{z}}$ is harmonic), and keep $v_2 = \psi(z,k), q_2 = q$ as in the derivation of (26). Then, observing that q is compactly supported and using $\Lambda_\sigma = \Lambda_q$, Theorem 1 applied to (30) yields

$$\mathbf{t}(k) = \int_{\partial\Omega} e^{i\bar{k}\bar{z}}(\Lambda_\sigma - \Lambda_1)\psi(z,k)\, ds(z). \tag{32}$$

As written in (32), the scattering transform contains an instance of $\psi(z,k)|_{\partial\Omega}$, which itself may be written in terms of Λ_σ as in (29), so that the EIT data appears twice in this boundary integral formulation of $\mathbf{t}$.

1.3.7. The D-bar equation. We now use $\mathbf{t}$ as a parameter in a special PDE, the solution to which yields the intermediate function $\mu(z,k)$ which will then give us σ directly through (21). The derivation is fully explained by Nachman in the proof for Theorem 2.1 of [138], and requires careful differentiation of the Lippmann-Schwinger equation (19) with respect to $\bar{k}$ to obtain the *D-bar equation:*

$$\bar{\partial}_k \mu(z,k) = \frac{\mathbf{t}(k)}{4\pi\bar{k}} e^{-i(kz+\bar{k}\bar{z})}\overline{\mu(z,k)}. \tag{33}$$

Theorem 4.1 of [138] guarantees that (33) has a unique solution with $\mu(z,k) - 1 \in L^\rho \cap L^\infty(\mathbb{C})$, where $\rho > 2$. Let $\beta_k = (\pi\bar{k})^{-1}$, and observe that $\bar{\partial}_k \beta_k = \delta(k)$, making β_k a fundamental solution for the $\bar{\partial}_k$ operator. Consider the generalized Lippmann-Schwinger equation

$$\mu - 1 = -\beta_k * (r\bar{\mu}), \tag{34}$$

where

$$r_k(z) := \frac{\mathbf{t}(k)}{4\pi\bar{k}} e^{-i(kz+\bar{k}\bar{z})}.$$

Application of $\bar{\partial}_k$ to both sides of (34) reveals that any solution to (33) satisfying $\mu(z,k)-1 \in L^\rho \cap L^\infty(\mathbb{C})$ will also satisfy (34). We may also write (34) in the following form, which is a Fredholm integral equation of the second kind:

$$\mu(z,k) = 1 + \frac{1}{4\pi^2} \int_{\mathbb{R}^2} \frac{\mathbf{t}(k')}{(k-k')\bar{k'}} e^{-i(kz+\bar{k}\bar{z})} \overline{\mu(z,k')} dk'. \tag{35}$$

As shown in [138], (35) is uniquely solvable at every fixed $z \in \mathbb{R}^2$, and in practical computations it is an approximation of (35) which we solve to obtain an approximation of $\mu(z,k)$.

Once (35) is solved for $\mu(z,k)$, we obtain the desired conductivity distribution $\sigma(z)$ via the algebraic relationship (21).

1.3.8. Summary of the method. In summary, the method of A. Nachman is as follows. Given infinite-precision boundary voltage and current density data Λ_σ,

(1) Solve the boundary integral equation (29) to obtain the CGO solution $\psi|_{\partial\Omega}$.

(2) Use $\psi|_{\partial\Omega}$ to compute the nonphysical scattering transform $\mathbf{t}(k)$ via the boundary-integral formulation (32).

(3) Use the scattering transform $\mathbf{t}$ as a parameter in the D-bar integral equation (35).

(4) Solve the D-bar integral equation (35) to obtain the CGO solution $\mu(z,k)$.

(5) Obtain $\sigma(z)$ from $\mu(z,k)$ using the algebraic relationship (21).

CHAPTER 2

A REAL-TIME D-BAR ALGORITHM

This chapter contains a detailed overview of our fast computational implementation of the D-bar algorithm for 2-D EIT, which represents the first D-bar algorithm to run in real time. The work contained in this chapter was published as "A Real-Time D-bar Algorithm for 2-D Electrical Impedance Tomography Data" in Inverse Problems and Imaging (IPI) in 2014, by the American Institute of Mathematical Sciences (AIMS). See [9] for the original published version. The author has obtained proper approval from AIMS (granted via email) to include in this dissertation a modified version of this previously published work. Additionally, some of the results included here were presented at the 15th International Conference on Biomedical Applications of Electrical Impedance Tomography and were published in the conference proceedings from this event (see [8]).

The reconstruction algorithm is based on Nachman's constructive global uniqueness proof [138] along with subsequent theory and implementations in [163, 107, 132, 94, 95, 135, 50, 108]. We give results based on experimental human data collected under proper approvals from the International Research Board at CSU.

2.1. MOTIVATION AND OVERVIEW

EIT holds great promise as a bedside imaging tool for patients in intensive care. Acquisition and computation of time-dependent image sequences is known as *functional Electrical Impedance Tomography* (f-EIT). Functional conductivity images have been used for monitoring pulmonary perfusion [34, 67, 166], determining regional ventilation in the lungs [69, 66, 183], detecting extravascular lung water [119], and evaluating shifts in lung fluid in congestive heart failure patients [64]. Regional results have been validated with CT images

[67, 69, 45, 166] and radionuclide scanning [118] in the presence of pathologies such as atelectasis, pleural effusion, and pneumothorax. However, the solution of the inverse problem in real-time poses a significant challenge. D-bar methods have been generally regarded as computationally intensive, but in this chapter, we show that through parallelization and careful optimization of the computational routines, a fast implementation is capable of providing real-time images from the pairwise current injection system at CSU. For details regarding technical specifications and performance of the ACE1 EIT system at CSU, see [128].

For the ACE1 system, the frame rate of data collection is dependent on the number of electrodes used and the sample rate, which is the number of samples collected to obtain each demodulated voltage measurement (the demodulation routine uses a least mean-squares filter to obtain voltage measurements from the raw data). The frame rates for various numbers of electrodes and sample rates are shown in Table 2.1, as reported in [127]. For the purposes

TABLE 2.1. Frame rates (in frames/s) for the pairwise current injection system at CSU for various numbers of electrodes and measurement sample rates, as reported in [127].

Number of Electrodes	256 Samples	512 Samples	1024 Samples
16	66.4	52.6	31.8
17	62.1	46.8	29.7
18	59.0	44.3	28.3
19	56.0	41.8	26.8
20	53.2	39.8	25.6
21	50.9	37.8	24.3
22	48.3	36.2	22.8
23	45.8	34.5	22.1
24	44.3	33.3	21.1
25	42.8	31.7	20.4
26	40.9	30.7	19.6
27	39.2	29.5	18.9
28	37.9	28.5	18.0
29	36.7	27.3	17.4
30	35.5	26.5	16.7
31	33.9	25.6	16.2
32	33.2	24.9	16.0

of this dissertation, we define real-time to mean that the algorithm runtime is less than the data acquisition obtained with 32 electrodes at a sample rate of 1024 samples per voltage measurement. A fast implementation in MATLAB on a 12 core Mac Pro with two 2.66 GHz 6 core Intel Xeon processors and MATLAB's Parallel Computing Toolbox is capable of computing reconstructions at less than this data acquisition rate of 16 frames/s, or 0.0625 s/frame. This demonstrates the feasibility of CGO methods for real-time reconstructions.

In fact, we consider two options for the parallel computations. Ideally, in real-time reconstructions, data is collected, demodulated, and fed directly to the reconstruction algorithm, one frame at a time. In this configuration, only the loop over the z-values in the solution of the D-bar equation is trivially parallelizable. This accounts for over 95% of the computation time and can be used to obtain real-time reconstructions at a rate of 0.0621 s/frame on 7 cores on a coarse mesh of 562 elements, as reported in §2.4. This approach is structured as shown in Algorithm 1.

If a time delay of approximately one second is acceptable to the user, the algorithm can be parallelized over the frames. In this configuration, the data is collected and sent to a buffer from which multiple frames are sent to the reconstruction algorithm in batch. This approach results in an algorithm that is over 99% parallelizable, and the frame rate is even faster. As shown in §2.4, reconstructions were computed at a rate of 0.0215 s/frame on 64 cores or 0.0578 s/frame on 12 cores on a mesh of 1931 elements. The computational method for this approach is shown in Algorithm 2.

2.2. OUTLINE OF THE FAST IMPLEMENTATION

We now discuss the computational steps for the fast implementation in detail, including numerical approximations of various functions and operations, and numerical solution of

the D-bar equation. As described in [129], a finite-dimensional matrix approximation $\mathbf{L}_\sigma$ to the DN map Λ_σ is formed by first computing the discrete ND map $\mathbf{R}_\sigma$ and then forming its inverse. Denote by N the number of linearly independent current patterns and by L the number of electrodes. For bipolar current patterns that skip a electrodes as applied by ACE1, $N = L - \gcd(L, a+1)$. To compute $\mathbf{R}_\sigma$, first orthonormalize the matrix of bipolar current patterns to obtain the set $\{J_l^m\}$, $m = 1, \ldots, N$ and $l = 1, \ldots, L$, and then use the proper change-of-basis to the voltage matrix to arrive at the set $\{V_l^m\}$. Then the ND matrix can be approximated by

$$\mathbf{R}_\sigma(m,n) \approx \sum_{l=1}^{L} \frac{\Delta\theta}{A} J_l^m V_l^n = \frac{\Delta\theta}{A} \mathbf{V}^\top \mathbf{J},$$

where A is the area of an electrode and $\Delta\theta$ is the angular distance between electrodes. Since the voltages sum to zero, we can then compute $\mathbf{L}_\sigma = \mathbf{R}_\sigma^{-1}$.

The scattering transform is computed for $|k| \leq R$, where R is chosen empirically, which constitutes a regularization strategy as shown in [108]. For the fast implementation, we utilize a linearized approximation to the scattering transform, denoted by $\mathbf{t}^{\exp}$, which is defined by replacing $\psi|_{\partial\Omega}$ by its asymptotic behavior:

$$\mathbf{t}^{\exp}(k) := \int_{\partial\Omega} e^{i\bar{k}\bar{z}} (\Lambda_\sigma - \Lambda_1) e^{ikz} ds. \tag{36}$$

This approximation was first introduced in [163] and was later studied in [107] where it was shown that the D-bar equation (33) with $\mathbf{t}(k)$ replaced by $\mathbf{t}^{\exp}$ truncated to a disk of radius R in the k-plane has a unique solution which is smooth with respect to z, and the reconstruction is smooth and stable. Further, it was shown that no systematic artifacts are introduced when the method with $\mathbf{t}^{\exp}$ is applied to piecewise continuous conductivities.

Since difference images from a reference frame are being reconstructed here, we implement the scattering transform $\mathbf{t}_{\text{dif}}^{\text{exp}}$:

$$\mathbf{t}_{\text{dif}}^{\text{exp}}(k) := \int_{\partial\Omega} e^{i\bar{k}\bar{z}}(\Lambda_\sigma - \Lambda_{\sigma_{\text{ref}}})e^{ikz}ds, \tag{37}$$

introduced in [95], in which the DN map for the conductivity $\sigma = 1$ is replaced by that of a reference frame $\Lambda_{\sigma_{\text{ref}}}$.

The functions e^{ikz} and $e^{i\bar{k}\bar{z}}$ are expanded in the orthonormalized current pattern basis. The coefficients of the expansions of the functions $e^{ikz}|_{\partial\Omega}$ and $e^{i\bar{k}\bar{z}}|_{\partial\Omega}$ in the orthonormalized current pattern basis vectors are computed in the setup phase of the algorithm, and are denoted by $\mathbf{c_k} = [c_1(k), \ldots, c_N(k)]^\top$ and $\mathbf{d_k}$, respectively, where

$$\mathbf{c_k} = \mathbf{J}^\top * \exp(ik\vec{z})^\top \quad \text{and} \quad \mathbf{d_k} = \mathbf{J}^\top * \exp(i\bar{k}\vec{\bar{z}})^\top.$$

Then, denoting the discrete inner product over two vectors u and v of length L by $(u, v)_L$,

$$\begin{aligned} \mathbf{t}_{\text{dif}}^{\text{exp}}(k) &\approx \sum_{j=1}^{N}\sum_{m=1}^{N} c_m(k)d_j(k)(J^j, (\Lambda_\sigma - \Lambda_{\sigma_{\text{ref}}})J^m)_L \\ &\approx \sum_{j=1}^{N}\sum_{m=1}^{N} c_m(k)d_j(k)(\mathbf{L}_\sigma(j,m) - \mathbf{L}_{\sigma_{\text{ref}}}(j,m)). \end{aligned}$$

The fast evaluation of this formula is accomplished using inner products and vector operations.

A single grid and multigrid (2-grid) method were introduced in [109] for the fast computation of Lippmann-Schwinger type equations that arise in D-bar methods for EIT, closely based on the method of Vainikko [180]. The convolutions are computed as FFTs, and the solution of the resulting linear system by a matrix-free method, such as GMRES [154]. For

difference images, and in particular the data sets considered here, the frame-to-frame change in the data is sufficiently small that the method nearly always converges in one inner and one outer iteration of GMRES. In such cases, the 1-grid method is significantly faster than the 2-grid method described in [109].

To apply this method, we seek the solution $\mu_{\mathrm{R}}^{\exp}$ to (35) with $\mathbf{t} = \mathbf{t}^{\exp}$:

$$\mu_{\mathrm{R}}^{\exp}(z,k) = 1 + \frac{1}{(2\pi)^2}\int_{|k|\le R} \frac{\mathbf{t}^{\exp}(k')}{(k-k')\bar{k'}} e^{-i(zk'+\bar{z}\bar{k'})}\overline{\mu_{\mathrm{R}}^{\exp}(z,k')}dk'. \tag{38}$$

To construct the computational k-grid, we define the square $[-D,D]^2$ where $D \ge R$, and we choose $M = 2^m$ for some positive integer m. The step-size for the k-grid is defined to be $h = 2D/(M-1)$, and the final size of the grid is then $M \times M$. We further choose a computational z-grid of domain points, which need not be equally spaced. Equation (38) can be written compactly as the linear system

$$[I - \mathcal{A}\, T(\overline{\cdot})]\mu_{\mathrm{R}}^{\exp} = 1, \tag{39}$$

where T is the pointwise multiplication operator defined by

$$Tw(k) = \frac{\mathbf{t}_{\mathrm{R}}^{\exp}(k)}{4\pi\bar{k}} e^{-i(zk'+\bar{z}\bar{k'})}\; w(k), \tag{40}$$

and the action of the operator $\mathcal{A}$ is given by

$$\mathcal{A}w(k) = \frac{1}{\pi}\int_{|k|\le R} \frac{w(k)}{k-k'}dk'. \tag{41}$$

In our fast implementation, we compute T simultaneously for all z-values in the computational grid using vector operations, which in MATLAB is more efficient than computing each

T separately inside the z-loop shown in step 7 of Algorithm 1 and step 9 of Algorithm 2. The action of the operator $\mathcal{A}$ can be approximated by

$$\mathcal{A}w(k) \approx h^2 \text{IFFT}(\text{FFT}(\beta(k)) \cdot \text{FFT}(w(k))), \tag{42}$$

where $\beta(k) = (\pi k)^{-1}$ is the Green's function for the $\bar{\partial}$ operator, and $\cdot$ denotes element-wise multiplication. In MATLAB, this operation can be performed efficiently using IFFTN and FFTN. These are MATLAB's general n-dimensional FFT and IFFT, which generate less computational overhead than MATLAB's 2-D versions FFT2 and IFFT2.

Once the solution $\mu_{\text{R}}^{\text{exp}}(z,k)$ to the D-bar equation has been found, the conductivity is given by $\sigma(z) = (\mu_{\text{R}}^{\text{exp}})^2(z,0)$. Note that the D-bar equation requires the solution of the linear system (39) for all k-values in the computational grid, even though we are ultimately only interested in $k = 0$. It is also to be noted that this method allows for the reconstruction of σ pointwise in Ω, independent from any other z-value, and so it is trivially parallelizable over the values in the computational z-grid.

For maximum computational speed, we invoked MATLAB with the flag -singleCompThread, which limits MATLAB to a single computational thread. This choice is compatible with the Parallel Computing Toolbox, and will restrict each parallel computation to a single core, which proved to be advantageous in the runtimes.

2.3. A COMPARISON OF SOLVERS FOR THE D-BAR EQUATION

It should be noted that the system (39) is real-linear but (due to the presence of the complex conjugate) is not complex-linear, so one way to handle this is to separate real and imaginary parts and solve a real-linear system of size $2M^2 \times 2M^2$. The linear operator $[I - \mathcal{A}_R\, T_R(\overline{\cdot})]$ is non-sparse and nonsymmetric, and is therefore computationally expensive

Algorithm 1 Fast Parallelized D-bar Implementation for MATLAB: Parallelization Over Mesh Points

Setup Phase. Define parameters and compute functions independent of the dynamic DN data, including:
- Physical parameters
- Boundary parameterization and arclength function
- Current pattern matrix $\mathbf{J}$
- Computational grids in k-plane and z-plane
- Coefficients $\mathbf{c_k}, \mathbf{d_k}$ for expansions of $e^{ikz}|_{\partial\Omega}$, $e^{i\bar{k}\bar{z}}|_{\partial\Omega}$ used in $\mathbf{t}^{\exp}$

Demodulate the reference data set and form the DN matrix for the reference data set $\mathbf{L}_{\sigma_{\text{ref}}}$
Load a single frame of the measured data and demodulate
Compute matrix approximation to DN map, $\mathbf{L}_\sigma$
Compute $\mathbf{t}^{\exp}$ simultaneously for all k using vector operations
Compute the operator T simultaneously for all z using vector operations
parfor all z in domain **do**
    Solve D-bar equation for $\mu_{\text{R}}^{\exp}(z,k)$
    $\sigma(z) \leftarrow (\mu_{\text{R}}^{\exp})^2(z,0)$
end parfor

Algorithm 2 Fast Parallelized D-bar Implementation for MATLAB: Parallelization Over Frames

Setup Phase. Define parameters and compute functions independent of the dynamic DN data, including:
- Physical parameters
- Boundary parameterization and arclength function
- Current pattern matrix $\mathbf{J}$
- Computational grids in k-plane and z-plane
- Coefficients $\mathbf{c_k}, \mathbf{d_k}$ for expansions of $e^{ikz}|_{\partial\Omega}$, $e^{i\bar{k}\bar{z}}|_{\partial\Omega}$ used in $\mathbf{t}^{\exp}$

Load a batch of frames of the measured data and domain boundary points
Demodulate the reference data set and form the DN matrix for the reference data set $\mathbf{L}_{\sigma_{\text{ref}}}$
parfor all frames **do**
    Demodulate the voltage data
    Compute matrix approximation to DN map, $\mathbf{L}_\sigma$
    Compute $\mathbf{t}^{\exp}$ simultaneously for all k using vector operations
    Compute the operator T simultaneously for all z using vector operations
    for all z in domain **do**
        Solve D-bar equation for $\mu_{\text{R}}^{\exp}(z,k)$
        $\sigma(z) \leftarrow (\mu_{\text{R}}^{\exp})^2(z,0)$
    end for
end parfor

to compute explicitly, an effect which is exacerbated by the necessary separation of real and imaginary parts. The use of a direct solver such as LU factorization is therefore inefficient.

Several choices of matrix-free Krylov subspace method solvers suitable for nonsymmetric operators were therefore compared for the fast implementation. We tested MATLAB's built-in solvers BiCGSTAB, BiCGSTABl, CGS, GMRES, and TFQMR, as well as custom optimized versions of BiCGSTAB, GMRES, and TFQMR. For detailed information concerning these linear solvers, see [70, 154, 165, 170, 181].

To compare the solvers, the entire (nonparallelized) D-bar algorithm described here (with a z-mesh with 935 mesh points and a 32×32 k-mesh) was run on 10 frames of human data, using a very basic desktop PC (Gateway E-4610 desktop PC with a 1.86 GHz dual-core processor). Each linear solver was tested and timed using an error tolerance of 10^{-5}. The resulting runtimes are shown in Figure 2.1. Clearly, our custom algorithms performed better than the built-in MATLAB versions, and our custom GMRES was by far the fastest algorithm tested. Each of the algorithms tested gave extremely similar final reconstruction results.

GMRES implements the Generalized Minimal Residual method for solving a linear system. The basic idea in all Krylov subspace methods is to iteratively approximate a solution to the system $A\mathbf{x} = \mathbf{b}$ by a vector $\mathbf{x}_n$ in the Krylov subspace $\mathcal{K}_n$:

$$\mathcal{K}_n = \text{span}\{\mathbf{b}, A\mathbf{b}, A^2\mathbf{b}, \ldots, A^{n-1}\mathbf{b}\}.$$

The vector $\mathbf{x}_n \in \mathcal{K}_n$ is chosen so as to minimize the Euclidean norm of the residual $\mathbf{r}_n := A\mathbf{x}_n - \mathbf{b}$. The iteration over n is stopped when

$$\frac{||\mathbf{r}_n||_2}{||\mathbf{b}||_2} < \epsilon_{\text{tol}}, \tag{43}$$

where ϵ_{tol} is a user-defined error tolerance. The GMRES method in particular utilizes an Arnoldi iteration to obtain the approximation $\mathbf{x}_n$, and one feature of the GMRES algorithm is that (to minimize computational overhead and roundoff errors) the iteration is typically restarted after r steps, where the choice of r can be tricky to optimize. The restarts are called the "outer iterations," while the Arnoldi iterations themselves are called the "inner iterations."

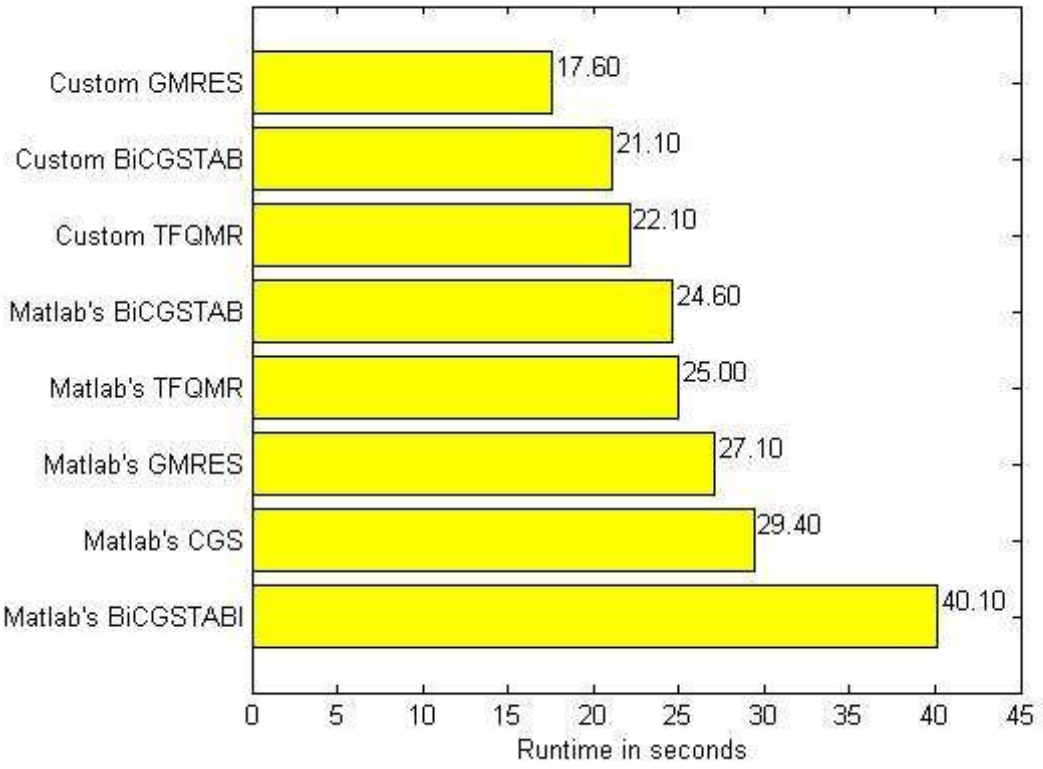

FIGURE 2.1. Runtimes (in seconds) for various matrix-free Krylov subspace solvers tested for use in solving the linear system (39). To compare the solvers, the entire (nonparallelized) D-bar algorithm described here (with a z-mesh with 935 mesh points, and a 32×32 k-mesh) was run on 10 frames of human data, using a Gateway E-4610 desktop PC with a 1.86 GHz dual-core processor. Each method was tested using an error tolerance of 10^{-5} in the numerical solver.

In our custom GMRES routine, which was roughly based on the template found in [18], we eliminated significant overhead due to repeated function calls and unnecessary option-checking and error-checking. Every time MATLAB's built-in GMRES (or any of MATLAB's built-in solvers, for that matter) is invoked, a call is made to an external .m file. Then, a series of subroutines is used within MATLAB's GMRES to determine which options the user has selected and to check for user errors. Moreover, each iteration of MATLAB's GMRES requires multiple function calls to the user-specified subroutine which computes the action of the linear operator, which in our case is the operator $[I - \mathcal{A}_R\, T_R(\overline{\cdot})]$. In MATLAB, calls to external functions involve some computational overhead which can become unwieldy when the operation must be performed thousands of times. We were therefore able to improve efficiency by embedding our code for GMRES and its necessary subroutines directly within the D-bar code. We also completely eliminated all unnecessary option- and error-checking, which greatly contribute to computational overhead when performed repeatedly. Finally, we took care to apply the operator $[I - \mathcal{A}_R\, T_R(\overline{\cdot})]$ to vectors within the algorithm as few times as possible, using the assumptions that the initial guess $\mathbf{x}_0$ will in general not satisfy (43), and that the algorithm usually converges after one outer and one inner iteration. This allows us to enter the algorithm assuming that we are going to perform exactly one iteration, so we may optimize the algorithm for this scenario, and we special-case the situation where additional iterations are required. This also gives us the luxury of not needing to optimize the restart value r. Similar customizations were applied to the BiCGSTAB and TFQMR algorithms tested. With these modifications, our custom algorithms greatly outperformed the built-in MATLAB versions.

One factor that greatly affects the runtime of any linear solver is the chosen value for the error tolerance ϵ_{tol}. We found that for the human dataset examined in this chapter,

for $\epsilon_{\text{tol}} = 10^{-4}$, the algorithm almost always converges in one inner and one outer iteration of GMRES. For $\epsilon_{\text{tol}} = 10^{-5}$, one outer iteration is still usually sufficient, but on very rare occasions two inner iterations will be required. For smaller error tolerances, the number of necessary iterations will increase. It is worth asking, therefore, whether $\epsilon_{\text{tol}} = 10^{-5}$, which will usually ensure only one total Arnoldi iteration and therefore a fast runtime, is sufficient to achieve desirable results, or if a smaller error tolerance will give visibly improved images. Based on our experiments, we determined that increased accuracy in the numerical solver leads to nearly identical images as those obtained with $\epsilon_{\text{tol}} = 10^{-5}$, but at a much greater computational cost.

To illustrate this point, we ran reconstructions using our custom GMRES with various error tolerances, recorded runtime information, and examined the resulting reconstructions. The entire (nonparallelized) D-bar algorithm described here (with a z-mesh of 5,916 mesh points and a 32×32 k-mesh) was run on 10 frames of human data, using a Dell Optiplex 790 with an Intel i7 3.4 GHz processor, for error tolerances $10^{-j}, j = 4, 5, \ldots, 12$. The resulting runtimes are shown in Figure 2.2. It is clear from this graph that runtimes increase sharply when $\epsilon_{\text{tol}} \leq 10^{-6}$, and again when $\epsilon_{\text{tol}} \leq 10^{-9}$, which indicates that these are the "break points" where additional iterations become necessary. To illustrate how little difference is apparent in the resulting reconstructions with additional iterations, Figure 2.3 shows one frame of human data reconstructed using GMRES with error tolerances $\epsilon_{\text{tol}} = 10^{-5}, 10^{-8}, 10^{-12}$. Our tests have yielded similar results with various other human datasets. We therefore are able to conclude that an error tolerance of $\epsilon_{\text{tol}} = 10^{-5}$ in the linear solver is sufficient to obtain high-quality reconstructions.

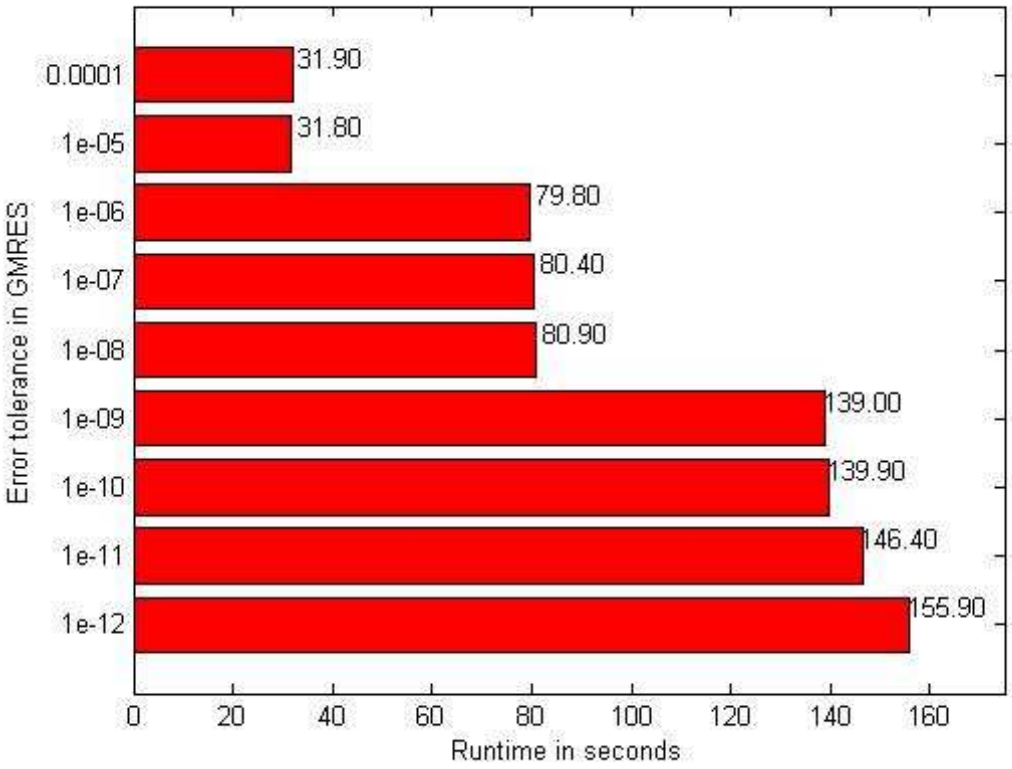

FIGURE 2.2. Runtimes (in seconds) corresponding to various error tolerances used in GMRES. To compare the error tolerances, the entire (nonparallelized) D-bar algorithm described here (with a z-mesh with 5,916 mesh points, and a 32×32 k-mesh) was run on 10 frames of human data, using a Dell Optiplex 790 with an Intel i7 3.4 GHz processor.

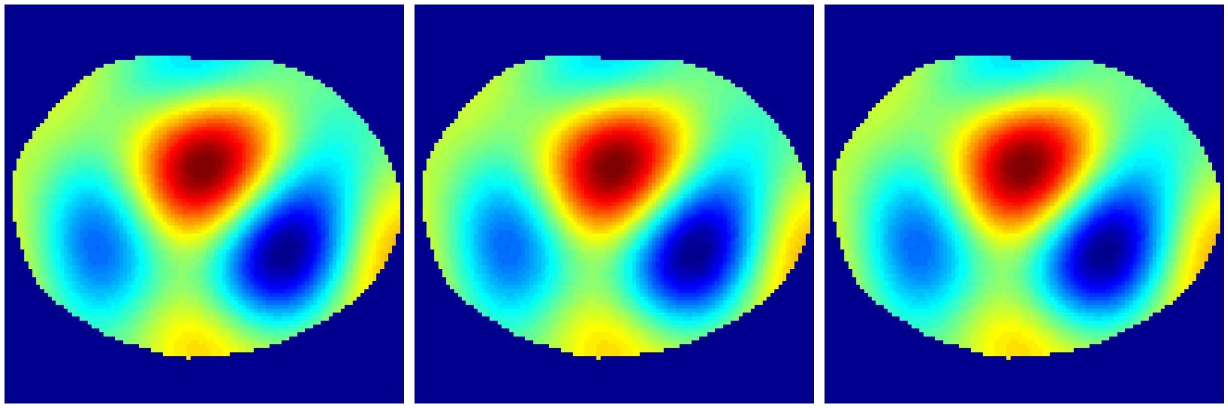

FIGURE 2.3. Reconstructions of human data corresponding to GMRES error tolerances $\epsilon_{\text{tol}} = 10^{-5}, 10^{-8}, 10^{-12}$ (left to right) used to solve the linear system (39). Note that the images appear nearly identical, indicating that little advantage is gained by decreasing the error tolerance, which necessitates additional iterations of GMRES.

2.4. RESULTS AND DISCUSSION

To demonstrate the feasibility of clinically useful real-time reconstructions using the D-bar method, we present reconstructions from data collected on the ACE 1 (Active Complex Electrode) EIT system at CSU. The ACE 1 system is a bipolar current injection system with 32 active electrodes operating at a user-specified frequency up to 200 kHz. For the results presented here, difference images of perfusion in a cross-section of the chest of a healthy male subject sitting upright and holding his breath are presented. 360 frames of data were collected at 16 frames/s at 125 kHz and current amplitude 0.823 mA, using the skip 0 current pattern. One frame was chosen as a reference data set and 359 difference images were computed using the fast implementation in §2.2 on a uniform k-mesh of size 16 by 16 (256 elements) and a truncation radius of $R = 3.8$. Numerical experiments indicate that this size of k-mesh is sufficient, and also the minimal acceptable k-mesh of size $2^m \times 2^m$ for these data sets. See §2.5 for a comparison of reconstructions on k-meshes with $m = 3, 4, 5,$ and 6, as well as error tables in the L^2 and L^∞ norms. All programming was in MATLAB and utilized the Parallel Computing Toolbox for the parallel solution of the D-bar equation.

In Tables 2.4 and 2.6 we compare the performance for each version of the algorithm with various numbers of cores in parallel on a 12 core Mac Pro with two 2.66 GHz 6 core Intel Xeon processors using three different spatial grids consisting of a coarse mesh with 562 elements, a medium mesh with 1,931 elements, and a fine mesh with 5,916 elements. In Tables 2.5 and 2.7 we compare the performance on a 64 core Linux system with four 2.3 GHz 16 core processors and 512 GB of RAM on the same three spatial grids.

Comparing all four tables, it is immediately clear that all runtimes utilizing the same number of cores were faster on the Mac Pro than on the Linux system, which is likely due in part to the difference in processor speed. It is also evident that while adding increasing

numbers of parallel cores continues to improve runtimes for Algorithm 2 in Tables 2.6 and 2.7, the runtimes for Algorithm 1 in Tables 2.4 and 2.5 reach maximum efficiency with a smaller number of cores, after which adding additional parallel cores actually slows the computation. This optimum number of cores increases as the z-mesh size increases.

It is well-known in parallel computing that the efficiency gained by adding additional parallel processors follows a "law of diminishing returns," embodied by Amdahl's law [10], which states that the maximum theoretical speedup s obtainable when using n processors in parallel is given by

$$s(n) = \frac{1}{(1-p) + \frac{p}{n}}, \tag{44}$$

where p is the proportion of the program that is parallelizable. One can see that as we increase n to ∞, the maximum theoretical speedup goes to $1/(1-p)$. To compute the actual speedup obtained using n processors, we use $s_{\text{actual}}(n) = t(1)/t(n)$, where $t(n)$ is the runtime with n cores in parallel.

In Figure 2.5, the actual speedups obtained on the Mac Pro using both versions of the parallel algorithm are shown along with the theoretical maximum speedups predicted by (44). One can see that the results obtained using Algorithm 2 are much closer to Amdahl's ideal values than the results obtained using Algorithm 1. We can also see that the larger the size of the z-mesh, the more efficient the parallelization becomes; this is predicted by (44) since increasing the number of elements in the z-mesh also increases p, the parallelizable portion of the program. In Figure 2.6 the same plots are included for the 64 core Linux system. It is evident that the additional cores do not provide speedup for Algorithm 1, and the divergence from the theoretically predicted speedup by Amdahl's Law increases with the number of cores, but Amdahl's Law also predicts the leveling off of speedup at around 20 to

25 cores; in fact, this happens at around 10 to 12 cores for parallelization over mesh values (Algorithm 1). However, for Algorithm 2, the speedup continues for all 64 cores, although it is clearly starting to level out at around 60 cores.

From the clinical perspective, difference images are sufficient for some applications, such as real-time detection of a pneumothorax or atelectasis. For other applications, such as distinguishing between blood, water, and mucus in the lung, absolute images may be required, which may require longer computation times. Some applications may also require finer spatial resolution than that presented here. However, the data is preserved for off-line or delayed reconstruction, and improvements such as the use of additional cores in parallel, faster FFTs, and faster processors are likely to yield improved runtimes in the future.

Figure 2.4 contains four frames in the reconstruction of the human chest data displayed in the three z-meshes to illustrate the resolution provided by these mesh choices. The figure depicts changes due to perfusion. The heart is at the top, and red represents high conductivity and blue low conductivity. The images are displayed on the same scale. While the topmost mesh is quite coarse, the lungs and heart are clearly visible, and changes are evident. The medium mesh is significantly better, and probably provides the best compromise for real-time imaging, but this implementation comes with the price of an approximately 1 second delay. The very fine mesh is included to illustrate highly desirable spatial resolution and the associated runtimes, given in Tables 2.4-2.7.

2.5. JUSTIFICATION FOR A COARSE K-MESH

Numerical computations were performed to study the effect of the choice of m when solving the D-bar equation on a k-mesh of size $2^m \times 2^m$. Computations were performed with $m = 3, 4, 5$, and 6. Very little change is evident in the reconstruction between reconstructions

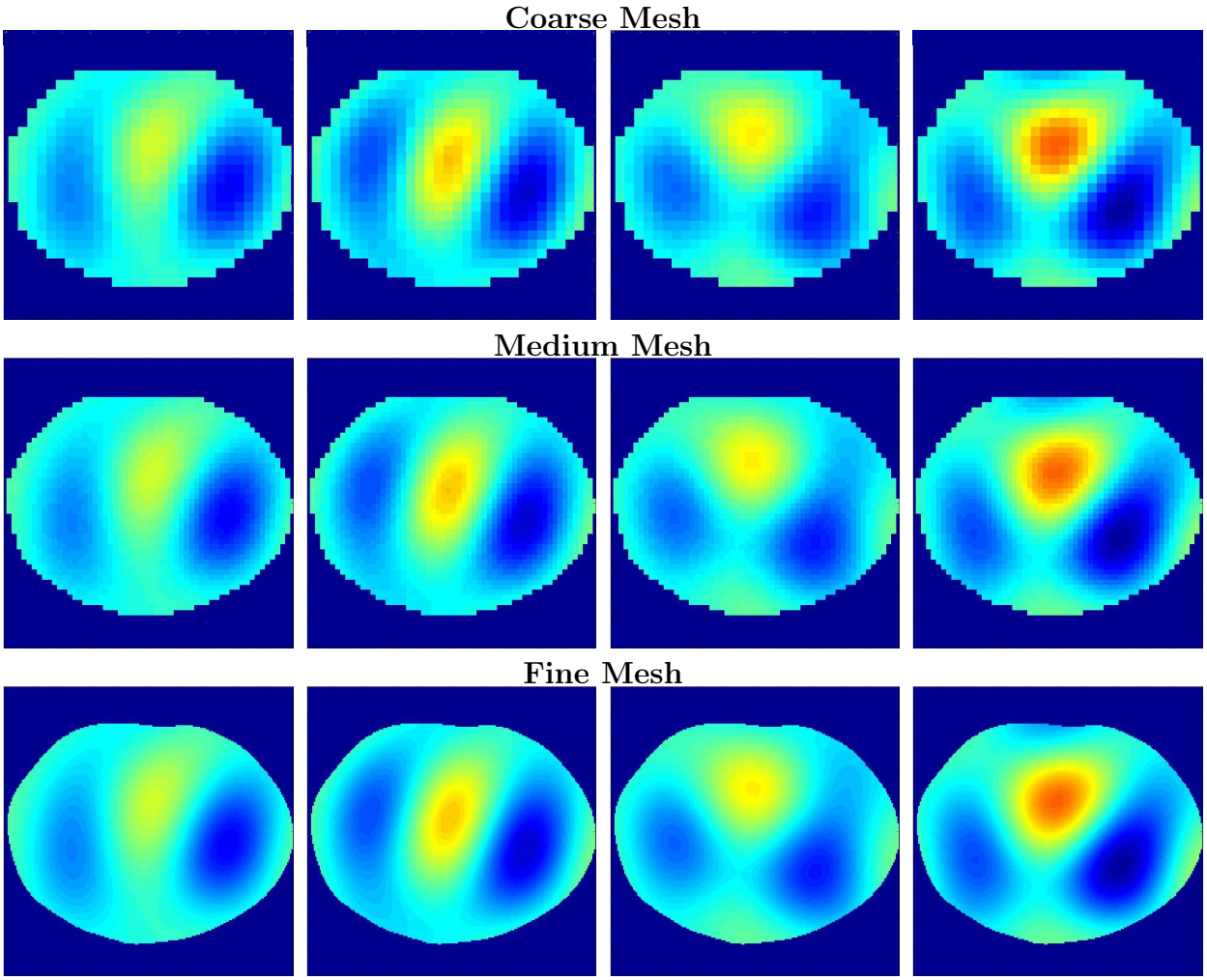

FIGURE 2.4. Reconstructions on the three z-meshes timed in this work of four frames in the sequence of 360 frames showing changes due to perfusion in the chest of a healthy human subject. The heart is at the top, and red represents high conductivity and blue low conductivity with respect to the reference frame. The images are displayed on the same scale.

from k-meshes of sizes $m = 4, 5$, and 6; see Figure 2.7. Choosing the image with $m = 6$, that is a 64×64 k-mesh as "truth," relative errors were computed in the L^2 and L^∞ norms for each frame. This choice of k-mesh is justifiable as a reference in the relative error computations because no further improvement is visibly seen by choosing a still finer mesh, and the lengths of computation time then become quite long for $m = 7$ and larger. In Table 2.2 the mean relative error, the maximum relative error, and the standard deviation over the 359 frames is reported. In Table 2.3 the effect of the size of the k-mesh on the runtime

for Algorithm 2 is provided. From the table of relative errors and reconstructions in Figure 2.7, it is evident that at least for this data set, the 16×16 k-mesh is sufficient. For general difference image reconstructions, we would also expect this to be sufficient, but recommend testing this parameter first.

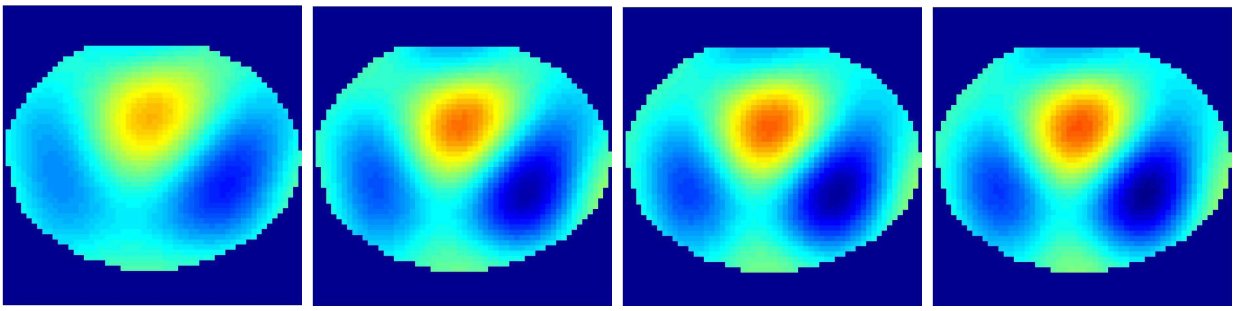

FIGURE 2.7. Reconstructions of the rightmost frame in Figure 2.4 computed by solving the D-bar equation on a k-grid of size $2^m \times 2^m$ with $m = 3, 4, 5,$ and 6, left to right. The images are displayed on the same scale.

TABLE 2.2. Comparison of the mean, maximum, and standard deviation over the 359 frames in the relative errors in the reconstructions computed by solving the D-bar equation on three sizes of k-mesh. The relative errors for each frame were computed by treating the reconstruction on a k-mesh of size 64×64 as truth.

	Relative Errors in L^∞ norm			Relative Errors in L^2 norm		
k-Mesh Size	Mean Err	Std Dev	Max Err	Mean Err	Std Dev	Max Err
8×8	2.29E-03	5.27E-04	4.13E-03	8.93E-04	1.76E-04	1.48E-03
16×16	7.24E-04	1.36E-04	1.20E-03	3.08E-04	6.12E-05	5.16E-04
32×32	2.43E-04	5.65E-05	4.21E-04	1.01E-04	2.15E-05	1.74E-04

TABLE 2.3. Runtimes (RT) in seconds for Algorithm 2 parallelized over 12 cores on a Mac Pro on the coarse and medium z-meshes, for various k-mesh sizes. The loop runtimes refer to the runtime for the parallelized loop over the frames. These results show that we can still easily achieve real-time results on the 32×32 k-mesh with an appropriately coarse z-mesh.

	Coarse grid (562 z-values)			Medium grid (1931 z-values)		
k-Mesh Size	Total RT	Loop RT	s/frame	Total RT	Loop RT	s/frame
8×8	4.7477	4.6552	0.0132	14.1798	14.0664	0.0395
16×16	6.7303	6.6036	0.0187	20.7440	20.5766	0.0578
32×32	16.1720	15.9394	0.0450	51.3855	51.0080	0.1431
64×64	68.8607	68.1446	0.1918	253.6598	252.1337	0.7066

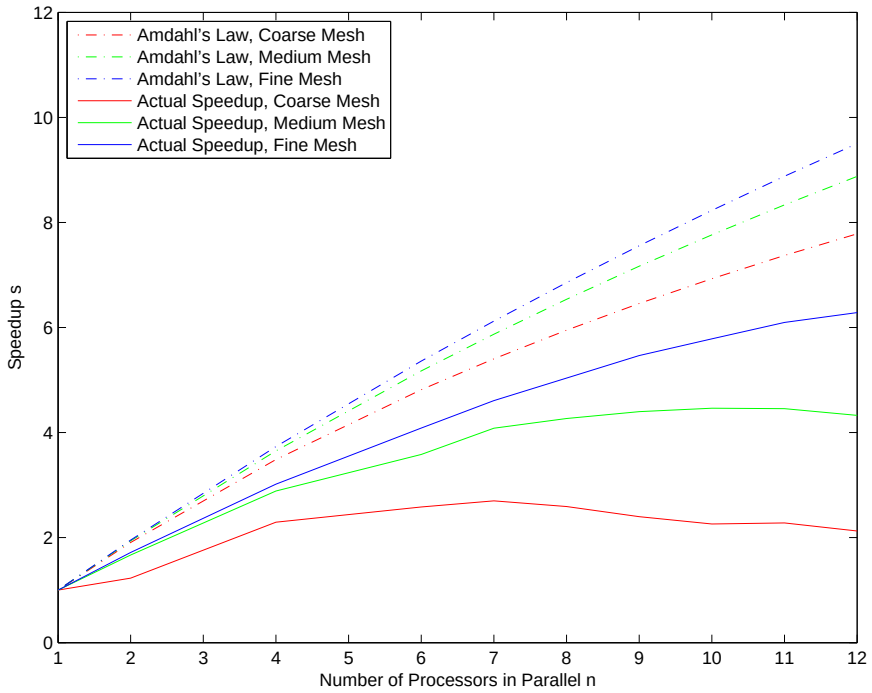

(A) Results with Algorithm 1 (parallelization over mesh points).

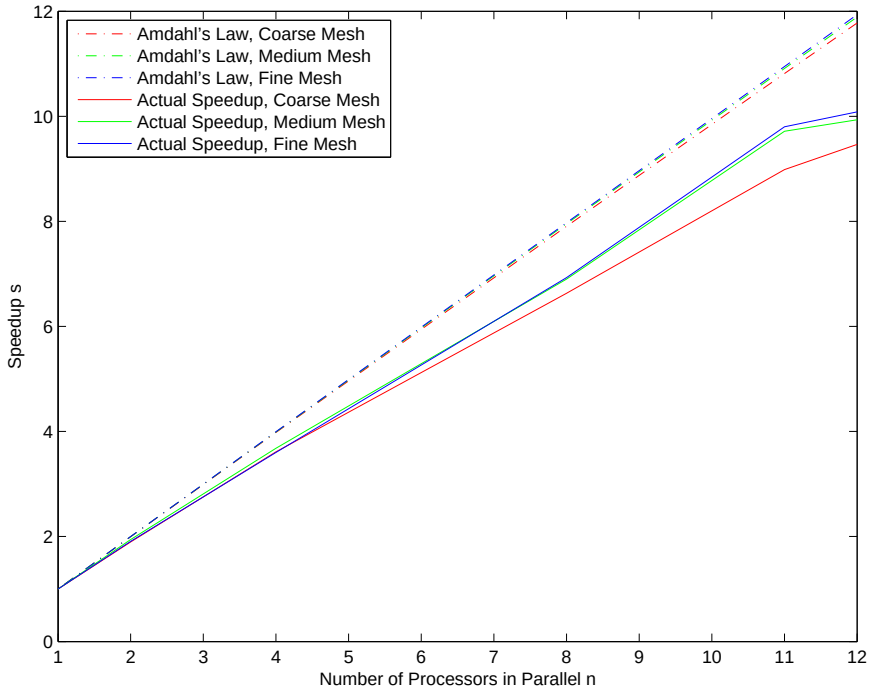

(B) Results with Algorithm 2 (parallelization over frames).

FIGURE 2.5. A comparison of Amdahl's law for maximum theoretical speedup (dashed lines) when using multiple cores with actual speedup obtained on a 12 core Mac Pro with two 2.66 GHz 6 core Intel Xeon processors (solid lines) using Algorithms 1 and 2.

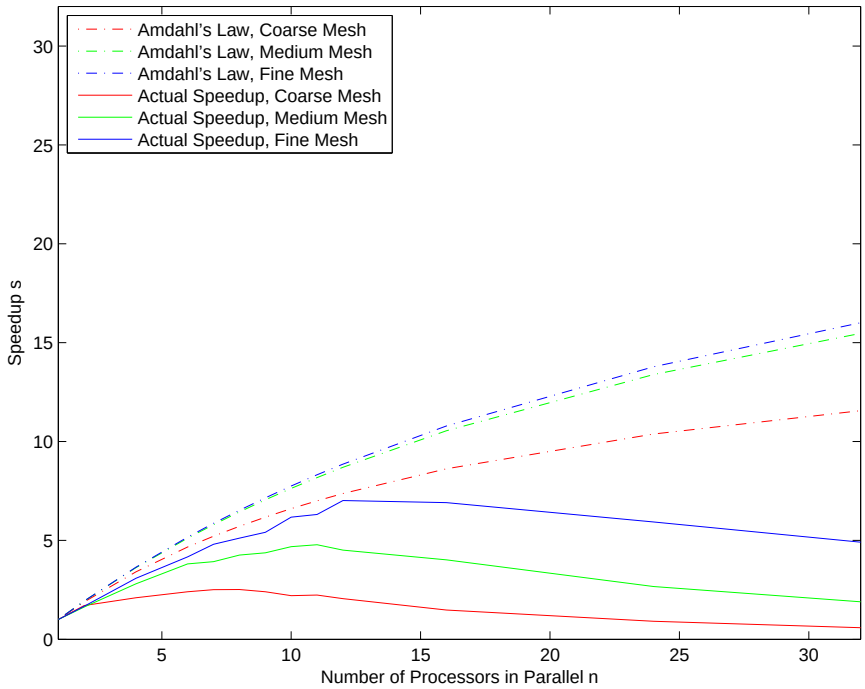

(A) Results with Algorithm 1 (parallelization over mesh points).

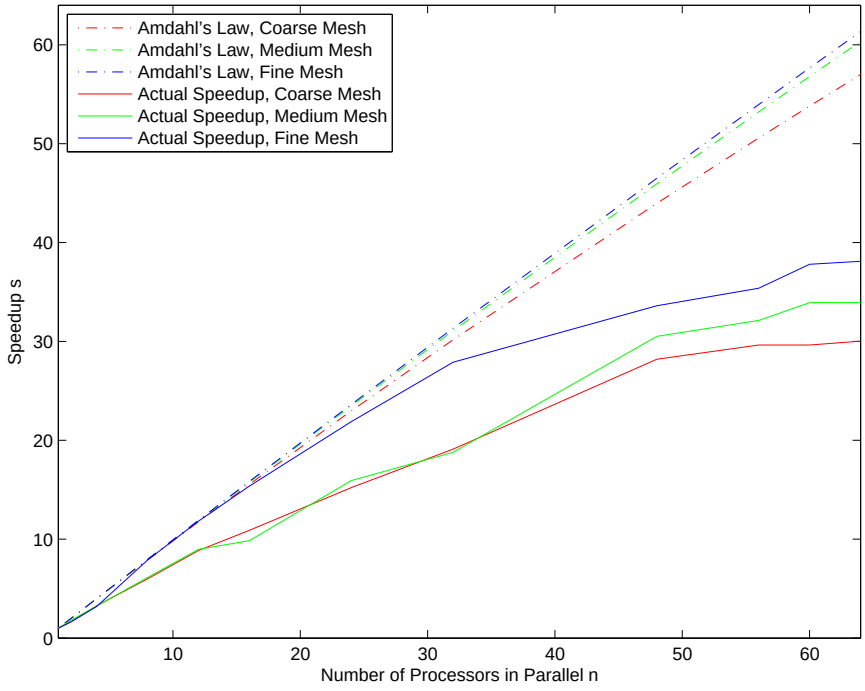

(B) Results with Algorithm 2 (parallelization over frames).

FIGURE 2.6. A comparison of Amdahl's law for maximum theoretical speedup (dashed lines) when using multiple cores with actual speedup obtained on a 64 core Linux system with four 2.3 GHz 16 core processors and 512 GB of RAM (solid lines) using Algorithms 1 and 2.

TABLE 2.4. Runtimes (RT) in seconds for Algorithm 1 (parallelization over mesh points) over 359 frames on a 12 core Mac Pro with two 2.66 GHz 6 core Intel Xeon processors. Here, the loop runtimes refer to the runtime for the parallelized loop over z-values. The fastest per-frame runtime for each mesh has been highlighted.

	Coarse grid (562 z-values)			Medium grid (1931 z-values)			Fine grid (5,916 z-values)		
Cores	Total RT	Loop RT	s/frame	Total RT	Loop RT	s/frame	Total RT	Loop RT	s/frame
1	60.1527	57.1906	0.1676	200.1049	193.7054	0.5574	615.3041	600.6027	1.7139
2	49.0169	45.0331	0.1365	119.8318	113.8120	0.3338	358.5238	343.1751	0.9987
4	26.2268	23.1675	0.0731	69.2834	62.6818	0.1930	203.8658	183.3158	0.5679
6	23.3147	20.3212	0.0649	55.8466	47.2439	0.1556	150.5782	130.0955	0.4194
7	22.2798	19.2730	0.0621	49.0180	41.6290	0.1365	133.5245	112.9986	0.3719
8	23.2349	20.2471	0.0647	46.8985	38.7851	0.1306	122.1320	101.3596	0.3402
9	25.0864	22.0817	0.0699	45.4834	37.2894	0.1267	112.5900	91.7865	0.3136
10	26.6466	23.6232	0.0742	44.8317	36.8733	0.1249	106.3704	85.4906	0.2963
11	26.3834	23.3987	0.0735	44.8993	36.9119	0.1251	100.9252	79.9427	0.2811
12	28.2897	25.3129	0.0788	46.2567	38.1605	0.1288	97.9265	77.0440	0.2728

TABLE 2.5. Runtimes (RT) in seconds for Algorithm 1 (parallelization over mesh points) over 359 frames on a 64 core Linux system with four 2.3 GHz 16 core processors and 512 GB of RAM. Here, the loop runtimes refer to the runtime for the parallelized loop over the frames. The fastest per-frame runtime for each mesh has been highlighted.

	Coarse grid (562 z-values)			Medium grid (1931 z-values)			Fine grid (5,916 z-values)		
Cores	Total RT	Loop RT	s/frame	Total RT	Loop RT	s/frame	Total RT	Loop RT	s/frame
1	70.6320	66.6039	0.1967	239.3496	231.0972	0.6667	767.5243	742.7878	2.1380
2	41.4227	38.4427	0.1154	146.6424	137.5511	0.4085	460.4769	435.7931	1.2827
4	33.5734	28.9639	0.0935	85.1865	75.0827	0.2373	248.8144	229.7575	0.6931
6	29.3667	24.9876	0.0818	62.8336	55.3416	0.1750	184.0372	164.8297	0.5126
7	28.1477	24.1555	0.0784	60.9286	51.3155	0.1697	159.8174	142.7302	0.4452
8	28.0048	24.1189	0.0780	56.1551	46.3121	0.1564	150.0559	127.9969	0.4180
11	31.5985	26.9765	0.0880	50.0699	42.1989	0.1395	121.6363	99.6636	0.3388
12	34.3986	30.1875	0.0958	53.0852	40.8174	0.1479	109.3473	91.8146	0.3046
16	47.7978	43.7131	0.1331	59.5714	50.6782	0.1659	111.0096	83.2492	0.3092
24	77.3859	72.0929	0.2156	89.5173	80.3598	0.2494	129.2778	104.2357	0.3601
32	120.9989	116.1762	0.3370	125.9324	115.8191	0.3508	156.2232	131.1057	0.4352

TABLE 2.6. Runtimes (RT) in seconds for Algorithm 2 (parallelization over frames) over 359 frames on a 12 core Mac Pro with two 2.66 GHz 6 core Intel Xeon processors. Here, the loop runtimes refer to the runtime for the parallelized loop over the frames. The fastest per-frame runtime for each mesh has been highlighted.

	Coarse grid (562 z-values)			Medium grid (1931 z-values)			Fine grid (5,916 z-values)		
Cores	Total RT	Loop RT	s/frame	Total RT	Loop RT	s/frame	Total RT	Loop RT	s/frame
1	63.5468	63.4370	0.1770	206.1180	205.9474	0.5741	623.0107	622.7078	1.7354
2	33.5405	33.4232	0.0934	106.1961	106.0467	0.2958	326.5889	326.2849	0.9097
4	17.5768	17.4568	0.0490	55.9864	55.8287	0.1560	173.0110	172.6940	0.4819
8	9.5713	9.4459	0.0267	29.8543	29.7101	0.0832	89.9303	89.6408	0.2505
11	7.0793	6.9545	0.0197	21.2018	21.0424	0.0591	63.5926	63.2956	0.1771
12	6.7303	6.6036	0.0187	20.7440	20.5766	0.0578	61.7965	61.4933	0.1721

TABLE 2.7. Runtimes (RT) in seconds for Algorithm 2 (parallelization over frames) over 359 frames on a 64 core Linux system with four 2.3 GHz 16 core processors and 512 GB of RAM. Here, the loop runtimes refer to the runtime for the parallelized loop over the frames. The fastest per-frame runtime for each mesh has been highlighted.

	Coarse grid (562 z-values)			Medium grid (1931 z-values)			Fine grid (5,916 z-values)		
Cores	Total RT	Loop RT	s/frame	Total RT	Loop RT	s/frame	Total RT	Loop RT	s/frame
1	83.0041	82.8420	0.2312	261.7762	261.5257	0.7292	837.1351	836.5582	2.3319
2	49.8535	49.5505	0.1389	145.1565	145.9066	0.4043	510.6861	510.2197	1.4225
4	25.3656	25.1796	0.0707	80.8684	80.6215	0.2253	262.7161	262.2612	0.7318
8	13.8435	13.6768	0.0386	42.7368	42.4592	0.1190	106.2459	105.8588	0.2959
12	9.3821	9.1925	0.0261	29.1641	28.8975	0.0812	70.7996	70.4057	0.1972
16	7.6005	7.3360	0.0212	26.5531	26.3019	0.0740	54.4559	54.0610	0.1517
24	5.4611	5.2730	0.0152	16.4534	16.1881	0.0458	38.2854	37.8909	0.1066
32	4.3561	4.1731	0.0121	13.9393	13.6828	0.0388	30.0064	29.5878	0.0836
48	2.9294	2.7678	0.0082	8.5636	8.3324	0.0239	24.9113	24.4925	0.0694
60	2.7924	2.6435	0.0078	7.7249	7.4911	0.0215	22.1673	21.7229	0.0617
64	2.7781	2.6219	0.0077	7.7157	7.4769	0.0215	21.9644	21.5439	0.0612

CHAPTER 3

AN A PRIORI D-BAR ALGORITHM

3.1. MOTIVATION AND OVERVIEW

In this chapter we now describe the second main project that is part of this dissertation. A portion of the work described here has been published in a pre-print version available on ArXiv [7]. Further publications are expected to be forthcoming in the near future.

A significant challenge in EIT imaging is the computation of static images with high-quality spatial resolution. Due to the ill-posedness of the inverse problem, finer details in the image are often lost in the presence of noisy measurements. Including prior information in the reconstruction algorithm has been shown to be one way to improve spatial resolution [14, 19, 38, 51, 55, 61, 62, 82, 83, 99, 124, 167, 172, 182]. This prior knowledge corresponds to a clinical situation in which we have a CT scan (or other similar data) for a human subject from which we may extract information regarding spatial locations of organ boundaries or conductivity estimates. When diagnosing and treating certain lung conditions, it is sometimes necessary to obtain repeated thoracic CT scans, each of which imparts a dose of ionizing radiation. EIT scans, on the other hand, have no ill effects. It is therefore highly desirable to use *a priori* information obtained from a CT or other scan to provide an improved EIT image, and then perform repeated harmless and comparatively inexpensive EIT scans in place of follow-up CT scans.

Reconstruction algorithms that involve the minimization of a cost functional, such as a Gauss-Newton algorithm, include the *a priori* information in the penalty term, penalizing reconstructions that deviate too greatly from the prior in a given norm. This technique

does not generalize to noniterative algorithms, and until now there has been no direct reconstruction method to utilize *a priori* information. The algorithm presented here therefore represents the first direct reconstruction method for EIT to incorporate *a priori* data.

3.2. OUTLINE OF THE A PRIORI METHOD

To motivate the *a priori* scheme, we first note that the scattering transform (30) can be written in terms of a scattering transform computed from a prior known conductivity distribution $\sigma_{\rm pr}$ in the form $\mathbf{t}(k) = \mathbf{t}_{\rm pr}(k) + \text{perturbation}(k)$. To this end, given $\sigma_{\rm pr}$, let $\Lambda_{\rm pr}$ denote the DN map corresponding to $\sigma_{\rm pr}$, let $\psi_{\rm pr}$ denote the CGO solution satisfying

$$\psi_{\rm pr}(z,k)|_{\partial\Omega} = e^{ikz}|_{\partial\Omega} - \int_{\partial\Omega} G_k(z-\zeta)(\Lambda_{\rm pr} - \Lambda_1)\psi_{\rm pr}(\cdot,k)ds(\zeta), \tag{45}$$

let $\mathbf{t}_{\rm pr}$ denote the scattering transform satisfying

$$\mathbf{t}_{\rm pr}(k) = \int_{\partial\Omega} e^{i\bar{k}\bar{z}}(\Lambda_{\rm pr} - \Lambda_1)\psi_{\rm pr}(z,k)ds(z), \tag{46}$$

and let $\mu_{\rm pr}$ denote the CGO solution satisfying

$$\mu_{\rm pr}(z,k) = 1 + \frac{1}{(2\pi)^2}\int_{\mathbb{R}^2} \frac{\mathbf{t}_{\rm pr}(k')}{\bar{k'}(k-k')} e^{-i(zk'+\bar{z}\bar{k'})}\overline{\mu_{\rm pr}(z,k')}dk'. \tag{47}$$

These equations are valid for $\sigma_{\rm pr} \in L^\infty(\Omega)$ by [13]. Subtracting (46) from the formula (32) for $\mathbf{t}(k)$, we see

$$\begin{aligned}
\mathbf{t}(k) - \mathbf{t}_{\rm pr}(k) &= \int_{\partial\Omega} e^{i\bar{k}\bar{z}}(\Lambda_\sigma\psi - \Lambda_1\psi - \Lambda_{\rm pr}\psi_{\rm pr} + \Lambda_1\psi_{\rm pr})ds \\
&= \int_{\partial\Omega} e^{i\bar{k}\bar{z}}(\Lambda_\sigma(\psi - \psi_{\rm pr}) - \Lambda_1(\psi - \psi_{\rm pr}) + (\Lambda_\sigma - \Lambda_{\rm pr})\psi_{\rm pr})ds.
\end{aligned}$$

Thus,

$$\mathbf{t}(k) = \mathbf{t}_{\mathrm{pr}}(k) + \int_{\partial\Omega} e^{i\bar{k}\bar{z}}[(\Lambda_\sigma - \Lambda_1)(\psi - \psi_{\mathrm{pr}}) + (\Lambda_\sigma - \Lambda_{\mathrm{pr}})\psi_{\mathrm{pr}}]ds. \tag{48}$$

Formula (48) suggests the following scheme. Given σ_{pr}, compute Λ_{pr} from a numerical forward solver, such as FEM, compute ψ_{pr} and $\mathbf{t}_{\mathrm{pr}}$ from (45) and (46), respectively, compute $\mathbf{t}(k)$ from (48), and use this $\mathbf{t}(k)$ in the D-bar method. However, this natural approach has several drawbacks when applied to noisy data. First of all, since the measured data Λ_σ has noise, it is necessary to compute $\mathbf{t}(k)$ on a truncated domain $|k| \leq R$. This means finer details encoded in large $|k|$ values of the prior will be lost. Second, the numerical computation of Λ_{pr} itself introduces error that is not necessarily a good match to the noise in Λ_σ. Thus, the term

$$\int_{\partial\Omega} e^{i\bar{k}\bar{z}}(\Lambda_\sigma - \Lambda_{\mathrm{pr}})\psi_{\mathrm{pr}}ds$$

is not an accurate perturbation, and errors in $\Lambda_\sigma - \Lambda_{\mathrm{pr}}$ will be amplified by the exponentially growing functions $e^{i\bar{k}\bar{z}}$ and ψ_{pr}.

An alternative approach motivated by (48) is to define an approximation to the scattering transform piecewise by

$$\mathbf{t}_{R_1,R_2}(k) := \begin{cases} \mathbf{t}(k), & |k| \leq R_1 \\ \mathbf{t}_{\mathrm{pr}}(k), & R_1 < |k| \leq R_2 \\ 0, & |k| > R_2 \end{cases}. \tag{49}$$

In this approximation, the perturbation term in (48) is neglected for $|k| > R_1$, and the entire scattering transform is truncated for some $R_2 \geq R_1$. Neglecting this term for $|k| > R_1$ is motivated by the fact that the size of R_1 is limited since $\mathbf{t}(k)$ will inevitably blow up for

larger values of $|k|$ in the presence of noisy data. Since the computation of $\mathbf{t}_{\text{pr}}$ is noise-free and in general much more numerically robust than the computation of $\mathbf{t}$, we may select R_2 to be significantly larger than R_1. The larger the value of R_2, the stronger the influence of the *a priori* information. The next question is then how to compute $\mathbf{t}_{R_1,R_2}$. For $|k| \leq R_1$, $\mathbf{t}(k)$ can be computed using (32), which is the same as computing $\mathbf{t}_R^{\text{BIE}}$, using the notation in [108]. To avoid the problems that arise from computing Λ_{pr}, the scattering transform $\mathbf{t}_{\text{pr}}$ can be computed directly from the definition of the scattering transform, provided $\sigma_{\text{pr}} \in C^2$. Then, defining

$$q_{\text{pr}} := \frac{\Delta\sqrt{\sigma_{\text{pr}}}}{\sqrt{\sigma_{\text{pr}}}},$$

the scattering transform $\mathbf{t}_{\text{pr}}$ is defined to be the nonlinear Fourier transform of q_{pr} [138]

$$\mathbf{t}_{\text{pr}}(k) := \int_{\mathbb{R}^2} e^{i\bar{k}\bar{z}} q_{\text{pr}}(z)\psi_{\text{pr}}(z,k)dz, \tag{50}$$

where ψ_{pr} is the solution of the Schrödinger equation (11), with $q = q_{\text{pr}}$. Once the scattering transform has been computed, the CGO solution μ can be solved from (35). We define $\tilde{\mu}_{R_2}$ as the solution to

$$\tilde{\mu}_{R_2}(z,k) = 1 + \frac{1}{(2\pi)^2}\int_{|k|\leq R_2} \frac{\mathbf{t}_{R_1,R_2}(k')}{\bar{k'}(k-k')} e^{-i(zk'+\bar{z}\bar{k'})}\overline{\tilde{\mu}_{R_2}(z,k')}dk'. \tag{51}$$

However, there is one more thing to note. The Green's function for the D-bar operator $\bar{\partial}_k$ is $\frac{1}{\pi k}$, and so the solution (35) to (33) is obtained from

$$\mu(z,k) = \lim_{R\to\infty}\left\{\frac{1}{\pi R^2}\int_{|k|\leq R}\mu(z,k)dk + \frac{1}{(2\pi)^2}\int_{|k|\leq R}\frac{\mathbf{t}(k')}{\bar{k'}(k-k')}e^{-i(zk'+\bar{z}\bar{k'})}\overline{\mu(z,k')}dk'\right\}, \tag{52}$$

where the first term tends to 1 as $R \to \infty$. Thus,

$$\tilde{\mu}_{R_2}(z,k) \approx \frac{1}{\pi R_2^2} \int_{|k|\le R_2} \mu(z,k)dk + \frac{1}{(2\pi)^2} \int_{|k|\le R_2} \frac{\mathbf{t}_{R_1,R_2}(k')}{\bar{k'}(k-k')} e^{-i(zk'+\bar{z}\bar{k'})} \overline{\tilde{\mu}_{R_2}(z,k')} dk'. \tag{53}$$

In practical computations, since $\tilde{\mu}_{R_2}(z,k)$ is unknown, the first integral is replaced by 1, that is, its limit as $R_2 \to \infty$. Approximating $\tilde{\mu}_{R_2}$ in this term by μ_{pr}, we have derived an equation for the approximation

$$\mu_{R_2}(z,k) = \frac{1}{\pi R_2^2} \int_{|k|\le R_2} \mu_{\text{pr}}(z,k)dk + \frac{1}{(2\pi)^2} \int_{|k|\le R_2} \frac{\mathbf{t}_{R_1,R_2}(k')}{\bar{k'}(k-k')} e^{-i(zk'+\bar{z}\bar{k'})} \overline{\mu_{R_2}(z,k')} dk'. \tag{54}$$

If the prior coincides with the correct conductivity distribution, this method converges and introduces no artifacts as $R_1, R_2 \to \infty$ by the convergence proof for the regularized D-bar method [108].

The strength of the prior, or its influence on the reconstruction, depends on R_2. If $R_2 = R_1$, then $\mathbf{t}_{R_1,R_2}(k) = \mathbf{t}^{\text{BIE}}_{R_1}(k)$, and the only influence of the prior on the reconstruction is in the term

$$\mu_{\text{int}}(z) := \frac{1}{\pi R_2^2} \int_{|k|\le R_2} \mu_{\text{pr}}(z,k)dk. \tag{55}$$

We can exert control over the amount of influence this term has by introducing a weighting parameter $\alpha \in [0,1]$ and writing

$$\mu_{R_2,\alpha}(z,k) = \alpha + (1-\alpha)\mu_{\text{int}}(z) + \frac{1}{(2\pi)^2} \int_{|k|\le R_2} \frac{\mathbf{t}_{R_1,R_2}(k')}{\bar{k'}(k-k')} e^{-i(zk'+\bar{z}\bar{k'})} \overline{\mu_{R_2,\alpha}(z,k')} dk', \tag{56}$$

which is equivalent to (51) if $\alpha = 1$ and (54) if $\alpha = 0$.

3.3. COMPUTATIONAL CONSIDERATIONS

We now describe the numerical details for the computation of the conductivity distribution $\sigma_{R_2,\alpha}$ corresponding to the CGO solution $\mu_{R_2,\alpha}$ to (56), including numerical approximations for necessary intermediate operators and functions.

As described in §2.2, we compute a finite-dimensional matrix approximation $\mathbf{L}_\sigma$ to the DN map Λ_σ. Since we are not in this case constructing difference images, we must also compute the discrete matrix approximation $\mathbf{L}_1$ of the DN map Λ_1 corresponding to homogeneous conductivity, by first numerically solving the forward conductivity problem to create simulated voltage data for the case where $\sigma \equiv 1 \in \Omega$. The method described previously for the computation of $\mathbf{L}_\sigma$ may then be used to compute $\mathbf{L}_1$ from this simulated data. In the fast implementation described in §2.2, we replaced the CGO solution $\psi|_{\partial\Omega}$ with its asymptotic behavior e^{ikz}. Here we invoke a fully nonlinear approximation to $\psi|_{\partial\Omega}$, found by numerically solving the boundary integral equation (29) at the center z_l of each electrode, as described in [84]. As in [12], we express the Faddeev Green's function G_k as

$$G_k(z) = \frac{1}{4\pi}\mathrm{Re}(\mathrm{EI}(ikz)),$$

where $\mathrm{EI}(z)$ is the exponential integral function, which in MATLAB can be computed easily using the built-in function: $\mathrm{EI}(z) \approx 2 * \mathrm{EXPINT}(z)$. To form a matrix approximation $\mathbf{\Gamma_k}$ for $G_k(z_l - \zeta_{l'})$, we must be careful of the logarithmic singularity that occurs when $l' = l$. We therefore discretize the surface of each electrode into S points z_{l_s}, $s = 1, \ldots, S$, and compute

$$\mathbf{\Gamma_k}(l, l') = \begin{cases} \frac{A}{2\pi}\mathrm{Re}(\mathrm{EXPINT}(ik(z_l - \zeta_{l'}))), & l' \neq l \\ \frac{1}{2\pi(S-1)}\sum_{s=1}^{S}\mathrm{Re}(\mathrm{EXPINT}(ik(z_l - \zeta_{l_s}))) & l' = l \end{cases}.$$

Denote by $\mathbf{b_k} = (b_1(k), \ldots, b_N(k))^\top$ and $\mathbf{c_k}$ the vectors of coefficients for the functions $\psi(z,k)|_{\partial\Omega}$ and $e^{ikz}|_{\partial\Omega}$, respectively, expanded in the basis of orthonormalized current patterns, so that $\psi(z,k)|_{\partial\Omega} \approx \mathbf{J}\mathbf{b_k}, e^{ikz}|_{\partial\Omega} \approx \mathbf{J}\mathbf{c_k}$. We may then approximate the convolution of G_k with $(\Lambda_\sigma - \Lambda_1)\psi$ for each $z = z_l$ as a finite-dimensional vector:

$$\int_{\partial\Omega} G_k(z-\zeta)(\Lambda_\sigma - \Lambda_1)\psi(\cdot,k)ds(\zeta) \approx \mathbf{\Gamma_k}\mathbf{J}(\mathbf{L}_\sigma - \mathbf{L}_1)\mathbf{b_k},$$

and the discrete version of (29) is

$$\mathbf{J}\mathbf{b_k} = \mathbf{J}\mathbf{c_k} - \mathbf{\Gamma_k}\mathbf{J}(\mathbf{L}_\sigma - \mathbf{L}_1)\mathbf{b_k}.$$

Multiplying through by the transpose of the orthonormal matrix $\mathbf{J}$ yields the linear system

$$[\mathbf{I} + \mathbf{J}^\top\mathbf{\Gamma_k}\mathbf{J}(\mathbf{L}_\sigma - \mathbf{L}_1)]\mathbf{b_k} = \mathbf{c_k}, \tag{57}$$

where $\mathbf{I}$ is the $N \times N$ identity matrix. In our implementation, this system was solved in MATLAB using the MLDIVIDE function.

The computation of the CGO solution ψ_{pr} corresponding to the prior is handled quite differently. From [138], we know μ_{pr} satisfies the Lippmann-Schwinger type equation (19) with $\mu = \mu_{\text{pr}}$:

$$\mu_{\text{pr}} = 1 - g_k * (q_{\text{pr}}\mu_{\text{pr}}). \tag{58}$$

The numerical solution of (58) uses the method in [109], which is based on ideas presented in [180], and a complete description of the computational steps can be found in [129]. In

short, we may write (58) as the linear system

$$[I + g_k * q_{\mathrm{pr}}(\cdot)]\mu_{\mathrm{pr}} = 1, \tag{59}$$

which is solved for μ_{pr} using a matrix-free method such as GMRES [154] or BiCGSTAB [181], which was used in our implementation, separating real and imaginary parts as required for the linear solver. The action of the linear operator on the left-hand side of (59) may be approximated efficiently using FFT and IFFT operations.

Once we obtain ψ_{pr}, the computation of $\mathbf{t}_{\mathrm{pr}}$ from its definition (50) is accomplished using simple numerical quadrature over the mesh of z-values. The integral μ_{int} is likewise found by applying numerical quadrature to the integrand μ_{pr}.

To obtain $\mu_{R_2,\alpha}(z)$, we must solve the equation (56) for each z, which involves modification of the computational methods described in [129]. We write (56) as the linear system

$$[I - \mathcal{A}T(\bar{\cdot})]\mu_{R_2,\alpha}(z) = \alpha + (1-\alpha)\mu_{\mathrm{int}}(z) \tag{60}$$

where the actions of the operators T and $\mathcal{A}$ are, analogously to (40) and (41), defined by

$$Tw(k) = \frac{\mathbf{t}_{R_1,R_2}(k)}{4\pi\bar{k}} e^{-i(zk' + \bar{z}\bar{k}')} w(k) \tag{61}$$

and

$$Aw(k) = \frac{1}{\pi} \int_{|k| \le R_2} \frac{w(k)}{k - k'} dk'. \tag{62}$$

Note that (60) is not complex-linear due to the presence of the conjugate operator, so it is necessary to solve real and imaginary parts separately. This system is solved by again

using a matrix-free solver such as BiCGSTAB, where the action of $\mathcal{A}$ can be approximated by FFT and IFFT operations.

From $\mu_{R_2,\alpha}$ we obtain the resulting conductivity distribution $\sigma_{R_2,\alpha} = \mu^2_{R_2,\alpha}(z,0)$, which is a result of both the EIT data Λ_σ and the *a priori* data encoded into $\mathbf{t}_{R_1,R_2}$ and μ_{int}.

3.4. CONSTRUCTING THE PRIOR CONDUCTIVITY DISTRIBUTION

The preceding method leaves one very obvious question: how do we obtain a reasonable estimate for the *a priori* conductivity distribution σ_{pr}? Any method employed will involve three distinct steps:

(1) Determine polygonal approximations to boundaries of regions of interest within the domain.

(2) Assign estimated conductivity values to each of these regions to obtain a discontinuous *a priori* distribution $\tilde{\sigma}_{\text{pr}}$. The values assigned to each region may be constant within the region, or may vary spatially within regions if desired.

(3) To satisfy the requirement that $\sigma_{\text{pr}} \in C^2(\Omega)$, mollify or otherwise smooth $\tilde{\sigma}_{\text{pr}}$ to obtain σ_{pr}.

Over the following pages, we will describe methodology for obtaining the approximate organ boundaries, as well two distinct methods for assigning constant conductivity estimates to regions of interest to obtain $\tilde{\sigma}_{\text{pr}}$. We acknowledge that many variations on these methods are possible, and these methods may be adapted accordingly to suit various applications. Additionally, we will describe iterative approaches that may improve upon the results obtained using one of these methods.

3.4.1. Obtaining approximate organ boundaries. Initially, knowledge is assumed of the spatial locations of boundaries for various domain inclusions (such as heart, lungs,

etc. for thoracic imaging) in the plane of the electrodes. In a clinical setting, this could be obtained by extracting the organ boundaries from a CT scan to obtain polygonal approximations to the actual organ boundaries.

In our experiments with simulated data, which will be described in section §3.5, we created polygonal boundaries representing heart, lungs, aorta, and spine within a circular domain to use as the organ boundaries for the simulation, and then created slightly different boundaries for the prior, as shown in Figure 3.1. This is representative of a realistic scenario where the true organ boundaries in the plane of the electrodes are unknown, and we approximate the boundaries from CT scan data.

In our tests with experimental tank data, which will be described in §3.7, we created an agar phantom representing a human heart and lungs. This phantom was photographed, and *a priori* organ boundaries were generated by clicking around the boundaries of the organs in the digital photograph, recording this geometric information, and then scaling the resulting polygonal boundaries to the correct dimensions. The experimental set-up and resulting *a priori* organ boundaries are shown in Figure 3.18 in §3.7. This process mimics a method that could be employed in a clinical setting, with a CT scan in place of the digital photograph. Organ boundary extraction (from a CT or other scan) could also likely be automated using image processing techniques based on Sobel or Canny edge detection (see [58] or [88], for example).

We next describe two possible methods for assigning conductivity values to the *a priori* conductivity distribution σ_{pr}. Each of these two methods describes the construction of a discontinuous *a priori* distribution $\tilde{\sigma}_{\text{pr}}$.

3.4.2. Constructing the prior: Blind Estimate Method. In the blind estimate method for assigning conductivity values to the prior, we simply make educated guesses for

the conductivity values within each approximate organ boundary. In a clinical setting these values can, for example, be estimated from literature sources wherein conductivity values for human tissue have been reported. Let $P \subset \Omega$ denote the polygonal region inside a particular approximate organ boundary and let $\{z_r\}$ be the finite set of points in the z-mesh used to construct σ_{pr}. An approximate constant conductivity value σ_P is selected for P, and we assign $\tilde{\sigma}_{\text{pr}}(z_n) = \sigma_P$ for all $z_n \in \{z_r\} \cap P$. We repeat this process for all organ boundaries used in the prior, obtaining the conductivity distribution $\tilde{\sigma}_{\text{pr}}$. Refinements to this process could be made by specifying regions of differing conductivities within individual organs if known inhomogeneities exist.

The blind estimate method is much computationally simpler and faster than the alternative extraction method which will be described next. However, if any pathologies have developed between the time of the initial CT scan and the time of the EIT scan, these pathologies will not be reflected in the prior, and their expression in the final reconstruction is therefore entirely dependent on the EIT data. The full *a priori* scheme with the blind estimate method for constructing the prior is outlined in Algorithm 3.

3.4.3. Constructing the prior: Extraction Method. In the extraction method, we first compute a reconstruction σ from the EIT data alone using the D-bar method described in §1.3. Note that the first-order approximation $\mathbf{t}^{\text{exp}}$ to the scattering transform as given in [94] could be used here as well to obtain an initial reconstruction. We then extract conductivity values from this reconstruction to obtain estimated values for the prior. This method has advantages over the blind estimate method in that pathologies not present in the CT scan data but that are apparent in the reconstruction σ may be included in the prior. Also, this method makes only geometric *a priori* assumptions, and makes no initial assumptions regarding conductivity values, and so relies less on estimates not associated with the

ALGORITHM 3 *A priori* scheme, Blind Estimate Method

Obtain *a priori* information and EIT data:
    - Form polygonal approximations to organ boundaries.
    - Collect EIT data and compute $\mathbf{L}_\sigma$.
    - Use FEM to simulate homogeneous data and compute $\mathbf{L}_1$.
Form computational grids for the k and z planes.
Make blind estimates for conductivity values to form $\sigma_{\rm pr}(z)$.
Compute $\sigma_{R_2,\alpha}(z)$:
    - Compute $q_{\rm pr} = \Delta\sqrt{\sigma_{\rm pr}}/\sqrt{\sigma_{\rm pr}}$.
    - Select R_1, R_2 with $R_1 \le R_2$.
    for $|k| \le R_2$ **do**
        - Solve (59) for $\mu_{\rm pr} = e^{-ikz}\psi_{\rm pr}$.
    end for
    for $|k| \le R_1$ **do**
        - Solve (57) for $\mathbf{b_k}$ to get $\psi|_{\partial\Omega} \approx \mathbf{J}\mathbf{b_k}$
        - Compute $\mathbf{t}(k)$ from (32).
    end for
    for $R_1 < |k| \le R_2$ **do**
        - Compute $\mathbf{t}_{\rm pr}(k)$ from (50).
    end for
    - Form $\mathbf{t}_{R_1,R_2}$.
    - Select α.
    for $z \in \Omega$ **do**
        - Compute $\mu_{\rm int}(z)$ from (55).
        - Solve (60) for $\mu_{R_2,\alpha}(z,\cdot)$.
        - Compute $\sigma_{R_2,\alpha}(z)$ from (21).
    end for

measured EIT data. The full *a priori* scheme with the extraction method for constructing the prior is outlined in Algorithm 4.

In our experiments with simulated data, we developed and used the following techniques for extracting approximate conductivity values from the reconstruction σ to be assigned to the lungs, heart, aorta, spine, and background in the prior. In what follows, we denote by $\{z_s'\}$ the finite set of points in the z-mesh used to construct σ, and the closed polygonal regions defined by specific organ boundaries by $P_{\rm heart}$, $P_{\rm spine}$, etc.

Lungs. We examine each lung in the σ reconstruction and compare the appearance of the lungs to the *a priori* approximate lung boundaries. If, based on the reconstruction

σ, the lungs appear to be free of pathology (i.e. there are no suspicious inhomogeneities within the regions $P_{\text{l lung}}$ and $P_{\text{r lung}}$), then the following method may be used. Find the set $\tilde{P}_{\text{l lung}} := \{z'_s\} \cap P_{\text{l lung}}$, and compute the average value

$$\sigma_{\text{l lung}} := \frac{1}{M} \sum_{m=1}^{M} \sigma(z'_m), \quad z'_m \in \tilde{P}_{\text{l lung}}, \tag{63}$$

where M denotes the number of points z'_m in $\tilde{P}_{\text{l lung}}$, and then assign $\sigma_{\text{pr}}(z_n) = \sigma_{\text{l lung}}$ for all $z_n \in \{z_r\} \cap P_{\text{l lung}}$. This process is then repeated for the right lung. On the other hand, if the reconstruction σ reveals possible lung pathologies in the form of inhomogeneities within a lung region, then the method can be revised in the following way. Assuming (without loss of generality) that one or more inhomogeneities appear in the left lung, divide the region $P_{\text{l lung}}$ into a finite number of connected subsets $S_j \subset P_{\text{l lung}}$, where each subset represents an area of fairly homogeneous conductivity in the reconstruction σ. Then for each S_j, compute the average conductivity over the points $z'_m \in \{z'_s\} \cap S_j$ and assign this value to $\tilde{\sigma}_{\text{pr}}(z_n)$ for $z_n \in \{z_r\} \cap S_j$.

Heart and aorta. To compute $\tilde{\sigma}_{\text{pr}}$ values for the heart region, one could potentially employ a similar method to that described for the lung regions. However, the position and shape of the reconstructed heart is more sensitive to noise level and truncation radius than the lung, and therefore using the anatomical position in the prior may include extraneous pixels. See Figure 3.3 as an example of how the size and shape of the reconstructed heart can vary. The aorta, on the other hand, is typically invisible in the reconstruction σ, so such a method could not be used to assign $\tilde{\sigma}_{\text{pr}}$ values within the aorta. The following method is therefore given as an alternative to the method used for the lungs. First, define the quantities

$$\sigma_{\max} := \max_{z'_m \in \{z'_s\} \cap \Omega} \{\sigma(z'_m)\}, \qquad \sigma_{\min} := \min_{z'_m \in \{z'_s\} \cap \Omega} \{\sigma(z'_m)\}, \tag{64}$$

and compute the value $\tau = \sigma_{\min} + c(\sigma_{\max} - \sigma_{\min})$ where $c \in (0.5, 1)$ is selected empirically. A good choice for c should optimally result in the set $H := \{z'_m \in \{z'_s\} \cap \Omega : \sigma(z'_m) \geq \tau\}$ being selected so as to be a connected subset of Ω and roughly the same size as the region P_{heart}, and such a c may vary depending on noise levels and choice of truncation radius in the computation of σ. We find the set H and compute

$$\sigma_{\text{heart}} := \frac{1}{M} \sum_{m=1}^{M} \sigma(z'_m), \quad z'_m \in H,$$

where M denotes the number of points in H. Finally, assign $\tilde{\sigma}_{\text{pr}}(z_n) = \sigma_{\text{heart}}$ for all $z_n \in \{z_r\} \cap P_{\text{heart}}$, and, since the aorta likely has conductivity values very similar to those of the heart, further assign these same values to $\tilde{\sigma}_{\text{pr}}$ in the region P_{aorta}.

Spine. Due to its small size, the reconstruction of the spine typically has very poor spatial resolution and its appearance and associated conductivity values can vary widely in the reconstruction σ in the presence of noise. Since we can usually assume that the spine is one of the most resistive objects in a thoracic EIT scan, we simply assign $\sigma_{\text{pr}}(z_n) = \sigma_{\min}$ for all $z_n \in \{z_r\} \cap P_{\text{spine}}$.

Background. We define the background to be the set $P_{\text{bg}} := \Omega - \cup_j P_j$ where each P_j corresponds to an organ boundary included in the prior, and assign values to P_{bg} according to the following method. Compute the quantities $\tau_1 = \sigma_{\min} + c_1(\sigma_{\max} - \sigma_{\min})$ and $\tau_2 = \sigma_{\min} + c_2(\sigma_{\max} - \sigma_{\min})$ where $c_1, c_2 \in (0, 1)$, $c_1 < c_2$. Find the set $B := \{z'_m \in \{z'_s\} : \sigma(z'_m) \in [\tau_1, \tau_2]\}$, and compute

$$\sigma_{\text{bg}} := \frac{1}{M} \sum_{m=1}^{M} \sigma(z'_m), \quad z'_m \in B,$$

where M denotes the number of points in B. Assign $\sigma_{\text{pr}}(z_n) = \sigma_{\text{bg}}$ for all $z_r \in \{z_n\} \cap P_{\text{bg}}$. As with the value c used for the heart, the values c_1 and c_2 must be selected empirically, and may

once again vary depending on noise levels and choice of truncation radius in the computation of σ. Since the lungs, which have low conductivity compared to the background, tend to dominate the reconstruction, it is usually advantageous to choose c_1, c_2 to be skewed to the upper end of the scale $(0, 1)$. Well-chosen c_1 and c_2 should result in the set B excluding most of the region corresponding to the lungs and spine, as well as the high conductivity region inside the heart.

ALGORITHM 4 *A priori* scheme with Extraction Method

Obtain *a priori* spatial information and EIT data:
    - Form polygonal approximations to organ boundaries.
    - Collect EIT data and compute $\mathbf{L}_\sigma$.
    - Use FEM to simulate homogeneous data and compute $\mathbf{L}_1$.
Compute conductivity $\sigma(z)$ using standard D-bar methods:
    - Form computational grids for the k and z planes for both σ and σ_{pr}.
    - Select a truncation radius R_1.
    for $|k| < R_1$ **do**
        - Solve (57) for $\mathbf{b_k}$ to get $\psi|_{\partial\Omega} \approx \mathbf{J}\mathbf{b_k}$
        - Compute $\mathbf{t}(k)$ from (32).
    end for
    for $z \in \Omega$ **do**
        - Solve the (R_1-truncated) equation (35) for $\mu(z, \cdot)$.
        - Compute $\sigma(z)$ from (21).
    end for
Extract conductivity values from $\sigma(z)$ to form σ_{pr}.
Compute $\sigma_{R_2,\alpha}(z)$:
    - Compute $q_{\text{pr}} = \Delta\sqrt{\sigma_{\text{pr}}}/\sqrt{\sigma_{\text{pr}}}$.
    - Select $R_2 \geq R_1$.
    for $|k| \leq R_2$ **do**
        - Solve (59) for $\mu_{\text{pr}} = e^{-ikz}\psi_{\text{pr}}$.
    end for
    for $R_1 < |k| \leq R_2$ **do**
        - Compute $\mathbf{t}_{\text{pr}}(k)$ from (50).
    end for
    - Form $\mathbf{t}_{R_1,R_2}$.
    - Select α.
    for $z \in \Omega$ **do**
        - Compute $\mu_{\text{int}}(z)$ from (55).
        - Solve (60) for $\mu_{R_2,\alpha}(z, \cdot)$.
        - Compute $\sigma_{R_2,\alpha}(z)$ from (21).
    end for

3.4.4. Iterative approaches. The *a priori* schemes described in the previous pages may be used alone to obtain a reconstruction $\sigma_{R_2,\alpha}$, but there is potential for further refinement of spatial resolution through the use of iterative approaches. The motivation is to take advantage of the enhanced spatial resolution in $\sigma_{R_2,\alpha}$ to construct a new prior that is more accurate than the original in terms of conductivity values and possible pathologies. We may include in this updated prior any new information that appears in the reconstruction $\sigma_{R_2,\alpha}$. This may be especially advantageous if the blind estimate method was used to construct the original prior, but the patient has since developed some pathology that is visible in the EIT data. Another situation where iteration may provide enhanced results is if we desire to use the extraction method, but the reconstruction σ has very poor spatial resolution. In §3.5 we provide an example of the first of these scenarios, using simulated data.

The computational steps in these iterative approaches are the following: (1) obtain the reconstruction $\sigma_{R_2,\alpha}$, using either the blind estimate or extraction method to assign conductivity values to the prior, (2) use the extraction method described in §3.4.3 to extract conductivity values from $\sigma_{R_2,\alpha}$ (rather than from σ), (3) use these extracted conductivity values to form an updated prior σ'_{pr}, (4) repeat the *a priori* scheme using the original EIT data with the updated prior σ'_{pr} to obtain an updated reconstruction $\sigma'_{R_2,\alpha}$. This entire process could potentially be repeated again if desired to obtain a second iterate $\sigma''_{R_2,\alpha}$.

3.5. RESULTS FROM SIMULATED DATA

We now present the results of our test problem using simulated data. In this test problem, we simulate a situation in which *a priori* information is available from a previous CT scan, but the patient has since developed a pleural effusion in one lung. We tested the previously described *a priori* scheme using both the blind estimate and extraction methods for assigning

conductivity values, and an iteration step as described above was performed on the results from the reconstructions using the blind estimate method.

We assumed that the organ boundaries (without pleural effusion) were given by the organ boundaries indicated by the solid line in Figure 3.1, and we assumed a circular domain of radius 143.2 mm. We therefore created a phantom with these organ boundaries, domain shape, and dimensions. Conductivity values were assigned to the phantom heart, lungs, aorta, and spine, and the FEM method with the complete electrode model including contact impedance described in [135] was used to generate voltage data. To simulate a pleural effusion, conductivity was increased in the phantom in the bottom of the left lung. We will use the convention that the left lung appears on the left-hand side of the image. The phantom with assigned conductivity values is shown in Figure 3.2. Random zero-mean Gaussian noise was added to the simulated voltages at 0%, 0.1%, and 0.2% of the maximum voltage values; the D-bar reconstructions σ using the method of §1.3 for each of the three noise cases are shown in Figure 3.3. All reconstructions in this section, including the reconstructions σ and the results of the *a priori* schemes, were computed using a z-mesh with 101×101 elements, $R_1 = 3.8$, and we tested values $R_2 \in \{3.8, 5.0, 7.5, 10\}$, and $\alpha \in \{0, 0.5, 0.75, 0.9\}$.

3.5.1. Blind estimate method applied to simulated data. We assigned "blind estimate" *a priori* conductivity values representing a phantom with two homogeneous lungs with conductivity 0.200 S/m, as shown on the right in Figure 3.2, in contrast to the actual values displayed on the left in Figure 3.2. The values for the background, heart, aorta, and spine differed slightly from the actual values. These "blind estimates" were used for all three noise cases, and are given in Table 3.1. Reconstructions using the blind estimate method can be seen in Figures 3.5, 3.6, 3.7.

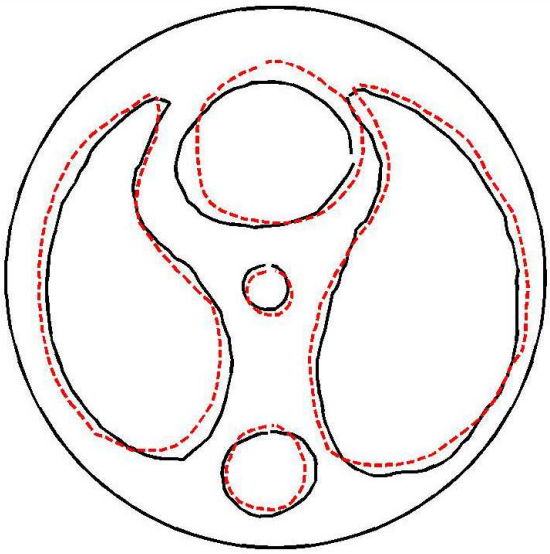

FIGURE 3.1. Solid line: simulated organ boundaries representing heart, lungs, aorta, and spine within a circular domain, used to generate simulated data. Dashed line: polygonal approximations of organ boundaries used as geometric *a priori* information in our experiments with simulated data.

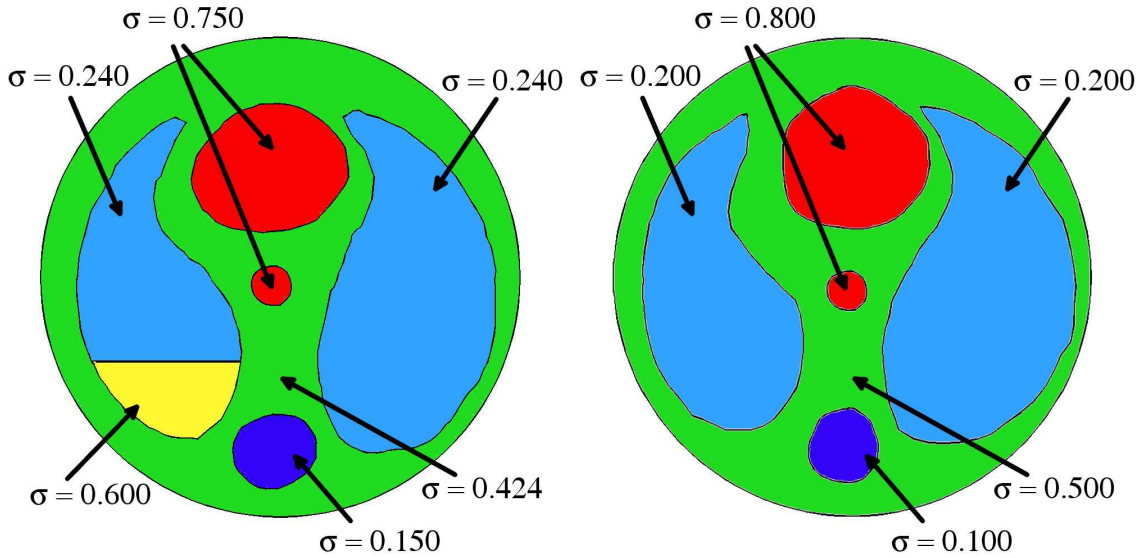

FIGURE 3.2. Conductivity values for the pleural effusion phantom (left) and the initial blind estimate prior (right). All conductivity values are in S/m.

Given the obvious lung pathology apparent in the reconstructions, we then performed an iteration step wherein the left lung was divided into two regions, which we shall refer to as the "lung top" and "lung bottom," separated by a horizontal line segment. We computed conductivity values for the iterate σ'_{pr} separately in each of these two regions, using the

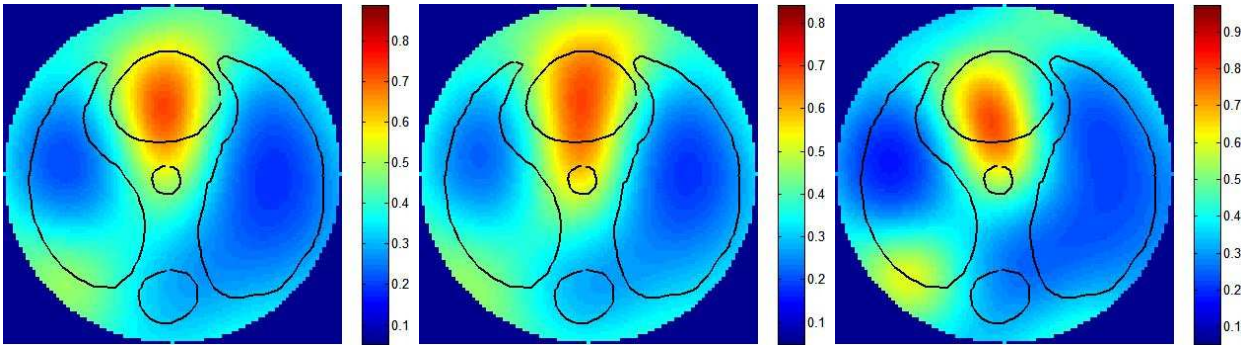

(A) Noise level = 0%. (B) Noise level = 0.1%. (C) Noise level = 0.2%.

FIGURE 3.3. Plots of the reconstructions σ from the simulated data experiments, computed using the regularized D-bar method of §1.3 (see also lines 5–15 of Algorithm 4) with truncation radius $R_1 = 3.8$, at noise levels 0%, 0.1%, and 0.2%, with superimposed true organ boundaries. Each noise case is plotted on its own scale; these scalings will be used for all plots concerning the simulated data at each noise level within this work.

methods described in §3.4.3 to extract conductivity values from the $\sigma_{R_2,\alpha}$ reconstruction with $R_2 = 5.0$ and $\alpha = 0.75$. In the computation of the values for the heart, aorta, and background, we selected values $c = 0.85$, $c_1 = 0.25$, and $c_2 = 0.95$; for simplicity, we used these same values in all noise cases. The resulting conductivity values used in σ'_{pr} are also given in Table 3.1.

The location of the dividing line between lung top and lung bottom was chosen by visually inspecting the $\sigma_{R_2,\alpha}$ reconstructions and selecting a horizontal line at which to form the division. For simplicity, we used the same approximate dividing line in all three noise cases. This approximate dividing line is compared to the actual lung division used to create the phantom in Figure 3.4. The reconstructions resulting from the iteration step can be seen in Figures 3.8, 3.9, and 3.10.

It is evident from the reconstructions in Figures 3.5, 3.6, 3.7 that with or without noise the blind estimate method without iteration detects the pleural effusion provided a very small value of α is not combined with a small value of R_2. The case $\alpha = 0$ and $R_2 = 3.8$ corresponds to using only μ_{int} as in equation (54) and the scattering transform from the

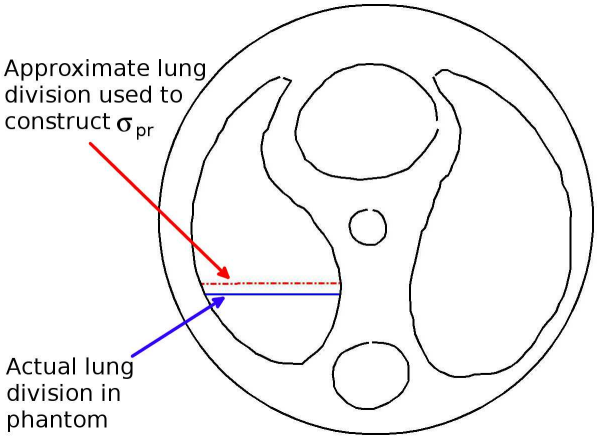

FIGURE 3.4. Locations of dividing line between the "lung top" and "lung bottom." The dividing line used in the phantom is indicated by a solid line. The approximate dividing line (dashed line) was used in the extraction method and the iteration step for the blind estimate method, and was obtained by visually inspecting the $\sigma_{R_2,\alpha}$ reconstructions.

regularized D-bar method without a prior. Increasing α and decreasing R_2 weakens the influence of the prior. In the case of a strong prior, the prior dominates the reconstruction in the blind estimate method, resulting in good spatial resolution of organ boundaries, but poor detection of the effusion. Adding the iteration step described in §3.4.4 results in excellent detection of the effusion in every case, and the aorta and spine can be clearly seen with excellent spatial accuracy even with a prior of medium weight, such as $\alpha = 0.5, R_2 = 7.5$.

TABLE 3.1. Conductivity values in S/m for the phantom as well as the "blind estimate" $\tilde{\sigma}_{\text{pr}}$ values assigned, along with values assigned to $\tilde{\sigma}'_{\text{pr}}$ in the subsequent iteration step, for each of the three noise cases.

	Back-ground	Heart	Left Lung top	Left Lung bottom	Right Lung	Aorta	Spine
Used in phantom	0.424	0.750	0.240	0.600	0.240	0.750	0.150
"Blind estimates" used in $\tilde{\sigma}_{\text{pr}}$	0.500	0.800	0.200	0.200	0.200	0.800	0.100
Used in $\tilde{\sigma}'_{\text{pr}}$, 0% noise	0.431	0.798	0.261	0.364	0.233	0.798	0.187
Used in $\tilde{\sigma}'_{\text{pr}}$, 0.1% noise	0.427	0.767	0.274	0.333	0.233	0.767	0.178
Used in $\tilde{\sigma}'_{\text{pr}}$, 0.2% noise	0.450	0.858	0.247	0.428	0.247	0.858	0.163

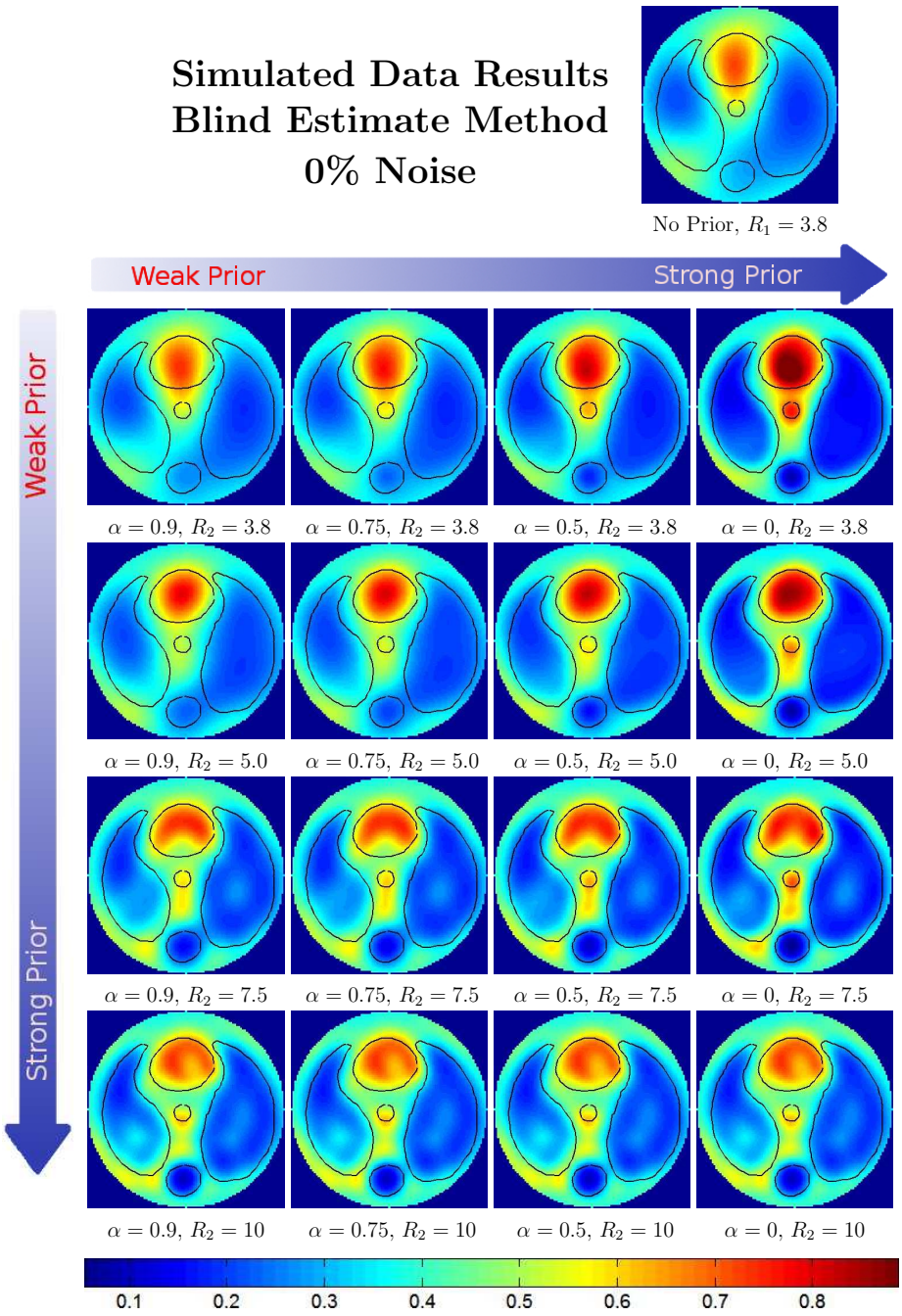

FIGURE 3.5. Reconstructions $\sigma_{R_2,\alpha}$ for the 0% noise case with simulated data, using the *a priori* scheme with the blind estimate method (before iteration step), with various values of α and R_2. The reconstruction with no prior is at the top for comparison. The strength of the prior increases moving left to right and top to bottom. The scale bar at the bottom applies to all reconstructions at this noise level.

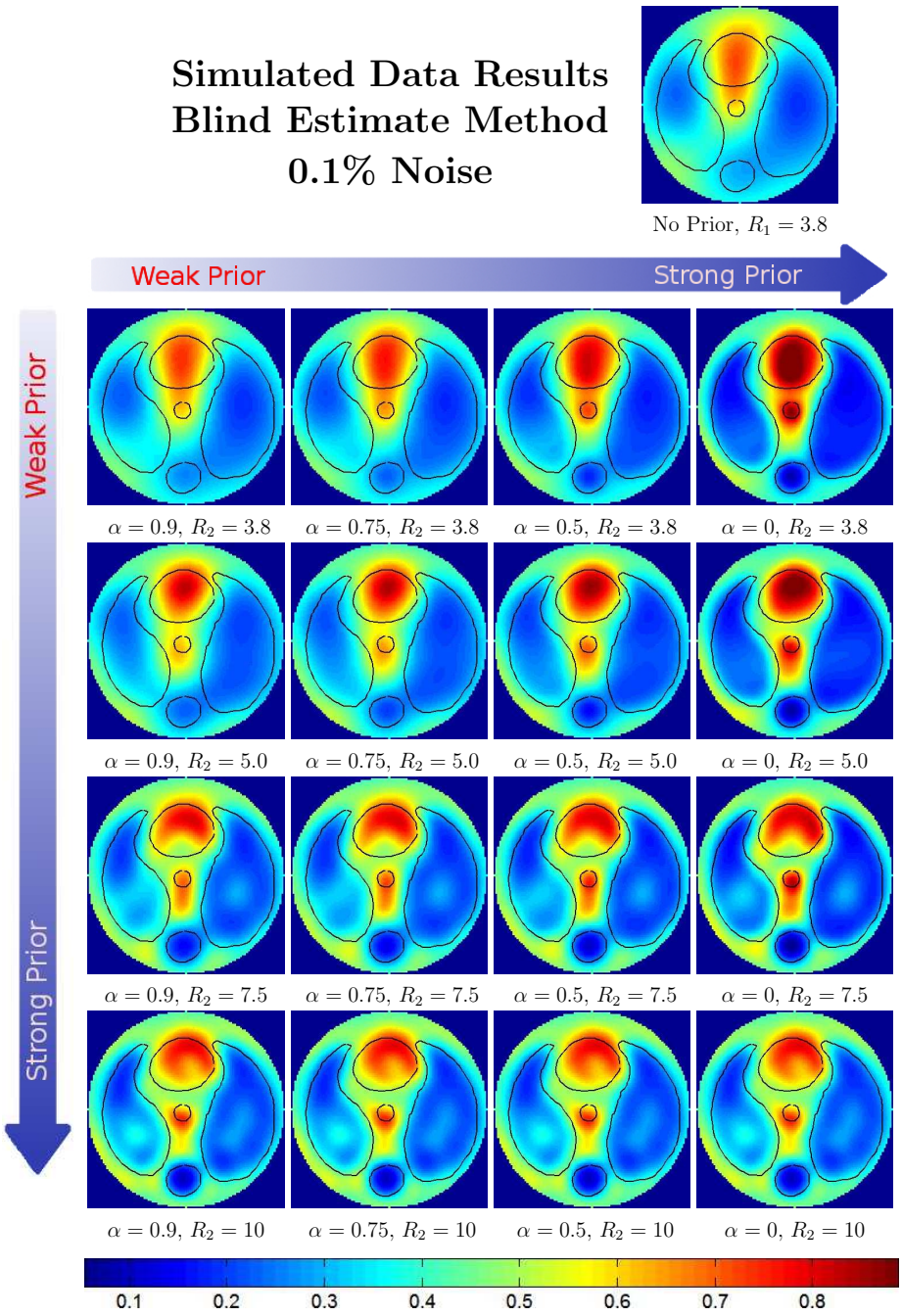

FIGURE 3.6. Reconstructions $\sigma_{R_2,\alpha}$ for the 0.1% noise case with simulated data, using the *a priori* scheme with the blind estimate method (before iteration step), with various values of α and R_2. The reconstruction with no prior is at the top for comparison. The strength of the prior increases moving left to right and top to bottom. The scale bar at the bottom applies to all reconstructions at this noise level.

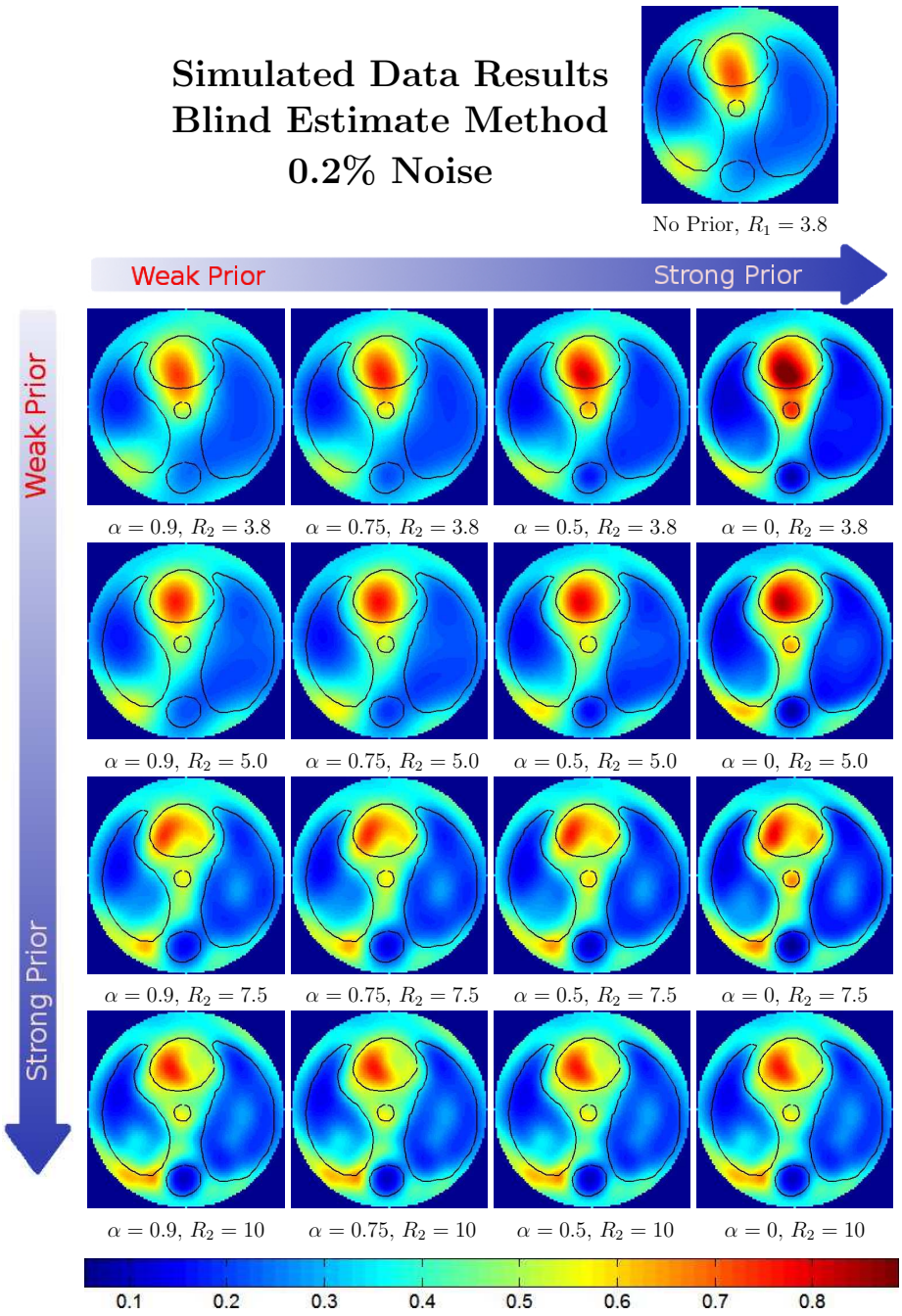

FIGURE 3.7. Reconstructions $\sigma_{R_2,\alpha}$ for the 0.2% noise case with simulated data, using the *a priori* scheme with the blind estimate method (before iteration step), with various values of α and R_2. The reconstruction with no prior is at the top for comparison. The strength of the prior increases moving left to right and top to bottom. The scale bar at the bottom applies to all reconstructions at this noise level.

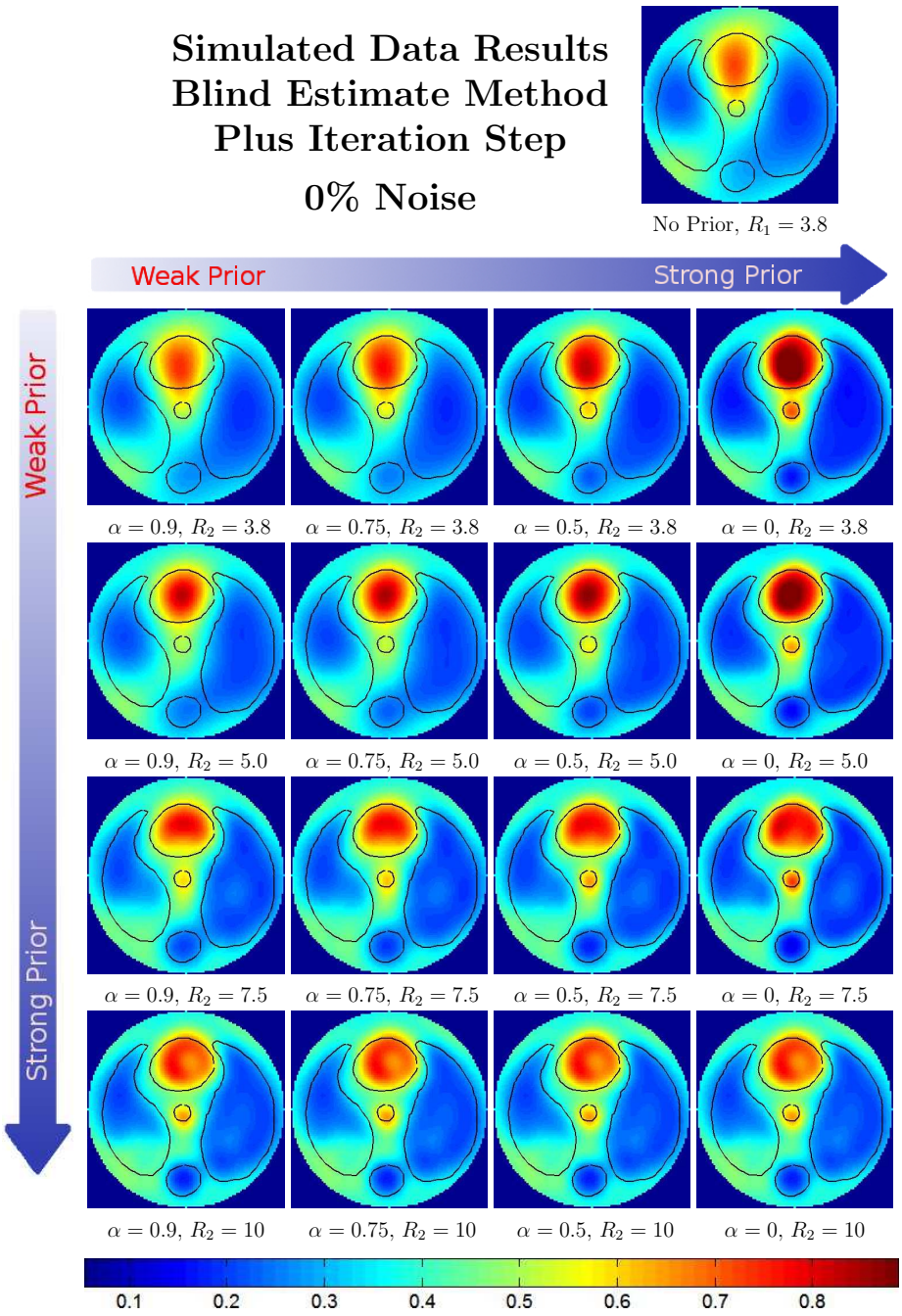

FIGURE 3.8. Reconstructions $\sigma'_{R_2,\alpha}$ for the 0% noise case with simulated data, using the *a priori* scheme with the blind estimate method plus one iteration step, with various values of α and R_2. The reconstruction with no prior is at the top for comparison. The strength of the prior increases moving left to right and top to bottom. The scale bar at the bottom applies to all reconstructions at this noise level.

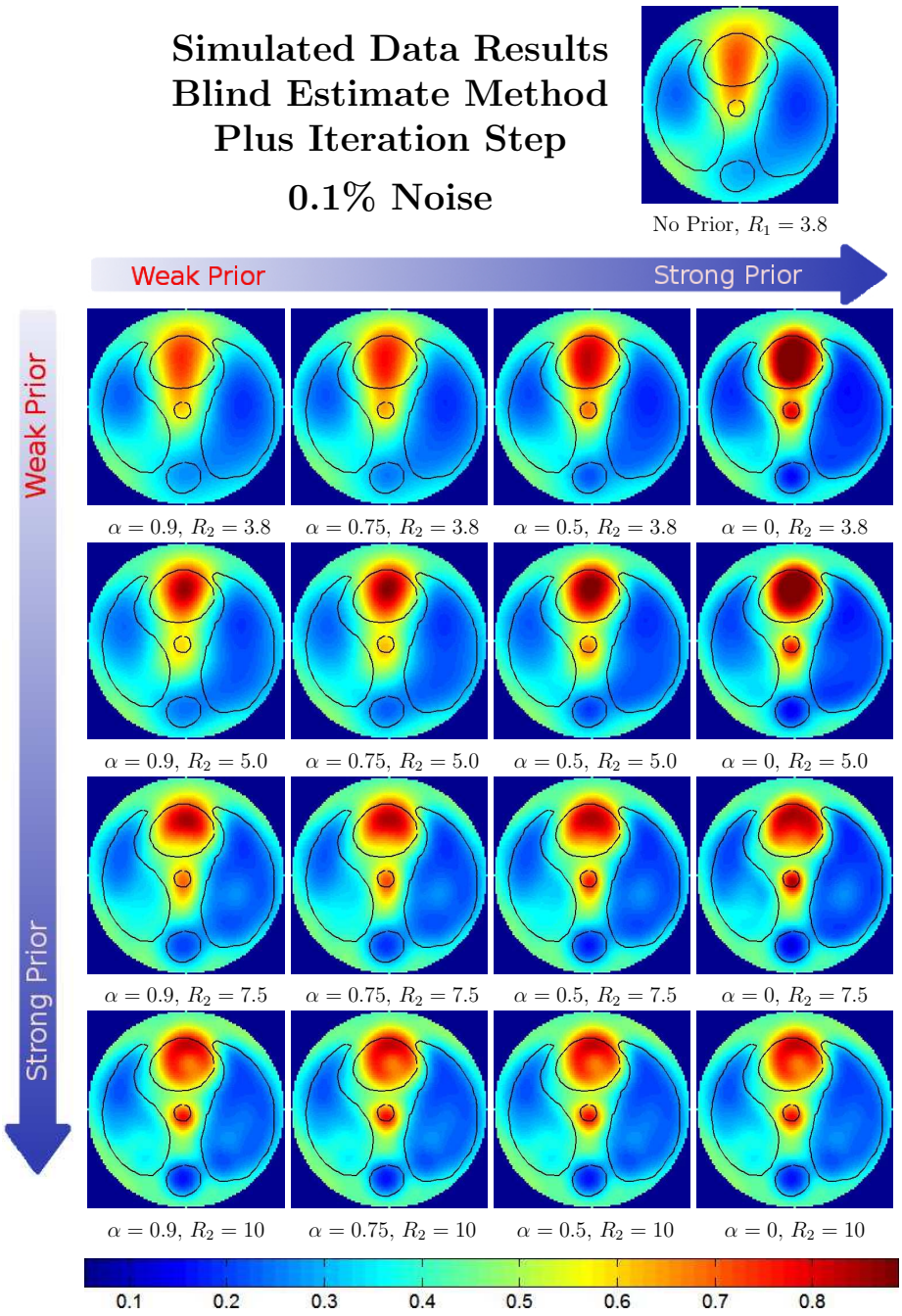

FIGURE 3.9. Reconstructions $\sigma'_{R_2,\alpha}$ for the 0.1% noise case with simulated data, using the *a priori* scheme with the blind estimate method plus one iteration step, with various values of α and R_2. The reconstruction with no prior is at the top for comparison. The strength of the prior increases moving left to right and top to bottom. The scale bar at the bottom applies to all reconstructions at this noise level.

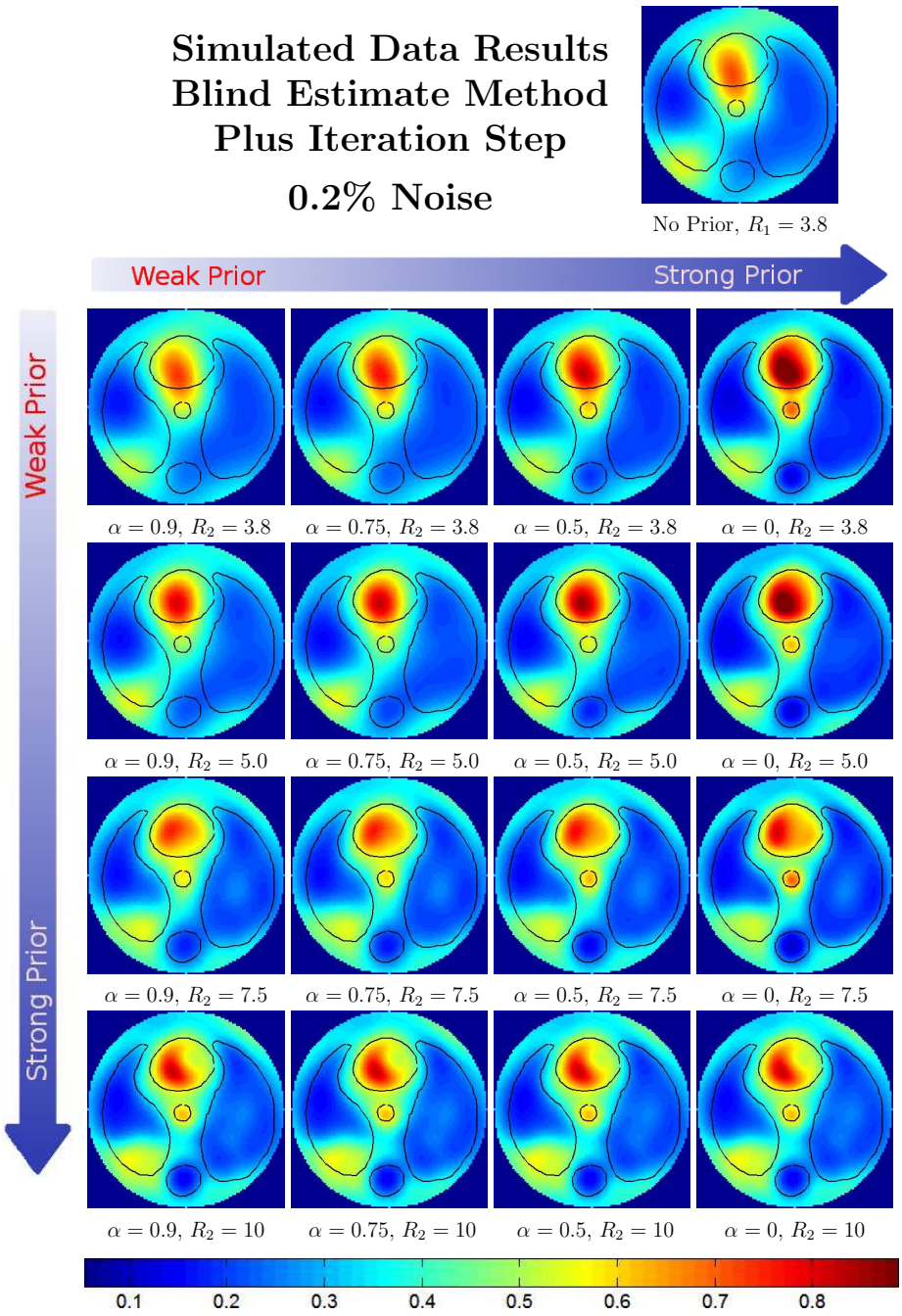

FIGURE 3.10. Reconstructions $\sigma'_{R_2,\alpha}$ for the 0.2% noise case with simulated data, using the *a priori* scheme with the blind estimate method plus one iteration step, with various values of α and R_2. The reconstruction with no prior is at the top for comparison. The strength of the prior increases moving left to right and top to bottom. The scale bar at the bottom applies to all reconstructions at this noise level.

3.5.2. Extraction method applied to simulated data. In assigning approximate conductivity values, for each noise level we first reconstructed σ with $R_1 = 3.8$ using the D-bar method with no *a priori* information. The reconstruction of σ is plotted along with the true organ boundaries in Figure 3.3.

For the extraction of conductivity values, from the σ reconstructions with the superimposed *a priori* organ boundaries, it was clear that the left lung has increased conductivity toward the bottom, so we again divided the lung into top and bottom to construct the prior. For simplicity, we used the same dividing line as was used in §3.5.1, and we selected the same values for c, c_1, and c_2 for all noise cases. Using the methods outlined in §3.4.3, we extracted conductivity values from the reconstruction σ to create σ_{pr}; these assigned values are given in Table 3.2, along with the conductivity values used in the phantom for comparison. We then proceeded with the rest of the *a priori* scheme outlined in §3.2, using $R_1 = 3.8$, and testing various values for R_2 and α. The resulting reconstructions are given in Figures 3.11, 3.12, and 3.13.

In this method, with or without noise, the effusion is clearly visible for all weights of the prior, with improvement in the organ shapes as the weight of the prior increases. Excellent reconstructions are found even in the presence of noise. An iteration step is not included for this method since the first step produces very high quality reconstructions.

Table 3.2. Conductivity values in S/m for the phantom as well as $\tilde{\sigma}_{\text{pr}}$ values computed using extraction method for each of the 3 noise cases.

	Back-ground	Heart	Left Lung top	Left Lung bottom	Right Lung	Aorta	Spine
Used in phantom	0.424	0.750	0.240	0.600	0.240	0.750	0.150
Extracted from σ, 0% noise	0.401	0.681	0.283	0.398	0.251	0.681	0.186
Extracted from σ, 0.1% noise	0.393	0.648	0.292	0.373	0.252	0.648	0.178
Extracted from σ, 0.2% noise	0.423	0.742	0.272	0.460	0.260	0.742	0.177

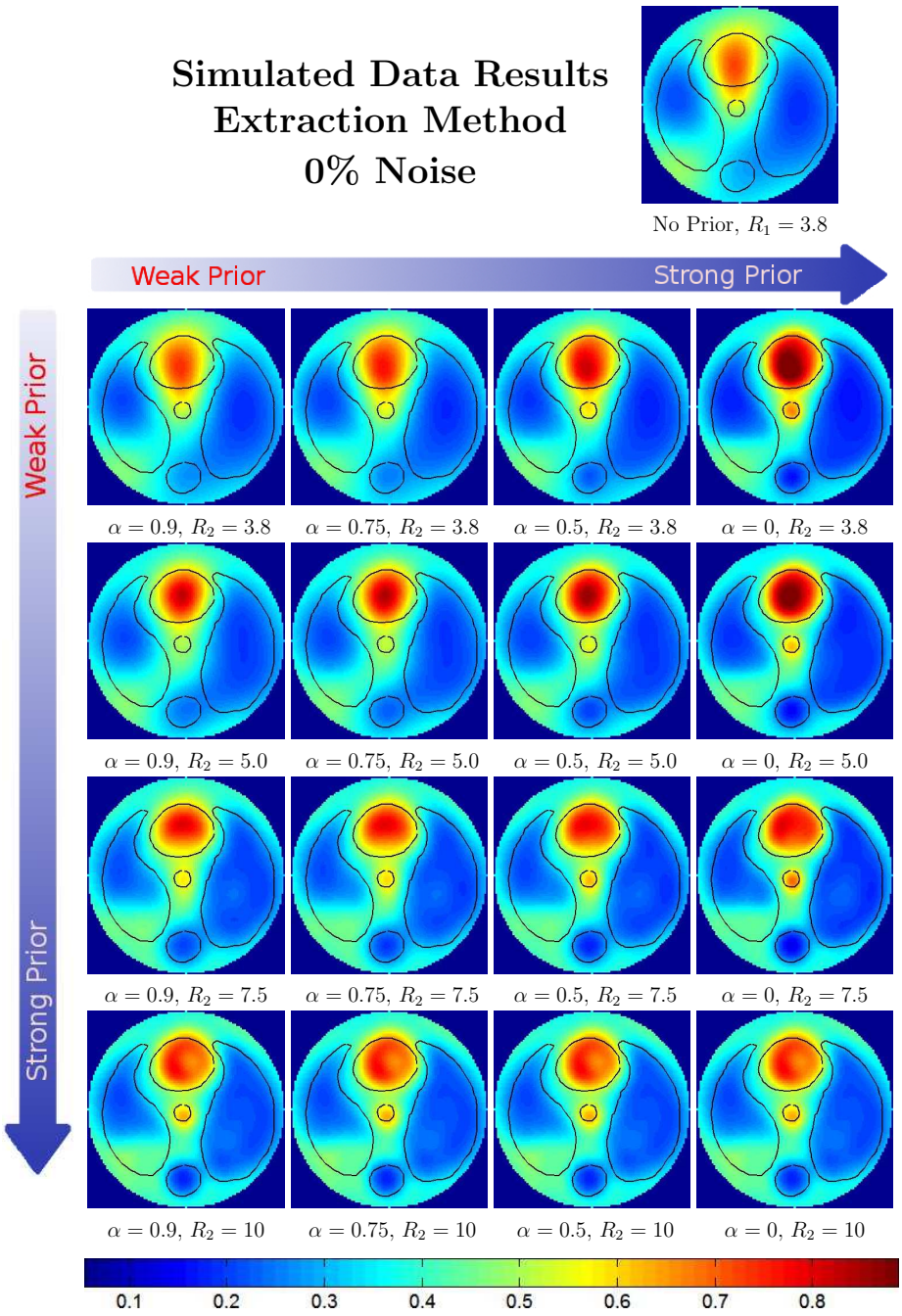

FIGURE 3.11. Reconstructions $\sigma_{R_2,\alpha}$ for the 0% noise case with simulated data, using the *a priori* scheme with the extraction method, with various values of α and R_2. The reconstruction with no prior is at the top for comparison. The strength of the prior increases moving left to right and top to bottom. The scale bar at the bottom applies to all reconstructions at this noise level.

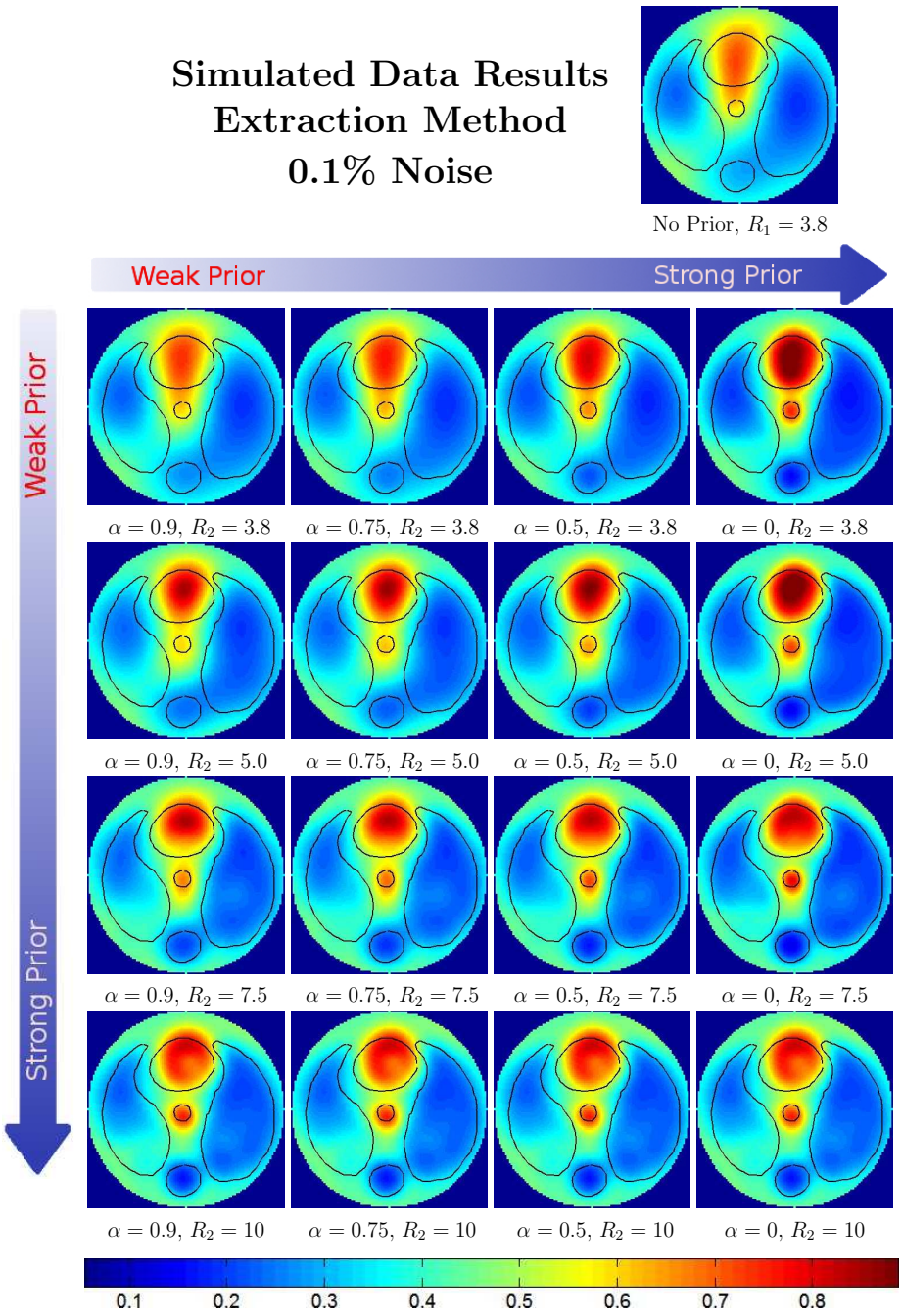

FIGURE 3.12. Reconstructions $\sigma_{R_2,\alpha}$ for the 0.1% noise case with simulated data, using the *a priori* scheme with the extraction method, with various values of α and R_2. The reconstruction with no prior is at the top for comparison. The strength of the prior increases moving left to right and top to bottom. The scale bar at the bottom applies to all reconstructions at this noise level.

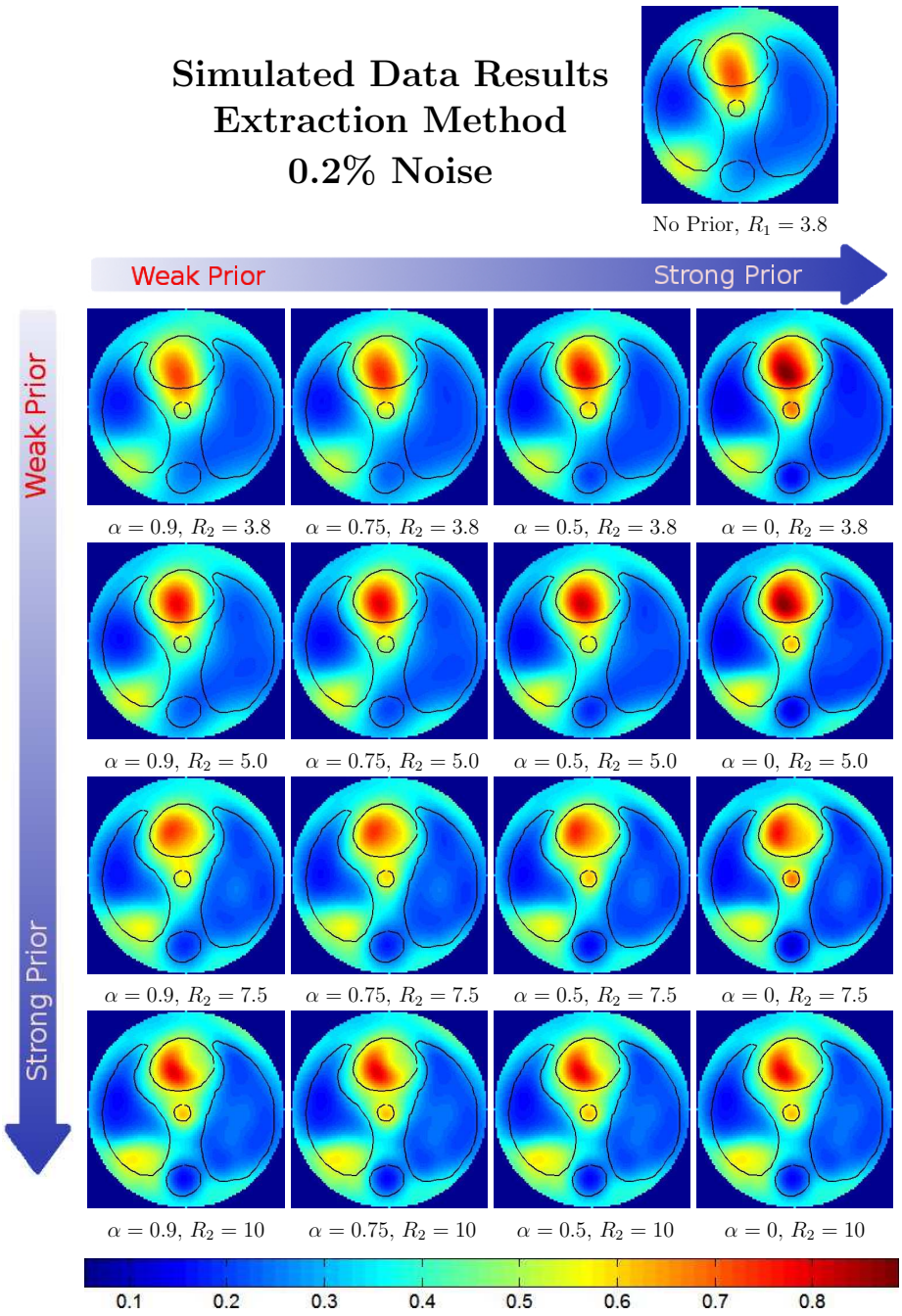

FIGURE 3.13. Reconstructions $\sigma_{R_2,\alpha}$ for the 0.2% noise case with simulated data, using the *a priori* scheme with the extraction method, with various values of α and R_2. The reconstruction with no prior is at the top for comparison. The strength of the prior increases moving left to right and top to bottom. The scale bar at the bottom applies to all reconstructions at this noise level.

3.6. A DISCUSSION OF THE "EDGE-RINGING" EFFECT

The "edge-ringing" effect seen in the reconstructed spine and lungs for small α or large R_2 in the reconstructions from simulated data (see Figure 3.6, especially) is likely due in part to the influence of the term μ_{int} on the reconstruction (in the case of small α) and the effects of the high-frequency scattering data from the prior (in the case of large R_2). The μ_{int} term provides excellent spatial resolution of the prior, detecting edges extremely well, but introducing ringing since it becomes increasingly uniform, tending to 1 as $R_2 \to \infty$. This effect can be seen in Figure 3.14.

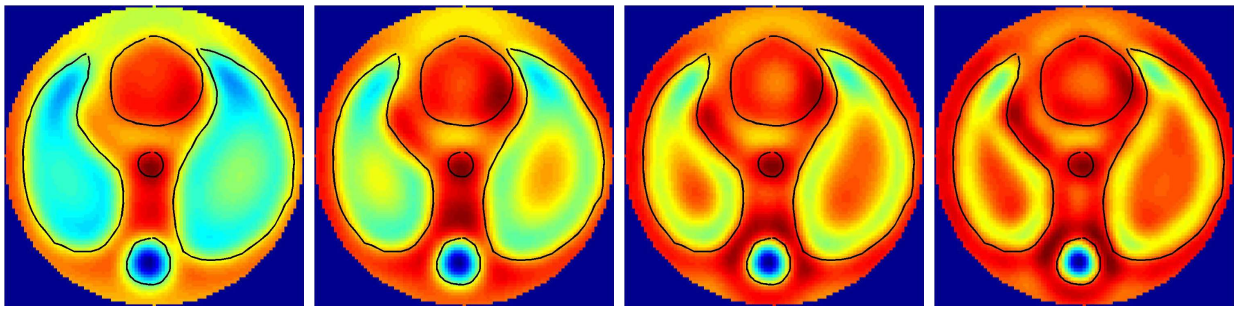

(A) $R_2 = 3.8$ (B) $R_2 = 5.0$ (C) $R_2 = 7.5$ (D) $R_2 = 10$

FIGURE 3.14. Plots of the real part of μ_{int} used in the simulations with various truncation radii R_2. Since $\mu_{\text{int}} \to 1$ as $R_2 \to \infty$, the scale must be adjusted for each value of R_2 for best viewing results. The boundaries shown are those used to compute σ_{pr}.

As was pointed out in [80], the high-frequency values of the scattering transform encode the sharper features of EIT images. In particular, the high-gradient areas of a conductivity distribution correspond to high scattering frequencies. In D-bar reconstructions regularized by low-pass filtering as described [108], the high-frequency scattering values are set to zero, which results in a smoothing or blurring effect. This is analogous to noise reduction via linear frequency filtering (with a standard Fourier transform) of digital images or signals. In our method, we include higher scattering frequencies from the prior using the piecewise

scattering transform (49). When R_2 is large, these values tend to dominate in the reconstruction, probably due to the high quality of the *a priori* scattering data as compared to data produced via simulation. To illustrate this effect, consider the reconstruction shown in Figure 3.15, which was produced using the following scattering transform, in which low scattering frequencies are set to zero, and only frequencies $3 < |k| \leq 10$ are preserved:

$$\mathbf{t}_{\mathrm{hf}}(k) = \begin{cases} 0, & |k| \leq 3 \\ \mathbf{t}_{\mathrm{pr}}(k), & 3 < |k| \leq 10 \\ 0, & |k| > 10 \end{cases} \cdot \tag{65}$$

Furthermore, the reconstruction shown in Figure 3.15 was produced using weighting parameter $\alpha = 1$, leading to complete suppression of the μ_{int} term. The result demonstrates that high scattering frequencies encode mostly information corresponding to the edges of organ boundaries. This experiment is analogous to high-pass frequency filtering of digital images, which results in detection of high-gradient areas in the digital image corresponding to edges.

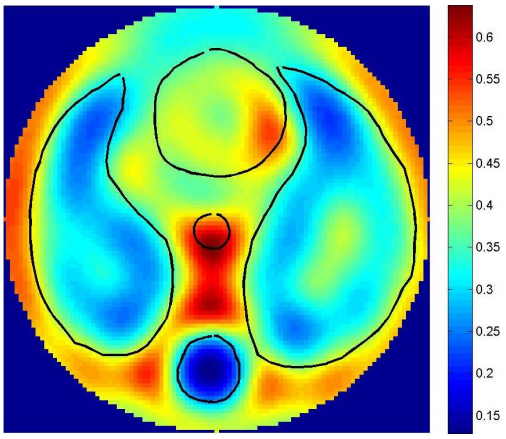

FIGURE 3.15. Reconstruction produced using the scattering transform (65) and $\alpha = 1$, leading to complete suppression of the μ_{int} term. Low frequency scattering values were set to zero, and only frequencies $3 < |k| \leq 10$ are used. The result suggests that high scattering frequencies encode mostly information corresponding to the edges of organ boundaries.

3.7. RESULTS FROM EXPERIMENTAL TANK DATA

In this section, we apply the *a priori* methods to experimental tank data, with EIT measurements taken using the ACE1 EIT system at CSU. We describe three separate experiments designed to simulate human thoracic data.

In all three experiments, the lab set-up consisted of a circular PVC tank of inner diameter 303.215 mm, surrounded by 32 equally-spaced stainless steel electrodes, each 25.4 mm in width. In the first experiment agar shapes representing a healthy human heart and lungs were placed into the tank, and the tank was filled with saline solution up to the top of the agar targets, resulting in a saline depth of 1 cm. This experimental set-up is shown on the left in Figure 3.16. We measured the conductivities of the saline and the agar components using a conductivity meter; the resulting measured conductivity values are shown in Table 3.3. We then applied electrical current at skip 0, frequency 125 kHz, current amplitude approximately 3.3 mA, and recorded the resulting EIT data.

FIGURE 3.16. Left: experimental set-up with agar heart and lungs in a PVC tank, surrounded by saline solution. Middle: a second experiment, in which the heart and lungs are preserved, but a copper conductor has been inserted into the bottom of the right lung. Left: a third experiment, in which the conductor has been removed, and a plastic insulator has been inserted in its place.

In a second experiment, we left the agar targets in the tank, and a circular copper conductor of diameter 24 mm was inserted into the bottom of the right lung (using the

TABLE 3.3. Measured conductivity values (in S/m) for agar components and background saline solution used in the described tank experiments. Conductivity values were measured using a conductivity meter at the start of the experiment.

Component	Measured Conductivity (S/m)
Background Saline	0.185
Heart	0.238
Lungs (right and left)	0.136

convention that the right lung is on the right-hand side of the image). EIT measurements were repeated at skip 0, frequency 125 kHz, current amplitude approximately 3.3 mA. This conductor could represent the presence of conductive pathology such as a cancerous tumor, contusion, or a blood clot in the lung. This experimental set-up is depicted in the middle in Figure 3.16.

In a third experiment, the conductor was removed, and a circular plastic insulator of diameter 28 mm was inserted in its place. While this scenario is not necessarily representative of a real-world physical pathology, we felt this was a natural experiment to try, and the resulting data provides a nice contrast with the case of the conductive pathology. EIT measurements were once more repeated at skip 0, frequency 125 kHz, current amplitude approximately 3.3 mA. This experimental set-up is depicted on the right in Figure 3.16.

Finally, the agar targets were removed, and additional saline was added to the tank to preserve the water level of 1 cm. EIT measurements were taken on the homogeneous tank, and this data were used in place of the measurements corresponding to Λ_1 in the reconstruction algorithm. This method (which is a form of difference imaging) results in a loss of the true conductivity values in the reconstructions.

The D-bar reconstructions σ for these two experimental test cases, using the method of §1.3, are shown in Figure 3.17. Reconstructions in this section, including the reconstructions σ and the results of the *a priori* schemes, were again computed using a z-mesh with 101×101

elements and inner truncation radius $R_1 = 3.8$. We show test results for parameter values $\alpha \in \{0, 0.5, 0.75, 0.9\}$, $R_2 \in \{3.8, 4.5, 5.0, 7.5\}$.

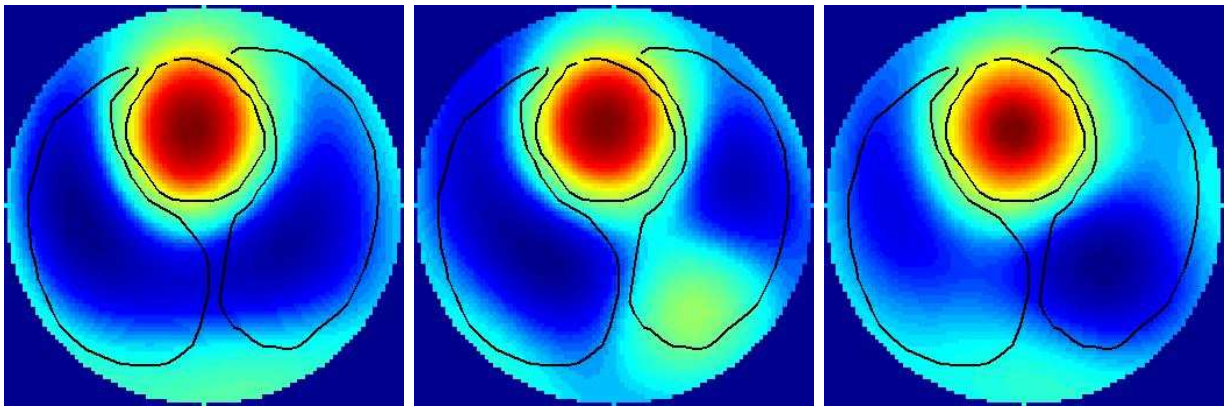

FIGURE 3.17. Plots of the reconstructions σ from the tank experiments, computed using the regularized D-bar method of §1.3 (see also lines 5–15 of Algorithm 4) with truncation radius $R_1 = 3.8$, with superimposed organ boundaries approximated from photographs. Each reconstruction is plotted on its own scale.

In the remainder of this section, we describe the methodology used to apply the *a priori* methods to these two experimental test cases, and we discuss the results and insights gained from these experiments.

3.7.1. TANK EXPERIMENT: HEALTHY HUMAN HEART AND LUNGS. In our tank experiments, boundaries used to construct $\tilde{\sigma}_{\text{pr}}$ were formed by clicking around the organ boundaries in the photograph of the experimental setup, saving this geometric data, and then scaling to the proper dimensions. The photograph of the experimental setup and the extracted organ boundaries are shown in Figure 3.18. Due to the previously mentioned loss of true conductivity values in the reconstructions, the extraction method (at least in its unmodified form) would not be useful to obtain conductivity estimates for the prior. Instead, we used the blind estimate method, with conductivity values selected based on the measurements shown in Table 3.3, so that $\sigma_{\text{heart}} = 0.238$ S/m, $\sigma_{\text{r lung}} = \sigma_{\text{l lung}} = 0.136$ S/m, and $\sigma_{\text{bg}} = 0.185$ S/m.

Due to noise and physical limitations of the measuring process, these values are themselves approximations of the true conductivity values, so this is representative of clinical situation in which we use published values for the conductivities of various human tissues.

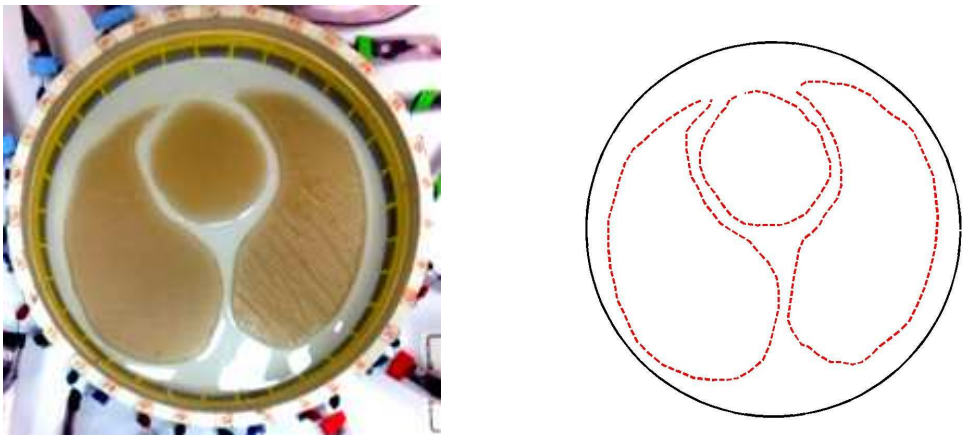

FIGURE 3.18. Left: experimental set-up with agar heart and lungs in tank. Right: polygonal approximations of organ boundaries used as geometric *a priori* information in our experiments with tank data.

Reconstructions $\sigma_{R_2,\alpha}$ for this tank experiment with a healthy heart and lungs phantom are shown in Figure 3.21. Due to loss of true conductivity values, for optimum plotting results the reconstructions were individually scaled to the interval $[0, 1]$. Observe the pronounced edge-ringing effect present for larger R_2 values. For the reconstructions displayed here, we selected slightly different values for R_2 than those used in the experiments with simulated data. This selection was made due to the apparent increased sensitivity to the prior and to the increased edge-ringing effect. For smaller values of R_2, however, the spatial resolution, organ shapes, and overall image quality is excellent.

3.7.2. TANK EXPERIMENT: CONDUCTIVE PATHOLOGY. For our experiment with the added conductive pathology, we ran initial reconstructions using the same prior σ_{pr} as was used in the case with the healthy heart and lungs. This represents a situation where a pathology has developed that was not present at the time of the original CT scan, and we

use the unmodified CT scan data to construct the prior. The results of this experiment are shown in Figure 3.22. As one can see, when the prior is fairly weak, the pathology in the right lung is still evident. But for larger R_2 and smaller α, the pathology becomes less obvious as the influence of the healthy prior increases. Compared to the reconstructions of the healthy phantom in Figure 3.21, however, the pathology leaves traces on all the reconstructions even when the influence of the prior is very strong.

Due to the very obvious, roughly circular area of high-conductivity present in the right lung in the reconstruction σ, which can best be seen in the contour plot of σ depicted in Figure 3.19, we then modified the prior to reflect this obvious pathology. This represents a situation where, although a pathology has appeared since the CT scan was taken, the initial EIT scan indicates a possible pathology, and we are able to modify the prior accordingly. Since the pathology appears as a fairly round, globular high-conductivity region in the EIT reconstruction σ_{pr}, we used level sets combined with visual intuition to extract a simply-connected high-conductivity region, and then took the convex hull of this region as the polygonal boundary for the pathology. This procedure resulted in the prior depicted in Figure 3.19. Observe that the spatial location of the pathology is close to, but does not coincide perfectly with, the actual location of the copper conductor in the photograph.

The conductor in the experiment was made out of copper, and so has extremely high conductivity. However, in the reconstruction σ, the conductivity of the pathology appears to be less than that of the heart, probably due to the surrounding resistive lung phantom. Since in practice the conductivity of the pathology would be unknown, we therefore based the approximate conductivity value for the prior on the reconstruction σ. To obtain the value σ_{path} to use in region corresponding to the pathology in the prior, we used the following computation, which may be thought of as the extraction method modified for use with

difference images. Again denote by $\{z_s'\}$ the finite set of points in the z-mesh used to construct σ. Denote by P_{path} the closed polygonal region defined by the extracted boundary for the pathology, let $\tilde{P}_{\text{path}} := \{z_s'\} \cap P_{\text{path}}$, and compute the average value

$$\sigma_{\text{path}*} := \frac{1}{M} \sum_{m=1}^{M} \sigma(z_m'), \quad z_m' \in \tilde{P}_{\text{path}},$$

where M denotes the number of points z_m' in $\tilde{P}_{\text{path}}$. Then compute the value σ_{path} to use in $\tilde{\sigma}_{\text{pr}}$ by the following scaling procedure:

$$\sigma_{\text{path}} = \sigma_{\text{min pr}} + \frac{\sigma_{\text{path}*} - \sigma_{\text{min}}}{\sigma_{\text{max}} - \sigma_{\text{min}}} (\sigma_{\text{max pr}} - \sigma_{\text{min pr}}),$$

where σ_{min}, σ_{max} are as in (64), and $\sigma_{\text{min pr}} = \sigma_{\text{r lung}}$, $\sigma_{\text{max pr}} = \sigma_{\text{heart}}$ are the min and max values used in the healthy prior, which may be thought of as approximations for the min and max values in the true conductivity distribution. Furthermore, assign the value $\sigma_{\text{r lung}}$ to the region $P_{\text{r lung}} - P_{\text{path}}$.

For our test case with the copper conductor, the preceding computation resulted in $\sigma_{\text{path}} = 0.181$ S/m. The results of the *a priori* procedure with this modified prior are shown in Figure 3.23. Observe that although the pathology is quite small (both in the prior and in reality), its presence is apparent in all of the reconstructions, at least until the "edge ringing" effect begins to dominate for larger values of R_2.

3.7.3. Tank experiment: resistive pathology. For our experiment with the added resistive pathology, we again ran initial reconstructions using the same prior σ_{pr} as was used in the case with the healthy heart and lungs. The results of this experiment are shown in Figure 3.24. Once again, when the prior is fairly weak, the pathology in the right lung is

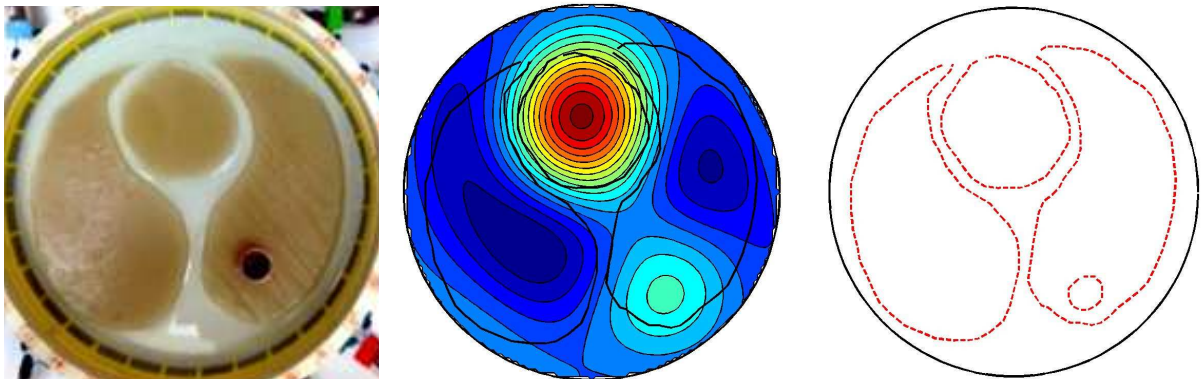

FIGURE 3.19. Right: the experimental set-up with agar heart and lungs and an added copper conductor representing a lung pathology. Middle: a contour plot, showing level sets, of the EIT reconstruction σ computed with no prior. Left: the modified organ boundaries for the prior reflecting the pathology, where the boundary for the pathology was computed by taking a level set of the reconstruction σ.

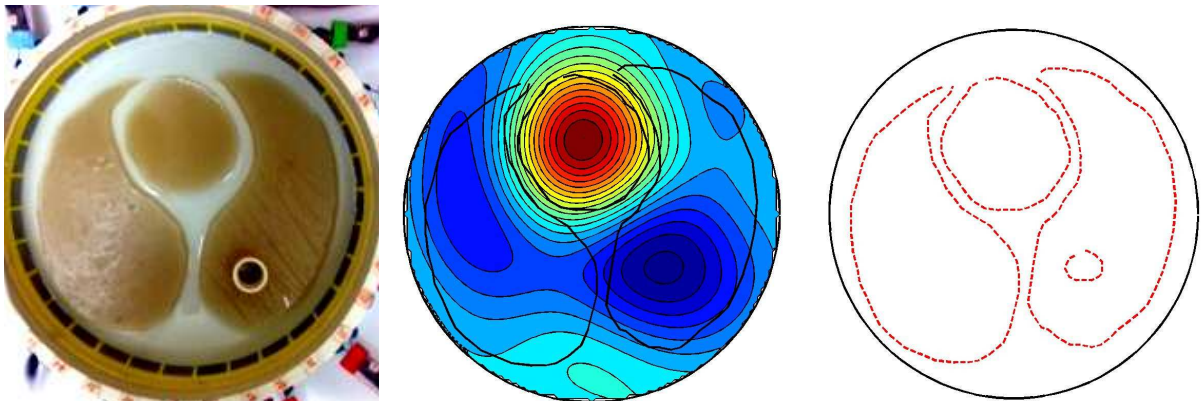

FIGURE 3.20. Right: the experimental set-up with agar heart and lungs and an added plastic insulator representing a lung pathology. Middle: a contour plot, showing level sets, of the EIT reconstruction σ computed with no prior. Left: the modified organ boundaries for the prior reflecting the pathology, where the boundary for the pathology was computed by taking a level set of the reconstruction σ.

still evident, but its presence in the reconstructions becomes less obvious as the influence of the prior increases.

We then modified the prior to reflect the pathology, once again using level sets, in a method analogous to that used for the conductive pathology. This procedure resulted in the prior depicted in Figure 3.20. To obtain the value σ_{path} to use in the region corresponding

to the resistive pathology in the prior, we used the following computation, which is slightly different than the method used to compute the value for the conductive pathology, due to the fact that the insulator shows up as more resistive than the lungs in the initial reconstruction σ. Denote again by P_{path} the closed polygonal region defined by the extracted boundary for the pathology, let $\tilde{P}_{\text{path}} := \{z'_s\} \cap P_{\text{path}}$ and again compute the average value

$$\sigma_{\text{path}*} := \frac{1}{M} \sum_{m=1}^{M} \sigma(z'_m), \quad z'_m \in \tilde{P}_{\text{path}},$$

where M denotes the number of points z'_m in $\tilde{P}_{\text{path}}$. Furthermore, compute the average value of the reconstruction in the left lung:

$$\sigma_{\text{l lung}*} := \frac{1}{M} \sum_{m=1}^{M} \sigma(z'_m), \quad z'_m \in \tilde{P}_{\text{l lung}},$$

where M denotes the number of points z'_m in $\tilde{P}_{\text{l lung}}$. Then compute the value σ_{path} to use in $\tilde{\sigma}_{\text{pr}}$ by the following scaling procedure:

$$\sigma_{\text{path}} = \sigma_{\text{min pr}} - \frac{\sigma_{\text{l lung}*} - \sigma_{\text{min}}}{\sigma_{\text{max}} - \sigma_{\text{ l lung}*}} (\sigma_{\text{max pr}} - \sigma_{\text{min pr}}),$$

where once again σ_{min}, σ_{max} are as in (64), and $\sigma_{\text{min pr}} = \sigma_{\text{r lung}}$, $\sigma_{\text{max pr}} = \sigma_{\text{heart}}$ are the min and max values used in the healthy prior. Finally, assign the value $\sigma_{\text{r lung}}$ to the region $P_{\text{r lung}} - P_{\text{path}}$.

For our test case with the plastic insulator, the preceding computation resulted in $\sigma_{\text{path}} = 0.104$ S/m. The results of the *a priori* procedure with this modified prior are shown in Figure 3.25. Once again, the resistive pathology is now evident in all the reconstructions, at least until the "edge-ringing" effect dominates for large R_2.

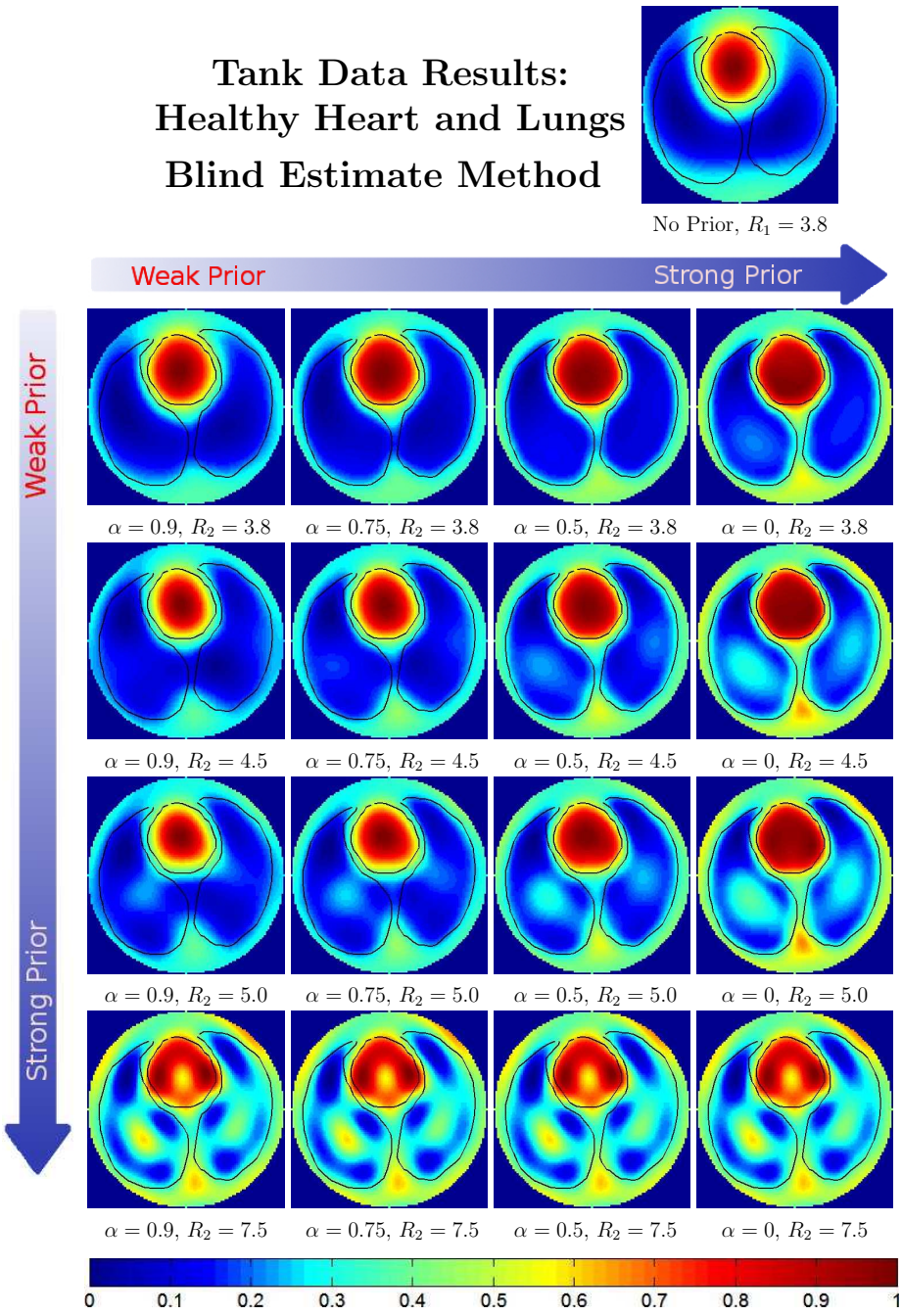

FIGURE 3.21. Reconstructions $\sigma_{R_2,\alpha}$ for the experimental tank data representing healthy heart and lungs, using the *a priori* scheme with the blind estimate method, with various values of α and R_2. The reconstruction with no prior is at the top for comparison. The strength of the prior increases moving left to right and top to bottom. Due to loss of true conductivity values, the reconstructions were individually scaled to the interval $[0, 1]$.

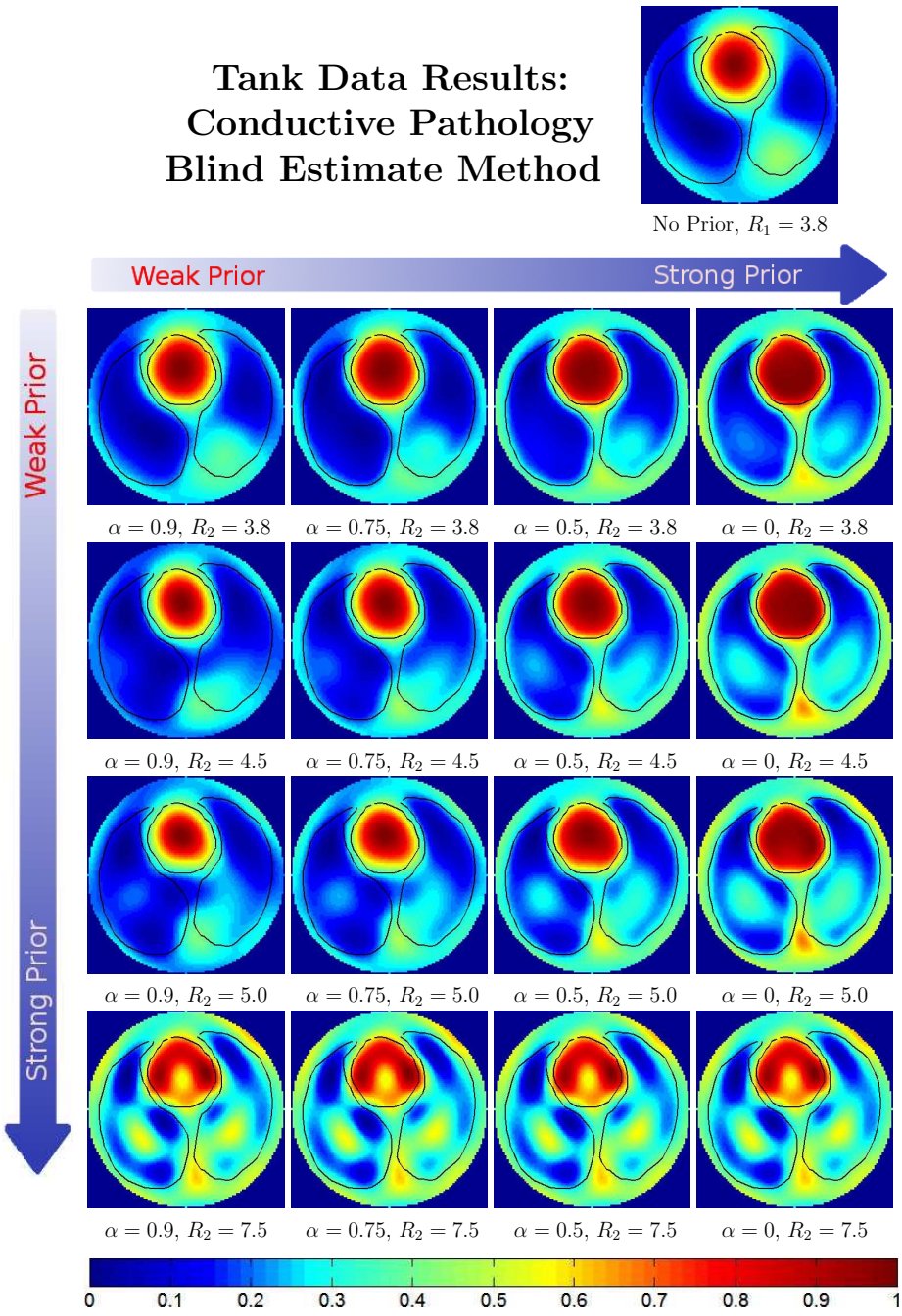

FIGURE 3.22. Reconstructions $\sigma_{R_2,\alpha}$ for the experimental tank data with added conductive pathology, using the *a priori* scheme with the blind estimate method, with various values of α and R_2. The reconstruction with no prior is at the top for comparison. The strength of the prior increases moving left to right and top to bottom. Due to loss of true conductivity values, the reconstructions were individually scaled to the interval $[0, 1]$.

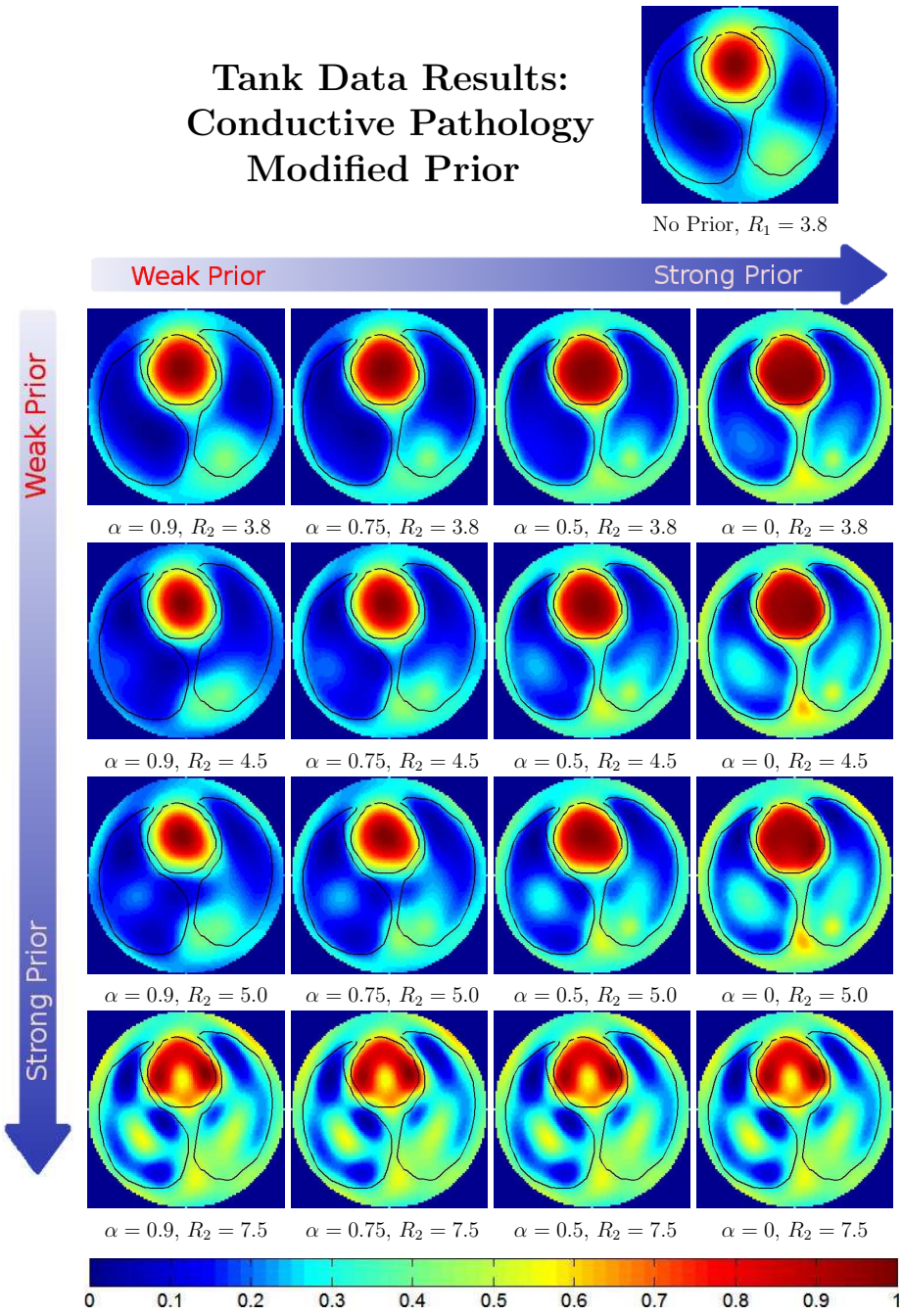

FIGURE 3.23. Reconstructions $\sigma_{R_2,\alpha}$ for the experimental tank data with added conductive pathology, using the *a priori* scheme with modified prior, with various values of α and R_2. The reconstruction with no prior is at the top for comparison. The strength of the prior increases moving left to right and top to bottom. Due to loss of true conductivity values, the reconstructions were individually scaled to the interval $[0, 1]$.

3.8. DISCUSSION OF DISCONTINUITIES IN THE PIECEWISE SCATTERING DATA

One question that is worth asking is the following: what does the scattering transform $\mathbf{t}_{R_1,R_2}(k)$ given in (49) look like for k close to $|k| = R_1$? Specifically, in the case of practical data, are there large discontinuities in the scattering data at the boundary R_1 due to large discrepancies between $\mathbf{t}$ and $\mathbf{t}_{\text{pr}}$?

We have found that in the cases we have examined, the scattering transform $\mathbf{t}$ tends to be of similar magnitude as $\mathbf{t}_{\text{pr}}$, and the match-up of the scattering data is reasonably good. To demonstrate this, consider the plots of the piecewise scattering transform $\mathbf{t}_{R_1,R_2}(k)$, computed on a 64×64 k-grid with $R_1 = 3.8, R_2 = 10$, for both the simulated data 0% noise case with the prior constructed using the blind estimate method (Figure 3.26); and the tank data case of the healthy heart and lungs phantom (Figure 3.27). As one can see, there are some discontinuities in both the real and imaginary parts of the scattering transforms, but overall the scattering data for $|k| \leq 3.8$ is of similar magnitude as the scattering data for $3.8 < |k| \leq 10$. A poorly-constructed prior (that is not a good match for the true conductivity distribution) will result in greater mismatch of scattering data, and this likely leads to artifacts in the resulting reconstructions. However, this phenomenon requires further study.

3.9. CONCLUSIONS FROM THE A PRIORI METHOD

We have demonstrated the effectiveness of the *a priori* algorithm described in this chapter using both numerically simulated data with added noise as well as experimental tank data collected using the ACE1 EIT system at CSU. These experiments indicate that the method produces images with enhanced spatial resolution and improved organ shapes in both these scenarios, even in the presence of noise.

Based on the results presented here, it is recommended that the reconstructions be monitored for the"edge-ringing" effect, and this effect can be mitigated by decreasing the value of R_2. The appropriate choices for the parameters R_2 and α may vary depending on the application, and it is recommended that several values be tested to observe their effects on the reconstructions. Overall, the method shows promise for clinical use in lung imaging when *a priori* information about organ boundaries can be obtained from a CT or MRI scan, for example. Future work is needed to evaluate its clinical effectiveness.

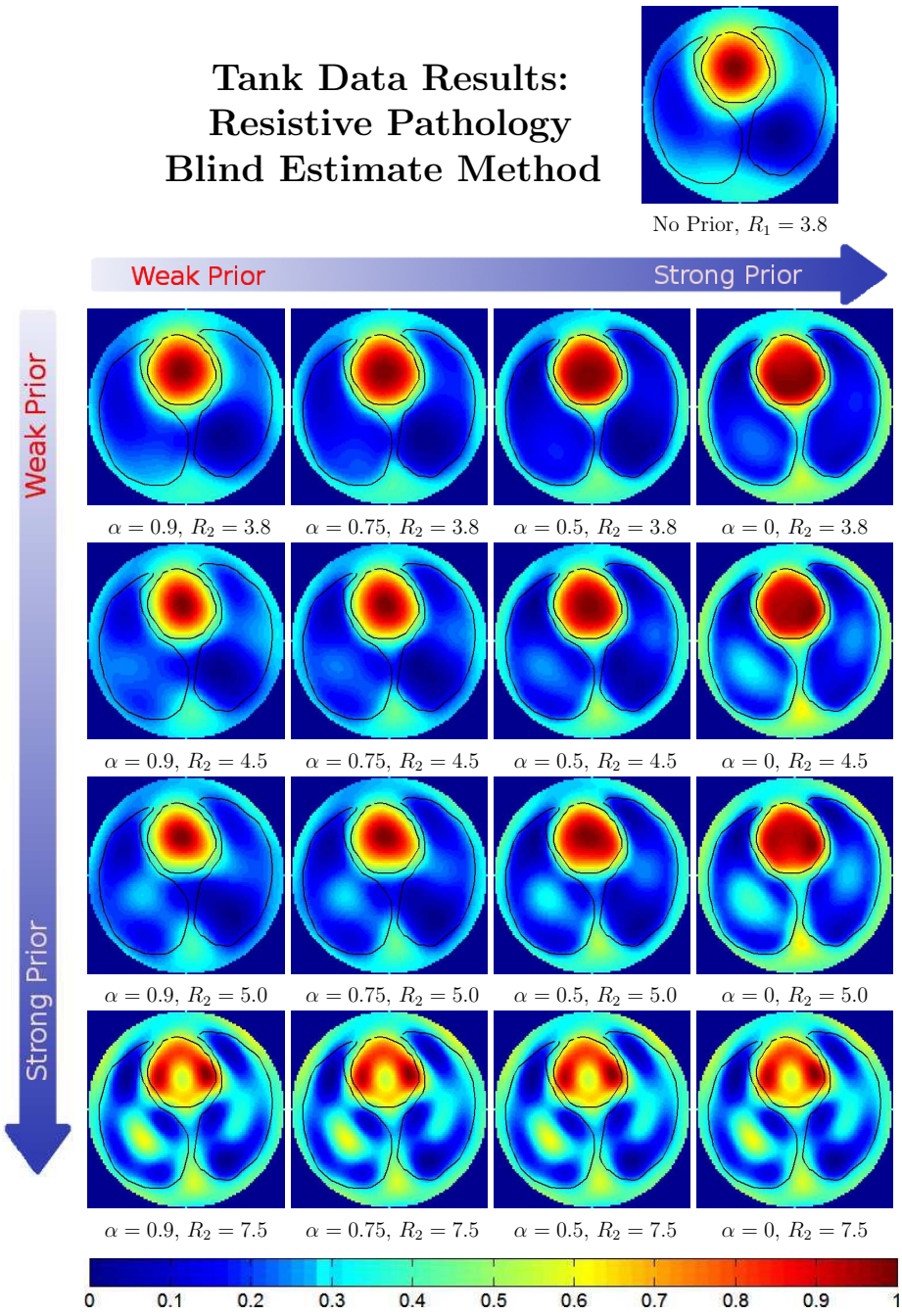

FIGURE 3.24. Reconstructions $\sigma_{R_2,\alpha}$ for the experimental tank data with added resistive pathology, using the *a priori* scheme with the blind estimate method, with various values of α and R_2. The reconstruction with no prior is at the top for comparison. The strength of the prior increases moving left to right and top to bottom. Due to loss of true conductivity values, the reconstructions were individually scaled to the interval $[0, 1]$.

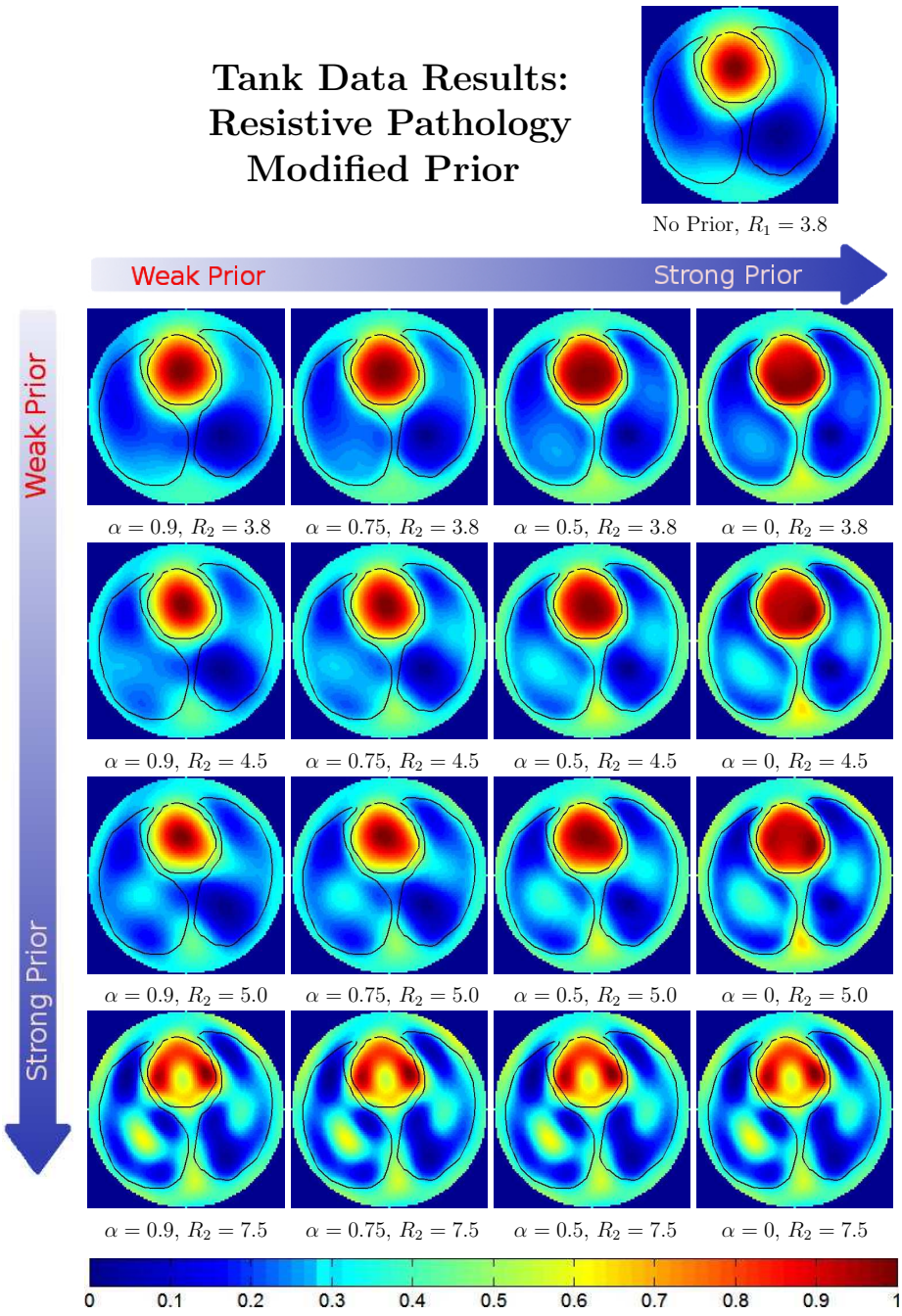

FIGURE 3.25. Reconstructions $\sigma_{R_2,\alpha}$ for the experimental tank data with added resistive pathology, using the *a priori* scheme with modified prior, with various values of α and R_2. The reconstruction with no prior is at the top for comparison. The strength of the prior increases moving left to right and top to bottom. Due to loss of true conductivity values, the reconstructions were individually scaled to the interval $[0, 1]$.

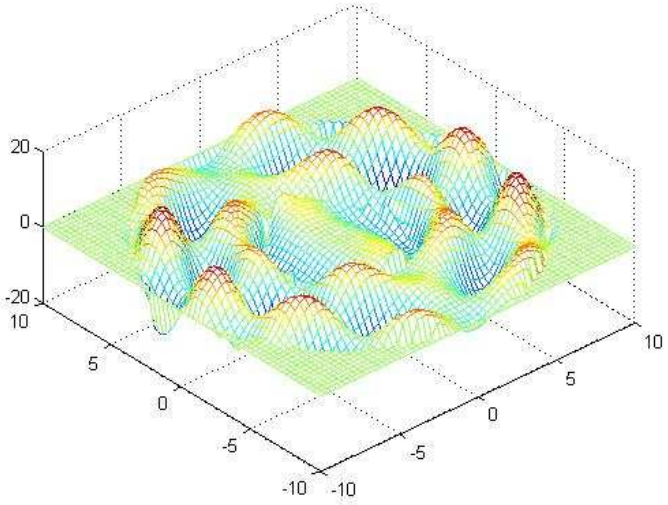

(A) Real part of $\mathbf{t}_{R_1,R_2}(k)$

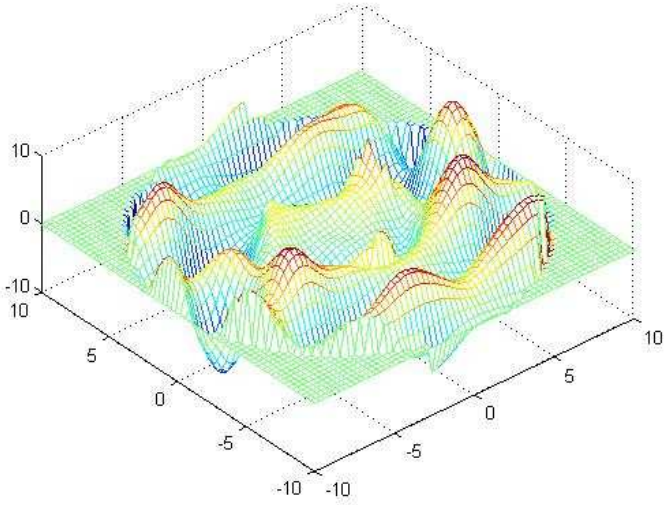

(B) Imaginary part of $\mathbf{t}_{R_1,R_2}(k)$

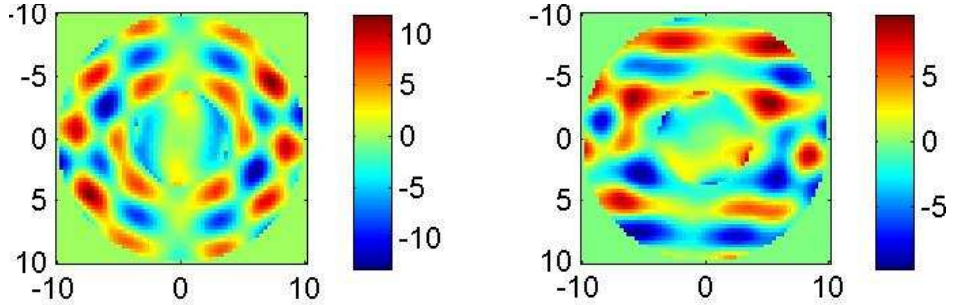

(C) Real (left) and imaginary (right) parts of $\mathbf{t}_{R_1,R_2}(k)$

FIGURE 3.26. Real and imaginary parts of the piecewise scattering transform $\mathbf{t}_{R_1,R_2}(k)$, computed on a 64×64 k-grid with $R_1 = 3.8, R_2 = 10$, for the simulated data 0% noise case, with the prior constructed using the blind estimate method.

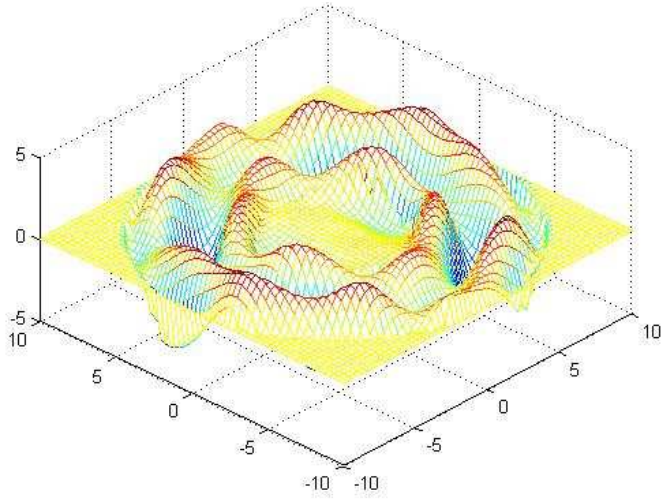

(A) Real part of $\mathbf{t}_{R_1,R_2}(k)$

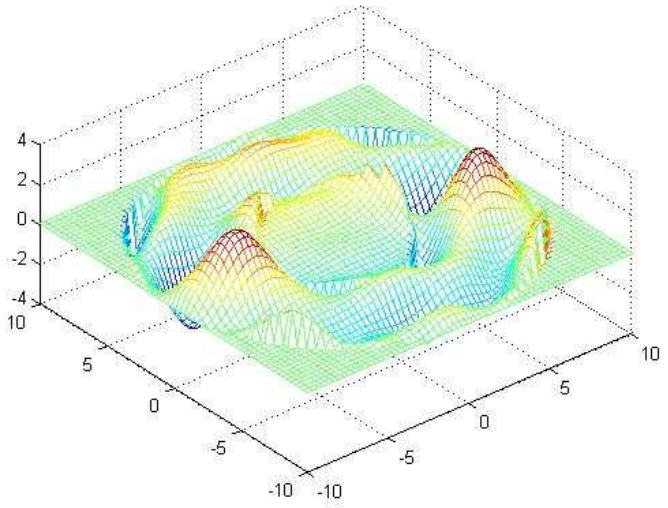

(B) Imaginary part of $\mathbf{t}_{R_1,R_2}(k)$

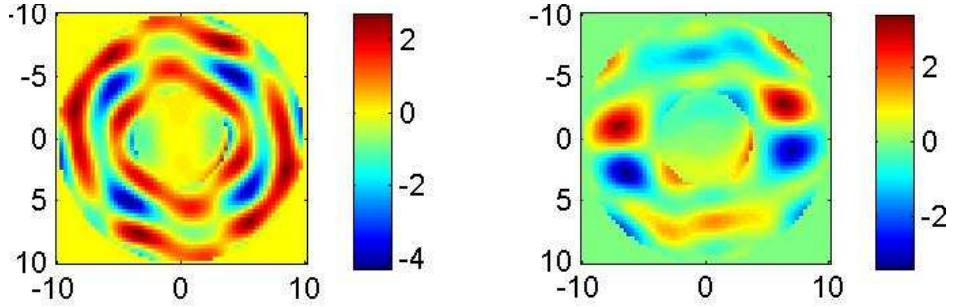

(C) Real (left) and imaginary (right) parts of $\mathbf{t}_{R_1,R_2}(k)$

FIGURE 3.27. Real and imaginary parts of the piecewise scattering transform $\mathbf{t}_{R_1,R_2}(k)$, computed on a 64×64 k-grid with $R_1 = 3.8, R_2 = 10$, for the case of experimental tank data with the healthy heart and lungs phantom.

CHAPTER 4

CONCLUSIONS

In this dissertation, we have described two successful computational improvements to the 2-D D-bar method of A. Nachman for electrical impedance imaging of conductivities. While these contributions have been developed mainly for use in medical imaging applications, and specifically human thoracic imaging, we believe the methods described here could be modified and developed for other applications of EIT, including other medical applications and possibly industrial and engineering applications as well.

The real-time D-bar algorithm described in Chapter 2 effectively shows that CGO methods can be made to be computationally efficient—and can in fact be made to run in real-time—thus demonstrating their feasibility for their use in functional bedside EIT imaging. This could prove to be greatly beneficial in clinical settings where functional real-time information is necessary, such as in ventilation monitoring and other bedside monitoring scenarios. The methods described here could also potentially be modified for use in applications other than medical imaging, such as process monitoring. We described two different ways to parallelize the 2-D D-bar algorithm, and we compared and contrasted the merits of each. Future work in this area could include the implementation of the algorithm in other programming languages such as C or FORTRAN, possibly combined with GPU parallelization, which may improve computational efficiency. Algorithm efficiency for absolute images (as opposed to difference images, which were presented in this dissertation) could also be examined. At the time of the writing of this writing, the work on the real-time D-bar algorithm described here has resulted in one manuscript published in a peer-reviewed journal [9]. This work was also presented in the 15th Annual Conference on Biomedical Applications of Electrical

Impedance Tomography, [8], where the author received the 2nd-place award for best student paper.

The *a priori* D-bar methods described in Chapter 3 demonstrate that spatial resolution in EIT imaging may be improved by incorporating prior information regarding spatial geometry, or a combination of geometry and estimated conductivity values, into the D-bar method. The *a priori* information was incorporated in two distinct ways: (1) we added an annulus containing high-frequency *a priori* scattering data to the nonlinear Fourier transform involved in the D-bar method, effectively stabilizing the method and allowing the expression of edges and other sharp details in the reconstructions, and (2) we incorporated a weighted integral term containing *a priori* CGO data into the D-bar equation, which resulted in different but similar effects. For each method, we provide a means to control the influence of the prior on the resulting reconstruction. We further described possible iterative methods that may produce improved results. These methods can be used separately or in combination. We have successfully applied the described methods to simulated data and experimental tank data. Further work must be done to apply these methods to the case of experimental human data, and evaluate their usefulness in clinical settings. The work regarding the *a priori* D-bar methods has resulted in a preliminary version of a manuscript published on ArXiv.org [7]. This work is currently being refined and we hope to have the result published in a peer-reviewed journal in the near future. This work has also spawned a collaborative work with S. Hamilton [79], wherein the *a priori* methods are applied to 2-D EIT imaging for complex admittivities on simulated chest-shaped domains.

BIBLIOGRAPHY

[1] Health risks from exposure to low levels of ionizing radiation. *BEIR VII phase*, 2, 2006.

[2] J.F.P.J. Abascal, S.R. Arridge, D. Atkinson, R. Horesh, L. Fabrizi, M. De Lucia, L. Horesh, R.H. Bayford, and D.S. Holder. Use of anisotropic modelling in electrical impedance tomography; description of method and preliminary assessment of utility in imaging brain function in the adult human head. *Neuroimage*, 43(2):258–268, 2008.

[3] A. Adler, B. Grychtol, and R. Bayford. Why is EIT so hard, and what are we doing about it? *Physiological measurement*, 36(6):1067, 2015.

[4] G. Alessandrini. Stable determination of conductivity by boundary measurements. *Applicable Analysis*, 27(1–3):153–172, 1988.

[5] G. Alessandrini. Singular solutions of elliptic equations and the determination of conductivity by boundary measurements. *Journal of Differential Equations*, 84(2):252–272, 1990.

[6] A. Allers and F. Santosa. Stability and resolution analysis of a linearized problem in electrical impedance tomography. *Inverse Problems*, 7(4):515–533, 1991.

[7] M. Alsaker and J.L. Mueller. A D-bar algorithm with a priori information for 2-D electrical impedance tomography. *arXiv:1505.01196*, 2015.

[8] M. Dodd (Alsaker) and J.L. Mueller. Fast D-bar reconstructions of ventilation and perfusion on a pairwise current injection system. In A. Adler and B. Grychtol, editors, *Proceedings of the 15th International Conference on Biomedical Applications of Electrical Impedance Tomography*, page 81, 2014.

[9] M. Dodd (Alsaker) and J.L. Mueller. A real-time D-bar algorithm for 2-D electrical impedance tomography data. *Inverse Problems and Imaging*, 8(4):1013–1031, 2014.

[10] G.M. Amdahl. Validity of the single processor approach to achieving large scale computing capabilities. In *Proceedings of the April 18-20, 1967, Spring Joint Computer Conference*, pages 483–485. ACM, 1967.

[11] D. Andreuccetti, R. Fossi, and C. Petrucci. Calculation of the dielectric properties of body tissues in the frequency range 10 Hz - 100 GHz. http://niremf.ifac.cnr.it/tissprop/htmlclie/htmlclie.php. Accessed: 2016-02-11.

[12] K. Astala, J.L. Mueller, L. Päivärinta, A. Perämäki, and S. Siltanen. Direct electrical impedance tomography for nonsmooth conductivities. *Inverse Problems and Imaging*, 5(3):531–549, 2011.

[13] K. Astala and L. Päivärinta. Calderón's inverse conductivity problem in the plane. *Annals of Mathematics*, 163(1):265–299, 2006.

[14] N.J. Avis and D.C. Barber. Incorporating a priori information into the Sheffield filtered backprojection algorithm. *Physiological Measurement*, 16(3A):A111–A122, 1995.

[15] A.P. Bagshaw, A.D. Liston, R.H. Bayford, A. Tizzard, A.P. Gibson, A.T. Tidswell, M.K. Sparkes, H. Dehghani, C.D. Binnie, and D.S. Holder. Electrical impedance tomography of human brain function using reconstruction algorithms based on the finite element method. *NeuroImage*, 20(2):752–764, 2003.

[16] D.C. Barber and B.H. Brown. Applied potential tomography. *Journal of physics. E. Scientific instruments*, 17(9):723–733, 1984.

[17] D.C. Barber and B.H. Brown. Progress in electrical impedance tomography. *Inverse problems in partial differential equations*, pages 151–64, 1990.

[18] R. Barrett, M. Berry, T. F. Chan, J. Demmel, J. Donato, J. Dongarra, V. Eijkhout, R. Pozo, C. Romine, and H. Van der Vorst. *Templates for the Solution of Linear*

Systems: Building Blocks for Iterative Methods, 2nd Edition. SIAM, Philadelphia, PA, 1994.

[19] U. Baysal and B.M. Eyüboglu. Use of a priori information in estimating tissue resistivities - a simulation study. *Physics in Medicine and Biology*, 43(12):3589–3606, 1998.

[20] R. Beals and R. Coifman. Scattering, transformations spectrales et équations d'évolution non linéaire ii. *Séminaire Équations aux dérivées partielles (Polytechnique)*, pages 1–8, 1982.

[21] R. Beals and R.R. Coifman. Multidimensional inverse scattering and nonlinear partial differential equations. In *Proc. Symp. Pure Math*, volume 43, pages 45–70, 1985.

[22] C.A. Berenstein and E.C. Tarabusi. Inversion formulas for the k-dimensional radon transform in real hyperbolic spaces. *Duke Mathematical Journal*, 62(3):613–631, 1991.

[23] J. Bikowski and J.L. Mueller. 2D EIT reconstructions using Calderóns method. *Inverse Problems and Imaging*, 2(1):43–61, 2008.

[24] A. Binley, S. Henry-Poulter, and B. Shaw. Examination of solute transport in an undisturbed soil column using electrical resistance tomography. *Water Resources Research*, 32(4):763–769, 1996.

[25] R.S. Blue, D. Isaacson, and J.C. Newell. Real-time three-dimensional electrical impedance imaging. *Physiological Measurement*, 21(1):15–26, 2000.

[26] G.T. Bolton and K.M. Primrose. An overview of electrical tomographic measurements in pharmaceutical and related application areas. *AAPS PharmSciTech*, 6(2):E137–E143.

[27] L. Borcea. A nonlinear multigrid for imaging electrical conductivity and permittivity at low frequency. *Inverse Problems*, 17(2):329–359, 2001.

[28] L. Borcea, J.G. Berryman, and G.C. Papanicolaou. High-contrast impedance tomography. *Inverse Problems*, 12(6):835–858, 1996.

[29] A. Borsic, R. Halter, Y. Wan, A. Hartov, and K.D. Paulsen. Sensitivity study and optimization of a 3d electric impedance tomography prostate probe. *Physiological measurement*, 30(6):S1, 2009.

[30] A. Borsic, R. Halter, Y. Wan, A. Hartov, and K.D. Paulsen. Electrical impedance tomography reconstruction for three-dimensional imaging of the prostate. *Physiological measurement*, 31(8):S1, 2010.

[31] G. Boverman, T.J. Kao, D. Isaacson, and G. Saulnier. An implementation of Calderón's method for 3-D limited-view EIT. *Medical Imaging, IEEE Transactions on*, 28(7):1073–1082, 2009.

[32] G. Boverman, T.J. Kao, R. Kulkarni, B.S. Kim, D. Isaacson, G. Saulnier, and J.C. Newell. Robust linearized image reconstruction for multifrequency EIT of the breast. *Medical Imaging, IEEE Transactions on*, 27(10):1439–1448, 2008.

[33] B.H. Brown. Electrical impedance tomography (EIT): a review. *Journal of Medical Engineering & Technology*, 27(3):97–108, 2003.

[34] B.H. Brown, D.C. Barber, A.H. Morice, and A.D. Leathard. Cardiac and respiratory related electrical impedance changes in the human thorax. *Biomedical Engineering, IEEE Transactions on*, 41(8):729–734, 1994.

[35] R. Brown and G. Uhlmann. Uniqueness in the inverse conductivity problem for non-smooth conductivities in two dimensions. *Communications in Partial Differential Equations*, 22(5–6):1009–1027, 1997.

[36] A.L. Bukhgeim. Recovering a potential from Cauchy data in the two-dimensional case. *Journal of Inverse and Ill-posed Problems*, 16(1):19–33, 2008.

[37] A.P. Calderòn. On an inverse boundary value problem. In *Seminar on Numerical Analysis and Its Applications to Continuum Physics*, pages 65–73. Sociedade Brasileira de Matematica (Rio de Janeiro), 1980.

[38] E.D.L.B. Camargo. *Development of an absolute electrical impedance imaging algorithm for clinical use*. PhD thesis, University of São Paulo, Brazil, 2013.

[39] M. Cheney and D. Isaacson. Distinguishability in impedance imaging. *Biomedical Engineering, IEEE Transactions on*, 39(8):852–860, 1992.

[40] M. Cheney, D. Isaacson, and E.L. Isaacson. Exact solutions to a linearized inverse boundary value problem. *Inverse Problems*, 6(6):923–934, 1990.

[41] M. Cheney, D. Isaacson, J. C. Newell, S. Simske, and J. Goble. Noser: An algorithm for solving the inverse conductivity problem. *International Journal of Imaging Systems and Technology*, 2(2):66–75, 1990.

[42] M. Cheney, D. Isaacson, and J.C. Newell. Electrical impedance tomography. *SIAM Review*, 41(1):85–101, 1999.

[43] V. Cherepenin, A. Karpov, A. Korjenevsky, V. Kornienko, A. Mazaletskaya, D. Mazourov, and D. Meister. A 3D electrical impedance tomography (EIT) system for breast cancer detection. *Physiological measurement*, 22(1):9, 2001.

[44] M.H. Choi, T.J. Kao, D. Isaacson, G. Saulnier, and J.C. Newell. A reconstruction algorithm for breast cancer imaging with electrical impedance tomography in mammography geometry. *IEEE Transactions on Biomedical Engineering*, 54(4):700–710, 2007.

[45] E.L.V. Costa, R. Gonzalez Lima, and M.B.P. Amato. Electrical impedance tomography. In J.L. Vincent, editor, *Intensive Care Medicine*, pages 394–404. Springer, New York, 2009.

[46] W. Daily and A. Ramirez. Electrical resistance tomography during in-situ trichloroethylene remediation at the Savannah River site. *Journal of Applied Geophysics*, 33(4):239–249, 1995.

[47] W. Daily, A. Ramirez, D. LaBrecque, and W. Barber. Electrical resistance tomography experiments at the oregon graduate institute. *Journal of Applied Geophysics*, 33(4):227–237, 1995.

[48] W. Daily, A. Ramirez, D. LaBrecque, and J. Nitao. Electrical resistivity tomography of vadose water movement. *Water Resources Research*, 28(5):1429–1442, 1992.

[49] W. Daily and A.L. Ramirez. Electrical imaging of engineered hydraulic barriers. *Geophysics*, 65(1):83–94, 2000.

[50] M. DeAngelo and J.L. Mueller. 2D D-bar reconstructions of human chest and tank data using an improved approximation to the scattering transform. *Physiological measurement*, 31(2):221–232, 2010.

[51] H. Dehghani, D.C. Barber, and I. Basarab-Horwath. Incorporating a priori anatomical information into image reconstruction in electrical impedance tomography. *Physiological Measurement*, 20(1):87–102, 1999.

[52] R. Deiana, G. Cassiani, A. Villa, A. Bagliani, and V. Bruno. Calibration of a vadose zone model using water injection monitored by GPR and electrical resistance tomography. *Vadose Zone Journal*, 7(1):215–226, 2008.

[53] F.J. Dickin, R.A. Williams, and M.S. Beck. Determination of composition and motion of multicomponent mixtures in process vessels using electrical impedance tomography-i. principles and process engineering applications. *Chemical Engineering Science*, 48(10):1883 – 1897, 1993.

[54] D.C. Dobson. Convergence of a reconstruction method for the inverse conductivity problem. *SIAM Journal on Applied Mathematics*, 52(2):442–458, 1992.

[55] D.C. Dobson and F. Santosa. An image-enhancement technique for electrical impedance tomography. *Inverse Problems*, 10(2):317–334, 1994.

[56] O. Dorn, H. Bertete-Aguirre, J.G. Berryman, and G.C. Papanicolaou. A nonlinear inversion method for 3D electromagnetic imaging using adjoint fields. *Inverse Problems*, 15(6):1523–1558, 1999.

[57] T. Dowrick, G.S. Dos Santos, A. Vongerichten, and D. Holder. Parallel, multi frequency EIT measurement, suitable for recording impedance changes during epilepsy. *Journal of Electrical Bioimpedance*, 6(1):37–43, 2015.

[58] A. El-Zaart and T. El-Arwadi. A new edge detection method for CT-scan lung images. *Journal of Biomedical Engineering and Medical Imaging*, 2(5), 2015.

[59] L.D. Faddeev. Increasing solutions of the Schrödinger equation. *Soviet Physics Doklady*, 10:1033–1035, 1966.

[60] R. Fazel, H.M. Krumholz, Y. Wang, J.S. Ross, H. H. Chen, J.and Ting, N.D. Shah, K. Nasir, A.J. Einstein, and B.K. Nallamothu. Exposure to low-dose ionizing radiation from medical imaging procedures. *New England Journal of Medicine*, 361(9):849–857, 2009.

[61] D. Ferrario, B. Grychtol, A. Adler, J. Sola, S.H. Bohm, and M. Bodenstein. Toward morphological thoracic EIT: Major signal sources correspond to respective organ locations in CT. *Biomedical Engineering, IEEE Transactions on*, 59(11):3000–3008, 2012.

[62] D. Flores-Tapia and S. Pistorius. Electrical impedance tomography reconstruction using a monotonicity approach based on a priori knowledge. In *Engineering in Medicine*

and Biology Society (EMBC), 2010 Annual International Conference of the IEEE, pages 4996–4999, Aug 2010.

[63] E. Francini. Recovering a complex coefficient in a planar domain from the Dirichlet-to-Neumann map. *Inverse Problems*, 16(1):107–119, 2000.

[64] D. Freimark, M. Arad, R. Sokolover, S. Zlochiver, and S. Abboud. Monitoring lung fluid content in CHF patients under intravenous diuretics treatment using bio-impedance measurements. *Physiological measurement*, 28(7):S269–S277, 2007.

[65] I. Frerichs. Electrical impedance tomography (EIT) in applications related to lung and ventilation: a review of experimental and clinical activities. *Physiological Measurement*, 21(2):R1–R21, 2000.

[66] I. Frerichs, J. Hinz, P. Herrmann, G. Weisser, G. Hahn, T. Dudykevych, M. Quintel, and G. Hellige. Detection of local lung air content by electrical impedance tomography compared with electron beam CT. *Journal of applied physiology*, 93(2):660–666, 2002.

[67] I. Frerichs, J. Hinz, P. Herrmann, G. Weisser, G. Hahn, M. Quintel, and G. Hellige. Regional lung perfusion as determined by electrical impedance tomography in comparison with electron beam CT imaging. *Medical Imaging, IEEE Transactions on*, 21(6):646–652, 2002.

[68] I. Frerichs, S. Pulletz, G. Elke, F. Reifferscheid, D. Schädler, J. Scholz, and N. Weiler. Assessment of changes in distribution of lung perfusion by electrical impedance tomography. *Respiration*, 77(3):282–291, 2009.

[69] I. Frerichs, G. Schmitz, S. Pulletz, D. Schädler, G. Zick, J. Scholz, and N. Weiler. Reproducibility of regional lung ventilation distribution determined by electrical impedance tomography during mechanical ventilation. *Physiological Measurement*, 28(7):S261–S267, 2007.

[70] R.W. Freund. A transpose-free quasi-minimal residual algorithm for non-Hermitian linear systems. *SIAM journal on scientific computing*, 14(2):470–482, 1993.

[71] L.F. Fuks, M. Cheney, D. Isaacson, D.G. Gisser, and J.C. Newell. Detection and imaging of electric conductivity and permittivity at low frequency. *Biomedical Engineering, IEEE Transactions on*, 38(11):1106–1110, 1991.

[72] C.S. Gardner, J.M. Greene, M.D. Kruskal, and R.M. Miura. Method for solving the Korteweg-deVries equation. *Physical Review Letters*, 19:1095–1097, 1967.

[73] O. Gilad and D.S. Holder. Impedance changes recorded with scalp electrodes during visual evoked responses: implications for electrical impedance tomography of fast neural activity. *Neuroimage*, 47(2):514–522, 2009.

[74] M. Hallaji, A. Seppnen, and M. Pour-Ghaz. Electrical impedance tomography-based sensing skin for quantitative imaging of damage in concrete. *Smart Materials and Structures*, 23(8):085001, 2014.

[75] R.J. Halter, A. Hartov, and K.D. Paulsen. A broadband high-frequency electrical impedance tomography system for breast imaging. *Biomedical Engineering, IEEE Transactions on*, 55(2):650–659, 2008.

[76] S.J. Hamilton, C. N. L. Herrera, J. L. Mueller, and A. Von Herrmann. A direct D-bar reconstruction algorithm for recovering a complex conductivity in 2D. *Inverse Problems*, 28(9):095005, 2012.

[77] S.J. Hamilton, M. Lassas, and S. Siltanen. A direct reconstruction method for anisotropic electrical impedance tomography. *Inverse Problems*, 30(7):075007, 2014.

[78] S.J. Hamilton and J. L. Mueller. Direct EIT reconstructions of complex admittivities on a chest-shaped domain in 2-D. *IEEE transactions on medical imaging*, 32(4):757–769, 2013.

[79] S.J. Hamilton, J. L. Mueller, and M. Alsaker. Incorporating a spatial prior into nonlinear D-bar EIT imaging for complex admittivities. *In review*, 2016.

[80] S.J. Hamilton and S. Siltanen. A data-driven edge-preserving D-bar method for electrical impedance tomography. *Inverse Problems and Imaging*, 8(4):1053–1072, 2014.

[81] L.M. Heikkinen, J. Kourunen, T. Savolainen, P.J. Vauhkonen, J.P. Kaipio, and M. Vauhkonen. Real time three-dimensional electrical impedance tomography applied in multiphase flow imaging. *Measurement Science and Technology*, 17(8):2083, 2006.

[82] L.M. Heikkinen, M. Vauhkonen, T. Savolainen, K. Leinonen, and J.P. Kaipio. Electrical process tomography with known internal structures and resistivities. *Inverse Problems in Engineering*, 9(5):431–454, 2001.

[83] T. Hermans, D. Caterina, R. Martin, A. Kemna, T. Robert, and F. Nguyen. How to incorporate prior information in geophysical inverse problems-deterministic and geostatistical approaches. In *Near Surface 2011-17th EAGE European Meeting of Environmental and Engineering Geophysics*, 2011.

[84] C.N.L. Herrera, M.F.M. Vallejo, J.L. Mueller, and R.G. Lima. Direct 2-D reconstructions of conductivity and permittivity from EIT data on a human chest. *IEEE Transactions on Medical Imaging*, 34(1):267–274, 2015.

[85] J. Hoła and K. Schabowicz. State-of-the-art non-destructive methods for diagnostic testing of building structures anticipated development trends. *Archives of Civil and Mechanical Engineering*, 10(3):5–18, 2010.

[86] D. Holder, editor. *Electrical Impedance Tomography: Methods, History and Applications*. IOP Publishing Ltd., Bristol, UK, 2005.

[87] T.C. Hou and J.P. Lynch. Electrical impedance tomographic methods for sensing strain fields and crack damage in cementitious structures. *Journal of Intelligent Material Systems and Structures*, 20(11):1363–1379, 2009.

[88] S. Hu, E.A. Hoffman, and J.M. Reinhardt. Automatic lung segmentation for accurate quantitation of volumetric X-ray CT images. *Medical Imaging, IEEE Transactions on*, 20(6):490–498, 2001.

[89] P. Hua, E.J. Woo, J.G. Webster, and W.J. Tompkins. Bladder fullness detection using multiple electrodes. In *Proceedings of the Annual International Conference of the IEEE Engineering in Medicine and Biology Society*, 1988.

[90] U.Z. Ijaz, B.S. Kim, T.J. Kao, A.K. Khambampati, S. Kim, M.C. Kim, J.C. Newell, D. Isaacson, and K.Y. Kim. Mammography phantom studies using 3D electrical impedance tomography with numerical forward solver. In *Frontiers in the Convergence of Bioscience and Information Technologies*, pages 379–383, 2007.

[91] D. Isaacson and M. Cheney. Current problems in impedance imaging. *Inverse problems in partial differential equations*, pages 141–149, 1990.

[92] D. Isaacson and M. Cheney. Effects of measurement precision and finite numbers of electrodes on linear impedance imaging algorithms. *SIAM Journal on Applied Mathematics*, 51(6):1705–1731, 1991.

[93] D. Isaacson and E.L. Isaacson. Comment on A.P. Calderóns paper:on an inverse boundary value problem. *mathematics of computation*, 52(186):553–559, 1989.

[94] D. Isaacson, J.L. Mueller, J.C. Newell, and S. Siltanen. Reconstructions of chest phantoms by the D-bar method for electrical impedance tomography. *Medical Imaging, IEEE Transactions on*, 23(7):821–828, 2004.

[95] D. Isaacson, J.L. Mueller, J.C. Newell, and S. Siltanen. Imaging cardiac activity by the D-bar method for electrical impedance tomography. *Physiological Measurement*, 27(5):S43–S50, 2006.

[96] H. Jin, S. Yang, M. Wang, and R.A. Williams. Measurement of gas holdup profiles in a gas liquid cocurrent bubble column using electrical resistance tomography. *Flow Measurement and Instrumentation*, 18(56):191 – 196, 2007.

[97] J. Jossinet, E.l Marry, and A. Montalibet. Electrical impedance endo-tomography: imaging tissue from inside. *Medical Imaging, IEEE Transactions on*, 21(6):560–565, 2002.

[98] J.P. Kaipio, V. Kolehmainen, E. Somersalo, and M. Vauhkonen. Statistical inversion and Monte Carlo sampling methods in electrical impedance tomography. *Inverse Problems*, 16(5):1487–1522, 2000.

[99] J.P. Kaipio, V. Kolehmainen, M. Vauhkonen, and E. Somersalo. Inverse problems with structural prior information. *Inverse problems*, 15(3):713, 1999.

[100] J.S. Kallman and J.G. Berryman. Weighted least-squares criteria for electrical impedance tomography. *Medical Imaging, IEEE Transactions on*, 11(2):284–292, 1992.

[101] T.J. Kao, G.J. Saulnie, H Xia, C. Tamma, J.C. Newell, and D. Isaacson. A compensated radiolucent electrode array for combined EIT and mammography. *Physiological Measurement*, 28(7):S291S299, 2007.

[102] K. Karhunen, A. Seppänen, A. Lehikoinen, P. J.M. Monteiro, and J.P. Kaipio. Electrical resistance tomography imaging of concrete. *Cement and Concrete Research*, 40(1):137–145, 2010.

[103] P.G. Kaup and F. Santosa. Nondestructive evaluation of corrosion damage using electrostatic measurements. *Journal of Nondestructive Evaluation*, 14(3):127–136, 1995.

[104] T.E. Kerner, K.D. Paulsen, A. Hartov, S.K. Soho, and S.P. Poplack. Electrical impedance spectroscopy of the breast: clinical imaging results in 26 subjects. *IEEE Transactions on Medical Imaging*, 21(6):638–645, 2002.

[105] S. Kim, A.N. Nkaya, and T. Dyakowski. Measurement of mixing of two miscible liquids in a stirred vessel with electrical resistance tomography. *International Communications in Heat and Mass Transfer*, 33(9):1088–1095, 2006.

[106] K. Knudsen. A new direct method for reconstructing isotropic conductivities in the plane. *Physiological Measurement*, 24(2):391, 2003.

[107] K. Knudsen, M. Lassas, J.L. Mueller, and S. Siltanen. D-bar method for electrical impedance tomography with discontinuous conductivities. *SIAM Journal on Applied Mathematics*, 67(3):893–913, 2007.

[108] K. Knudsen, M. Lassas, J.L. Mueller, and S. Siltanen. Regularized D-bar method for the inverse conductivity problem. *Inverse Problems and Imaging*, 35(4):599–624, 2009.

[109] K. Knudsen, J. Mueller, and S. Siltanen. Numerical solution method for the dbar-equation in the plane. *Journal of Computational Physics*, 198(2):500–517, 2004.

[110] K. Knudsen and A. Tamasan. Reconstruction of less regular conductivities in the plane. *Communications in Partial Differential Equations*, 29(3–4):361–381, 2005.

[111] K. Koch, J. Wenninger, S. Uhlenbrook, and M. Bonell. Joint interpretation of hydrological and geophysical data: electrical resistivity tomography results from a process hydrological research site in the Black Forest Mountains, Germany. *Hydrological Processes*, 23(10):1501–1513, 2009.

[112] R.V. Kohn and A. McKenney. Numerical implementation of a variational method for electrical impedance tomography. *Inverse Problems*, 6(3):389–414, 1990.

[113] R.V. Kohn and M. Vogelius. Determining conductivity by boundary measurements. *Communications on Pure and Applied Mathematics*, 37(3):289–298, 1984.

[114] R.V. Kohn and M. Vogelius. Determining conductivity by boundary measurements ii. interior results. *Communications on Pure and Applied Mathematics*, 38(5):643–667, 1985.

[115] R.V. Kohn and M. Vogelius. Relaxation of a variational method for impedance computed tomography. *Communications on Pure and Applied Mathematics*, 40(6):745–777, 1987.

[116] V. Kolehmainen, E. Somersalo, P.J. Vauhkonen, M. Vauhkonen, and J.P. Kaipio. A Bayesian approach and total variation priors in 3D electrical impedance tomography. In *Engineering in Medicine and Biology Society, 1998. Proceedings of the 20th Annual International Conference of the IEEE*, volume 2, pages 1028–1031 vol.2, 1998.

[117] J. Kourunen, R. Kyhk, J. Matula, J. Kyhk, M. Vauhkonen, and L.M. Heikkinen. Imaging of mixing of two miscible liquids using electrical impedance tomography and linear impedance sensor. *Flow Measurement and Instrumentation*, 19(6):391 – 396, 2008.

[118] P.W.A. Kunst, A. Vonk Noordegraaf, O.S. Hoekstra, P.E. Postmus, and P.M.J.M. De Vries. Ventilation and perfusion imaging by electrical impedance tomography: a comparison with radionuclide scanning. *Physiological measurement*, 19(4):481–490, 1998.

[119] P.W.A. Kunst, A. Vonk Noordegraaf, E. Raaijmakers, J. Bakker, A.B.J. Groeneveld, P.E. Postmus, and P.M.J.M. de Vries. Electrical impedance tomography in the assessment of extravascular lung water in noncardiogenic acute respiratory failure. *CHEST*, 116(6):1695–1702, 1999.

[120] H. Kwon, J.I. Choi, and J.K. Seo. An electrical impedance monitoring method of water-lubricated oil transportation. *Flow Measurement and Instrumentation*, 46, Part B:327–333, 2015.

[121] A.D. Leathard, B.H. Brown, J. Campbell, F. Zhang, A.H. Morice, and D. Tayler. A comparison of ventilatory and cardiac related changes in EIT images of normal human lungs and of lungs with pulmonary emboli. *Physiological Measurement*, 15(2A):A137–A146, 1994.

[122] S. Leonhardt, A. Cordes, H. Plewa, R. Pikkemaat, I. Soljanik, K. Moehring, H.J. Gerner, and R. Rupp. Electric impedance tomography for monitoring volume and size of the urinary bladder. *Biomedizinische Technik/Biomedical Engineering*, 56(6):301–307, 2011.

[123] R. Li, J. Gao, Y. Li, J. Wu, Z. Zhao, and Y. Liu. Preliminary study of assessing bladder urinary volume using electrical impedance tomography. *Journal of Medical and Biological Engineering*, pages 1–9, 2016.

[124] S.C. Li, L.C. Nie, B. Liu, J. Song, Z.Y. Liu, M.X. Su, and L. Xu. 3d electrical resistivity inversion using prior spatial shape constraints. *Applied Geophysics*, 10(4):361–372, 2013.

[125] A. Lipponen, A.Seppänen, and J.P. Kaipio. Reduced-order estimation of nonstationary flows with electrical impedance tomography. *Inverse Problems*, 26(7):074010, 2010.

[126] R. Mann, M. Wang, A.E. Forrest, P.J. Holden, T. Dyakowski, F.J. Dickin, and R.B. Edwards. Gas-liquid and miscible liquid mixing in a plant-scale vessel monitored using electrical resistance tomography. *Chemical Engineering Communications*, 175(1):39–48, 1999.

[127] M.M. Mellenthin. *The Active Complex Electrode (ACE1) Electrical Impedance Tomography System & Anatomically Inspired Modeling of Electrode-Skin Contact Impedance*. PhD thesis, Colorado State University, 2016.

[128] M.M. Mellenthin, J.L. Mueller, E.D.L. Bueno de Camargo, F. Silva de Moura, S.J. Hamilton, and R. Gonzalez Lima. The ACE1 thoracic electrical impedance tomography system for ventilation and perfusion. In *Engineering in Medicine and Biology Society (EMBC), 2015 37th Annual International Conference of the IEEE*, pages 4073–4076. IEEE, 2015.

[129] J. L. Mueller and S. Siltanen. *Linear and Nonlinear Inverse Problems with Practical Applications*. Society for Industrial and Applied Mathematics, Philadelphia, PA, 2012.

[130] J.L. Mueller, D. Isaacson, and J.C. Newell. A reconstruction algorithm for electrical impedance tomography data collected on rectangular electrode arrays. *IEEE Transactions on Biomedical Engineering*, 46(11):1379–1386, 1999.

[131] J.L. Mueller, D. Isaacson, and J.C. Newell. Reconstruction of conductivity changes due to ventilation and perfusion from EIT data collected on a rectangular electrode array. *Physiological Measurement*, 22(1):97–106, 2001.

[132] J.L. Mueller and S. Siltanen. Direct reconstructions of conductivities from boundary measurements. *SIAM Journal on Scientific Computing*, 24(4):1232–1266, 2003.

[133] J.L. Mueller, S. Siltanen, and D. Isaacson. A direct reconstruction algorithm for electrical impedance tomography. *IEEE Transactions on Medical Imaging*, 21(6):555–559, 2002.

[134] P.A. Muller, D. Isaacson, J.C. Newell, and G.J. Saulnier. Calderòn's method on an elliptical domain. *Physiological Measurement*, 34(6):609, 2013.

[135] E.K. Murphy and J.L. Mueller. Effect of domain shape modeling and measurement errors on the 2-D D-bar method for EIT. *IEEE Transactions on Medical Imaging*, 28(10):1576–1584, 2009.

[136] A. Nachman, J. Sylvester, and G. Uhlmann. An n-dimensional Borg-Levinson theorem. *Communications in Mathematical Physics*, 115(4):595–605, 1988.

[137] A.I. Nachman. Reconstructions from boundary measurements. *Annals of Mathematics*, 128(3):531–576, 1988.

[138] A.I. Nachman. Global uniqueness for a two-dimensional inverse boundary value problem. *Annals of Mathematics*, 143(1):71–96, 1996.

[139] J.C. Newell, P.M. Edic, Xiaodan Ren, J.L. Larson-Wiseman, and M.D. Danyleiko. Assessment of acute pulmonary edema in dogs by electrical impedance imaging. *IEEE Transactions on Biomedical Engineering*, 43(2):133–138, 1996.

[140] D.T. Nguyen, C. Jin, A. Thiagalingam, and A.L. McEwan. A review on electrical impedance tomography for pulmonary perfusion imaging. *Physiological measurement*, 33(5):695, 2012.

[141] A. Nissinen, J.P. Kaipio, M. Vauhkonen, and V. Kolehmainen. Contrast enhancement in EIT imaging of the brain. *Physiological measurement*, 37(1):1, 2015.

[142] T.J. Noble, A.H. Morice, K.S. Channer, P. Milnes, N D. Harris, and B.H. Brown. Monitoring patients with left ventricular failure by electrical impedance tomography. *European Journal of Heart Failure*, 1(4):379–384, 1999.

[143] M. Noel and B. Xu. Archaeological investigation by electrical resistivity tomography: a preliminary study. *Geophysical Journal International*, 107(1):95–102, 1991.

[144] R.G. Novikov. Multidimensional inverse spectral problem for the equation $-\Delta\psi + (v(x) - Eu(x))\psi = 0$. *Functional Analysis and Its Applications*, 22(4):263–272, 1988.

[145] C. Oberdörster, J. Vanderborght, A. Kemna, and H. Vereecken. Investigating preferential flow processes in a forest soil using time domain reflectometry and electrical resistivity tomography. *Vadose Zone Journal*, 9(2):350–361, 2010.

[146] W.R.B. Polydorides, N.and Lionheart and H. McCann. Krylov subspace iterative techniques: on the detection of brain activity with electrical impedance tomography. *Medical Imaging, IEEE Transactions on*, 21(6):596–603, 2002.

[147] A. Ramirez, W. Daily, A. Binley, D. LaBrecque, and D. Roelant. Detection of leaks in underground storage tanks using electrical resistance methods. *Journal of Environmental and Engineering Geophysics*.

[148] A. Ramirez, W. Daily, D. LaBrecque, E. Owen, and D. Chesnut. Monitoring an underground steam injection process using electrical resistance tomography. *Water Resources Research*, 29(1):73–87, 1993.

[149] A.L. Ramirez, J.J. Nitao, W.G. Hanley, R. Aines, R.E. Glaser, S.K. Sengupta, K.M. Dyer, T.L. Hickling, and W.D. Daily. Stochastic inversion of electrical resistivity changes using a Markov chain Monte Carlo approach. *Journal of Geophysical Research: Solid Earth*, 110(B2), 2005.

[150] M.G. Rasteiro, R.C.C. Silva, F.A.P. Garcia, and P.M. Faia. Electrical tomography: a review of configurations and applications to particulate processes. *KONA Powder and Particle Journal*, 29:67–80, 2011.

[151] V. Rimpiläinen, L.M. Heikkinen, M. Kuosmanen, A. Lehikoinen, A.and Voutilainen, and J. Vauhkonen, M.and Ketolainen. An electrical impedance tomography-based approach to monitor in vitro sodium chloride dissolution from pharmaceutical tablets. *Review of Scientific Instruments*, 80(10), 2009.

[152] V. Rimpiläinen, M. Kuosmanen, J. Ketolainen, K. Jrvinen, M. Vauhkonen, and L.M. Heikkinen. Electrical impedance tomography for three-dimensional drug release monitoring. *European Journal of Pharmaceutical Sciences*, 41(2):407 – 413, 2010.

[153] A. Romsauerova, A. McEwan, L. Horesh, R. Yerworth, R.H. Bayford, and D.S. Holder. Multi-frequency electrical impedance tomography (EIT) of the adult human head: initial findings in brain tumours, arteriovenous malformations and chronic stroke, development of an analysis method and calibration. *Physiological Measurement*, 27(5):S147–S161, 2006.

[154] Y. Saad and M.H. Schultz. GMRES: A generalized minimal residual algorithm for solving nonsymmetric linear systems. *SIAM Journal on Scientific and Statistical Computing*, 7(3):856–869, 1986.

[155] F. Santosa and M. Vogelius. A backprojection algorithm for electrical impedance imaging. *SIAM Journal on Applied Mathematics*, 50(1):216–243, 1990.

[156] T. Schlebusch, S. Nienke, S. Leonhardt, and M. Walter. Bladder volume estimation from electrical impedance tomography. *Physiological measurement*, 35(9):1813, 2014.

[157] A. Seppänen, K. Karhunen, A. Lehikoinen, J.P. Kaipio, and P.J.M. Monteiro. Electrical resistance tomography imaging of concrete. In *Concrete Repair, Rehabilitation and Retrofitting II: 2nd International Conference on Concrete Repair, Rehabilitation and Retrofitting*, pages 571–577, 2009.

[158] A. Seppänen, V. Nissinen, A.and Kolehmainen, S. Siltanen, and A.M. Laukkanen. Electrical impedance tomography imaging of larynx. In *MAVEBA*, pages 27–29, 2011.

[159] A.V. Shahidi, R. Guardo, and P. Savard. On the monitoring of pulmonary edema by impedance tomography. In *Engineering in Medicine and Biology Society, 1994.*

Engineering Advances: New Opportunities for Biomedical Engineers. Proceedings of the 16th Annual International Conference of the IEEE, 1994.

[160] P.C. Shetiye, A.A. Ghatol, V.N. Ghate, and S.R. Patil. Detection of breast cancer using electrical impedance and RBF neural network. *International Journal of Information and Electronics Engineering*, 5(5):356, 2015.

[161] V. Shevnin, O. Delgado-Rodriguez, A. Mousatov, E. Nakamura-Labastida, and A. Mejia-Aguilar. Oil pollution detection using resistivity sounding. *Geofisica Internacional*, 42(4):613–622, 2003.

[162] S. Siltanen. *Electrical impedance tomography and Faddeev Green's functions*. PhD thesis, Helsinki University of Technology, November 1999.

[163] S. Siltanen, J. Mueller, and D. Isaacson. An implementation of the reconstruction algorithm of A Nachman for the 2D inverse conductivity problem. *Inverse Problems*, 16(3):681–699, 2000.

[164] S. Siltanen and J.P. Tamminen. Reconstructing conductivities with boundary corrected D-bar method. *Journal of Inverse and Ill-Posed Problems*, 22(6):847–870, 2014.

[165] G.L.G. Sleijpen and D.R. Fokkema. BiCGstab(l) for linear equations involving unsymmetric matrices with complex spectrum. *Electronic Transactions on Numerical Analysis*, 1(11):2000, 1993.

[166] H.J. Smit, A. Vonk Noordegraaf, J. T. Marcus, A. Boonstra, P.M de Vries, and P.E. Postmus. Determinants of pulmonary perfusion measured by electrical impedance tomography. *European journal of applied physiology*, 92(1-2):45–49, 2004.

[167] M. Soleimani. Electrical impedance tomography imaging using a priori ultrasound data. *BioMedical Engineering OnLine*, 5(8), 2006.

[168] E. Somersalo, M. Cheney, D. Isaacson, and E. Isaacson. Layer stripping: a direct numerical method for impedance imaging. *Inverse Problems*, 7(6):899–926, 1991.

[169] E. Somersalo, J.P. Kaipio, M.J. Vauhkonen, D. Baroudi, and S. Jaervenpaeae. Impedance imaging and Markov chain Monte Carlo methods, 1997.

[170] P. Sonneveld. CGS, a fast Lanczos-type solver for nonsymmetric linear systems. *SIAM journal on scientific and statistical computing*, 10(1):36–52, 1989.

[171] T. Strauss and T. Khan. Statistical inversion in electrical impedance tomography using mixed total variation and non-convex lp regularization prior. *Journal of Inverse and Ill-posed Problems*, 23(5):529–542, 2015.

[172] H. Syed, A. Borsic, A. Hartov, and R.J. Halter. Anatomically accurate hard priors for transrectal electrical impedance tomography (treit) of the prostate. *Physiological measurement*, 33(5):719, 2012.

[173] G. Sylvester, J.and Uhlmann. A uniqueness theorem for an inverse boundary value problem in electrical prospection. *Communications on Pure and Applied Mathematics*, 39(1):91–112, 1986.

[174] J. Sylvester. A convergent layer stripping algorithm for the radially symmetric impedence tomography problem. *Communications in Partial Differential Equations*, 17(11–12):1955–1994, 1992.

[175] J. Sylvester and G. Uhlmann. A global uniqueness theorem for an inverse boundary value problem. *Annals of Mathematics*, 125(1):153–169, 1987.

[176] J. Sylvester and G. Uhlmann. Inverse boundary value problems at the boundarycontinuous dependence. *Communications on Pure and Applied Mathematics*, 41(2):197–219, 1988.

[177] J. Sylvester and G. Uhlmann. The dirichlet to neumann map and applications. In *Proceedings of the Conference Inverse problems in partial differential equations (Arcata, 1989), SIAM, Philadelphia*, pages 101–139, 1990.

[178] C.J.C. Trepte, C.R. Phillips, J. Solà, A. Adler, S.A. Haas, M. Rapin, S.H. Böhm, and D.A. Reuter. Electrical impedance tomography (EIT) for quantification of pulmonary edema in acute lung injury. *Critical Care*, 20(1):1–9, 2015.

[179] G. Uhlmann. Inverse problems: seeing the unseen. *Bulletin of Mathematical Sciences*, pages 1–71, 2014.

[180] G. Vainikko. Fast solvers of the Lippmann-Schwinger equation. In R.P. Gilbert, J.i Kajiwara, and Y.S. Xu, editors, *Direct and Inverse Problems of Mathematical Physics*, pages 423–440. Springer US, 2000.

[181] H.A. van der Vorst. Bi-CGSTAB: A fast and smoothly converging variant of Bi-CG for the solution of nonsymmetric linear systems. *SIAM Journal on scientific and Statistical Computing*, 13(2):631–644, 1992.

[182] M. Vauhkonen, D. Vadasz, P.A. Karjalainen, E. Somersalo, and J.P. Kaipio. Tikhonov regularization and prior information in electrical impedance tomography. *Medical Imaging, IEEE Transactions on*, 17(2):285–293, 1998.

[183] J.A. Victorino, J.B. Borges, V.N. Okamoto, G.F.J. Matos, M.R. Tucci, M.P.R. Caramez, H. Tanaka, F.S. Sipmann, D.C.B. Santos, C.S.V. Barbas, C.R.R. Carvalho, and M.B P. Amato. Imbalances in regional lung ventilation: a validation study on electrical impedance tomography. *American Journal of Respiratory and Critical Care Medicine*, 169(7):791–800, 2004.

[184] A. Vonk Noordegraaf, T.J.C. Faes, A. Janse, J.T. Marcus, J.G.F. Bronzwaer, P.E. Postmus, and P.M.J.M. de Vries. Noninvasive assessment of right ventricular diastolic function by electrical impedance tomography. *CHEST*, 111(5):1222–1228, 1997.

[185] A. Vonk Noordegraaf, P.W.A. Kunst, A. Janse, J.T. Marcus, P.E. Postmus, T.J.C. Faes, and P.M.J.M. de Vries. Pulmonary perfusion measured by means of electrical impedance tomography. *Physiological measurement*, 19(2):263, 1998.

[186] Y. Wan, R. Halter, A. Borsic, P. Manwaring, A. Hartov, and K. Paulsen. Sensitivity study of an ultrasound coupled transrectal electrical impedance tomography system for prostate imaging. *Physiological measurement*, 31(8):S17, 2010.

[187] M. Wang, A. Dorward, D. Vlaev, and R. Mann. Measurements of gasliquid mixing in a stirred vessel using electrical resistance tomography (ERT). *Chemical Engineering Journal*, 77(12):93 – 98, 2000.

[188] R.M. West, R.G. Aykroyd, S. Meng, and R.A. Williams. Markov chain Monte Carlo techniques and spatialtemporal modelling for medical EIT. *Physiological Measurement*, 25(1):181–194, 2004.

[189] R.M. West, X. Jia, and R.A. Williams. Quantification of solid-liquid mixing using electrical resistance and positron emission tomography. *Chemical Engineering Communications*, 175(1):71–97, 1999.

[190] R.M. West, D.M. Scott, G. Sunshine, J. Kostuch, L. Heikkinen, M. Vauhkonen, B.S. Hoyle, H.I. Schlaberg, R. Hou, and R.A. Williams. In situ imaging of paste extrusion using electrical impedance tomography. *Measurement Science and Technology*, 13(12):1890, 2002.

[191] A. Wexler, B. Fry, and M. R. Neuman. Impedance-computed tomography algorithm and system. *Appl. Opt.*, 24(23):3985–3992, 1985.

[192] T.J. Yorkey, J.G. Webster, and W.J. Tompkins. Comparing reconstruction algorithms for electrical impedance tomography. *Biomedical Engineering, IEEE Transactions on*, BME-34(11):843–852, 1987.

[193] Q.Y. Zhou, J. Shimada, and A. Sato. Three-dimensional spatial and temporal monitoring of soil water content using electrical resistivity tomography. *Water Resources Research*, 37(2):273–285, 2001.

[194] Y. Zou and Z. Guo. A review of electrical impedance techniques for breast cancer detection. *Medical engineering & physics*, 25(2):79–90, 2003.